Enhanced Energy Harvesting for Rotating Systems using Stochastic Resonance

Hongjip Kim

Dissertation submitted to the faculty of the
Virginia Polytechnic Institute and State University
in partial fulfillment of the requirements for the degree of

Doctor of Philosophy
in
Mechanical Engineering

Lei Zuo, Chair
Robert G. Parker
Tomonari Furukawa
Muhammad R. Hajj

December 17, 2019
Blacksburg, Virginia

Keywords: Energy Harvesting, Rotating Systems, Stochastic Resonance, Self-tuning, FPK equation, Potential asymmetry, Weak periodic potential

Enhanced Energy Harvesting for Rotating Systems applying Stochastic Resonance

Hongjip Kim

ABSTRACT

Energy harvesting from the rotating system has been an influential topic for researchers over the past several years. Yet, most of these harvesters are linear resonance-based harvesters whose output power drops dramatically under random excitations. This poses a serious problem because a lot of vibrations in rotating systems are stochastic. In this dissertation, a novel energy harvesting strategy for rotating systems was proposed by taking advantage of stochastic resonance. Stochastic resonance is referred to as a physical phenomenon that is manifest in nonlinear bistable systems whereby a weak periodic signal can be significantly amplified with the aid of inherent noise or vice versa. Stochastic resonance can thus be used to amplify the noisy and weak vibration motion.

Through mathematical modeling, this dissertation shows that stochastic resonance is particularly favorable to energy harvesting in rotating systems. The conditions for stochastic resonance are satisfied by adding a nonlinear bistable energy harvester to the rotating system because noise and periodic signal already coexist in the rotating environment. Both numerical and experimental results show that stochastic resonance energy harvester has higher power and wider bandwidth than linear harvesters under a rotating environment.

The dissertation also investigates how stochastic resonance changes for the various types of excitation that occur in real-world applications. The co-existence of the vibrational & stochastic resonance is observed depending on the periodic signal to noise ratio.

The dissertation finally proposed two real applications of stochastic resonance energy harvesting. First, stochastic resonance energy harvester for oil drilling applications is presented. In the oil drilling environment, the periodic force in rotating shafts is biased, which can lower the efficacy of stochastic resonance. To solve the problem, an external magnet was placed above the bi-stable energy harvester to compensate for the biased periodic signal. Energy harvester for smart tires is also proposed. The passively tuned system is implemented in a rotating tire via centrifugal force. An inward-oriented rotating beam is used to induce bistability via the centrifugal acceleration of the tire. The results show

that larger power output and wider bandwidth can be obtained by applying the proposed harvesting strategy to the rotating system.

Enhanced Energy Harvesting for Rotating Systems applying Stochastic Resonance

Hongjip Kim

GENERAL AUDIENCE ABSTRACT

In this dissertation, a novel energy harvesting strategy for rotating systems was proposed by taking advantage of stochastic resonance. Stochastic resonance is referred to as a physical phenomenon that is manifest in nonlinear bistable systems whereby a weak periodic signal can be significantly amplified with the aid of inherent noise or vice versa. Stochastic resonance can thus be used to amplify the noisy and weak vibration motion.

Through mathematical modeling, this dissertation shows that stochastic resonance is particularly favorable to energy harvesting in rotating systems. Both numerical and experimental results show that stochastic resonance energy harvester has higher power and wider bandwidth than linear harvesters under a rotating environment.

The dissertation also investigates how stochastic resonance changes for the various types of excitation that occur in real-world applications.

The dissertation finally proposed two real applications of stochastic resonance energy harvesting. First, stochastic resonance energy harvester for oil drilling applications is presented. Energy harvester for smart tires is also proposed. The results show that larger power output and wider bandwidth can be obtained by applying the proposed harvesting strategy to the rotating syste

Acknowledgments

I would like to express my sincere gratitude to everyone who helped, supported me in this endeavor. Without them, I won't be able to accomplish this work.

I would like to give great thanks to my advisor, Professor Lei Zuo. It is my luck to have Professor Zuo as my advisor. He has been giving me valuable instructions and guidance, which greatly helps me in the process of this project. His talent and encouragement drive me to convey my enthusiasm to work on the project. His enthusiastic attitude to work also influence me on my work and life.

I also would like to thank Professor Robert Parker, Professor Tomonari Furukawa and Professor Muhammad Hajj for serving on my dissertation committee. Their comments, ideas and suggestions have been very helpful for my research and significantly improved the quality of my dissertation. Also I would like to thanks to Professor Eatherton to borrow Quansar shaker for experiment

I also gratefully acknowledge the funding support from National Science Foundation (NSF) (Grant #1529842 and 1738689).

Next, I propose my appreciation to my lab mates, Hyunjun Jung, Yongjia Wu, Mingyi Liu, Feng Qian, Yu Pan, Yifan Lui, Qiuchi Xiong, Jason Parker, Bonan Qin, Box Jiang, Kan Sun and Jia Mi for providing help and technical discussions. Especially, thanks to Dr. Tai and Dr. Barry for his valuable instructions and guidance.

At last, I want to give my deepest thanks to my family, Seungjo Kim, Kyungsook Lee and Sungeun Kim. Their support and devotion make my life better.

Sincerely

Contents

Acknowledgements v
Contents vi
List of figures ix
List of tables xii
Nomenclature xiii

1. Introduction 1

1.1 Motivation 1

1.2 Objectives and Contributions of the Dissertation 5

1.3 Dissertation Organization 6

2. Background 7

2.1 Chapter introduction 7

2.2 Equivalent model of the rotating system 7

2.3 Vibration characteristics of rotating system 9

2.4 Kramer's problem under rotating environment 11

2.5 Principle of stochastic resonance 13

3. Fokker Planck equation for stochastic nonlinear systems 16

3.1 Chapter introduction 16

3.2 Ito form of stochastic equation 16

3.3 Solving stochastic equation using ode solver 18

3.4 Transformation of stochastic equation using Kramers-Moyal expansion 20

3.5 Solving FPK equation through finite element method 23

4. Influences of magnitude of weak periodic signal on the stochastic resonance 26

4.1 Chapter introduction 26

4.2 Influences of magnitude of weak periodic signal on the stochastic resonance 27

4.3 Investigation of dynamics of stochastic nonlinear system 30

4.4 Chapter summary 37

5. Stochastic resonance energy harvesting for general rotating shaft 38

5.1 Chapter introduction 38

5.2 Stochastic resonance in general rotating shaft 38

5.3 Effect of potential asymmetry due to centrifugal force 41

5.4 Magnetic enhanced stochastic resonance energy harvesting strategy 46

5.5 Experiment verification 50

5.6 Chapter summary 55

6. Self tuning stochastic resonance energy harvesting for smart tire 56

6.1 Chapter introduction 56

6.2 Self tuning stochastic resonance induced via a centrifugal stiffening effect 56

6.3 Stochastic resonance for modulated noise 63

6.4 Numerical simulation of smart tire energy harvester 68

6.5 Experimental verification with rotating platform 71

6.6 Field test results 75

6.7 Chapter summary 78

7. Conclusion and Future work 79

References 81

Appendices 89
Appendix A: Equation of motion for rotating beam 89
Appendix B: Signal to noise ratio of general rotating system 95
Appendix C: Calculation of average power from probability density function 96

List of figures

Figure 1.1. Failure of rotating machinery 1

Figure 1.2. Smart health monitoring system 1

Figure 1.3. Energy harvester for tire using piezo electric patch 3

Figure 2.1 Equivalent mechanical representation of a rotating system 8

Figure 2.2.Vibration response of the rotating system presented in chapter 2.2……..9

Figure 2.3. Schematic representation of a bi stable potential excited by noise input 11

Figure 2.4. Schematic representation of energy harvesting excited by both noise input and periodic signal 13

Figure 2.5 Description of stochastic resonance 14

Figure 2.6 Effect of stochastic resonance 15

Figure 3.1 Convergence problem of classical Euler-Murayama method on stochastic nonlinear equation 18

Figure 3.2 Iso-parametric shape function for solving FPK equation 24

Figure 3.3 Finite element mesh used for the solution of equation (3.5) 24

Figure 3.4 Convergence study of FEM solution and comparison with analytical prediction from Kramer's formula 24

Figure 4.1 Comparison of analytical and numerical SNR under different ratio for fixed parameters 28

Figure 4.2 Critical RPN under different dimensionless stiffness 29

Figure 4.3 Time response of displacement for stochastic resonance energy harvester 31

Figure 4.4 Power output of stochastic resonance energy harvester 32

Figure 4.5 Probability density plot of stochastic resonance harvester 33

Figure 4.6 Experiment setup 34

Figure 4.7 Time response of stochastic resonance energy harvester 34

Figure 4.8 Power output of stochastic resonance energy harvester 35

Figure 4.9 Probability density plot of stochastic resonance harvester 36
Figure 5.1 Vibrations in a rotating shaft..... 38
Figure 5.2 Vibration response from stick-slip in various rotating shaft system..... 39
Figure 5.3 Compare of stochastic resonance in symmetric and asymmetric potential……..…40
Figure 5.4 Phase trajectories of the system 43
Figure 5.5 Time response of the system……...……43
Figure 5.6 Comparison of amplitude spectrum in asymmetric potential and symmetric potential.....44
Figure 5.7 The working range of the harvester with respect to various rotation speeds..……45
Figure 5.8 Stochastic resonance energy harvesting concept for rotating shaft.....……...46
Figure 5.9 Comparison of dimension in deep down hole ..... .46
Figure 5.10 Experiment configuration of symmetric and asymmetric potential ..... .47
Figure 5.11 Potential energy curve for different rotating speed… ..... .47
Figure 5.12 Experiment setup of stochastic resonance energy harvester with magnet 50
Figure 5.13 Experiment setup to measure force-displacement curve.....51
Figure 5.14 Nonlinear restoring force-displacement fitting curve 51
Figure 5.15 Comparison of the amplitude spectrum between simulation with system identification and experiment 52
Figure 5.16 Comparison of amplitude spectrum in the asymmetric potential energy harvester (without magnet) and the symmetric potential energy harvester (with magnet) 52
Figure 5.17 Time response of the experiment setup.....53
Figure 5.18 Frequency sweep test result..... 54
Figure 6.1 Self-tuning stochastic resonance energy harvester for rotating tires.....57
Figure 6.2 Magnetic flux simulation performed by FEMM 58
Figure 6.3 Schematic diagram of inward oriented rotating beam energy harvester 59
Figure 6.4 Bistability of self-tuning harvester.....62
Figure 6.5 SNR versus rotation speed Ω to investigate effect of self tuning 65
Figure 6.6 Stochastic resonance frequency versus driving frequency for noise excitation.....65

Figure 6.7 Comparison of stochastic resonance frequency determined by analytical SNR and numerical 66
Figure 6.8 Numerical simulation of power output for real tire environment 70
Figure 6.9 Equivalent horizontal rotating platform for tire energy harvesting 71
Figure 6.10 Experiment setup of stochastic resonance harvester for modulated noise 72
Figure 6.11 Displacement and reaction force measurement results 72
Figure 6.12 Voltage output of harvester respect to driving speed 73
Figure 6.13 Frequency sweep test results 73
Figure 6.14 Energy harvester prototype for field test 75
Figure 6.15 Results from the field test 75
Figure 6.16 Energy harvesting circuit implementation 76
Figure 6.17 Test of energy harvesting circuit with self tuning energy harvester 77

List of table

Table 1.1. Ambient vibration energy and power requirements for various rotating system……..2
Table 6.1 Parameters of example harvester 1 66
Table 6.2 Parameters of energy harvester using in simulation 68

Nomenclature

m	Mass of energy harvester
c	Dissipative damping in energy harvester
k_1	Linear stiffness of energy harvester
k_3	Cubic stiffness of energy harvester
x	Displacement output of system
N	Gaussian white noise
D	Noise intensity
ε	Magnitude of periodic signal
Ω	Driving frequency
r_k	Kramer's rate
f_{SR}	Stochastic resonance frequency
Ω_0	Angular frequency at the top of barrier
Ω_b	Angular frequency at the two stable point
U	The potential function of the bi-stable oscillator
ΔU	The potential barrier height
S	The magnitude of the output power spectrum
P	Probability density function
$n_{\pm}$	The populations in each equilibrium x_+ and x_-
$I_{\pm}$	Transition rates between the state x_+ to x_-
q	The nondimensional magnitude of periodic force
α_0	The decaying constant of auto correlation
S_x	Spectrum of output signal s
S_n	Noise spectrum
ϵ_1	Normalized displacement
$\bar{c}$	Normalized damping
$\bar{k}_1$	Dimensionless linear stiffness
$\bar{k}_3$	Dimensionless nonlinear stiffness

σ	Dimensionless noise intensity
$\overline{P}$	Dimensionless power
ζ	Modal damping
β	Dimensionless rotating speed
K	Modal noise coefficient
E	Electrical tuning ratio in a dual-mass vibration system
I	Inertial of cantilever beam
ρ	Density of beam
A	Area of beam
μ	Dimensionless mass of tip mass
φ	Shape function
α	Dimensionless radius of disk
ξ	Random number
θ	Voltage constant of the electromagnetic energy harvester
l	Length of beam
V	Vehicle moving velocity

1. Introduction

1.1 Motivation

Rotating system are used in various rotary machines to transmit rotational motion and power, such as in oil drilling strings, steam turbines, tire, and Hard disk. The nature of rotary machines makes these systems constantly subject to cyclic loading and hence highly susceptible to fatigue. Figure 1.1 shows examples of failure in the rotating systems. The development of health monitoring and prognostic systems for rotating shafts play an important role in preventing catastrophic events. Figure 1.2 shows the overall structure of smart health monitoring system. One major challenge to the development is the lack of reliable energy sources to power remote sensors in the field [1]. As an alternative type of energy source to traditional batteries, energy harvesting from ambient vibrations has become a promising solution to power remote sensors [2-3].

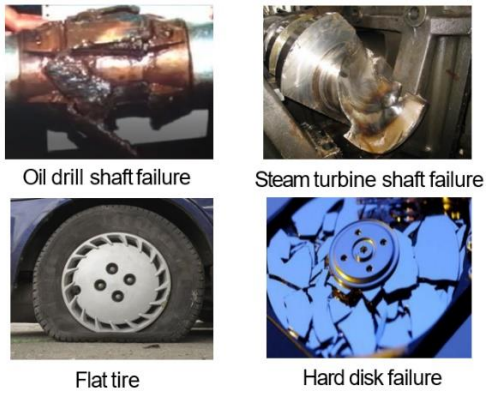

Figure 1.1. Failure of rotating machinery.

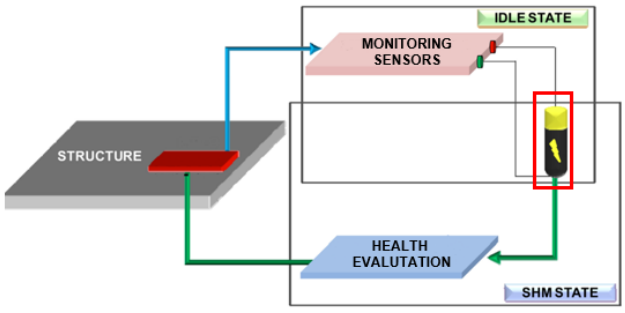

Figure 1.2. Smart health monitoring system [2].

Application	Power requirement	Ambient vibration energy
Smart tire	~30 mW	~200 W
Oil drilling	~ 100 mW	~1200 W
Turbine shaft	~ 150 mW	~6000 W
Wind turbine	~ 50 mW	~2000 W
Helicopter blades	~ 150 mW	~5000 W

Table 1.1. Ambient vibration energy and power requirements for various rotating systems [23-28].

Table 1.1 presents the power requirements and existing ambient vibration energy in various rotary systems. It clearly shows that the requirements easily achieved through vibration energy harvester. However, there are three barriers to efficiently harvesting energy from rotating systems: a) *Large centrifugal force*, b) *Noise interference*, and c) *Time-varying rotation speed*. Due to high-speed rotation, the centripetal acceleration on a rotary machine can be large (~200 g at 500 rpm [17]). Large centrifugal force causes large plastic deformation that diminishes the performance of energy harvester. Therefore, when placing a vibration energy harvester, like those in [19-20], on a shaft or wheel, only a small amount of energy would be generated. Furthermore, vibrations on a tire or wheel are very noisy because the roughness of a road is a stochastic process (zero-mean, stationary Gaussian random process [4]). This is a major issue because traditional harvesters rely on resonance and have notoriously low efficiency when subject to noisy excitations (Figure 1.3). Finally, traditional energy harvesters achieve optimal performance via tuning the resonance frequency to match the excitation frequency of the host [16]. However, the excitation frequency of a shaft or wheel changes along with the rotation speed [18].

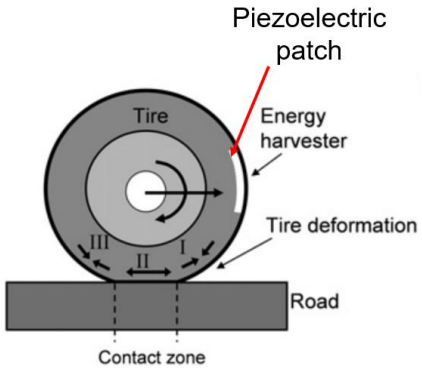

Figure 1.3. Energy harvester for tire using piezo electric patch [18].

Stochastic resonance can be a promising solution to this problem. Stochastic resonance is a physical phenomenon which is manifest in nonlinear bi-stable systems whereby a weak periodic signal can be significantly amplified with the aid of inherent noise or vice versa. Currently, research on stochastic resonance is prosperous in many fields, such as physics, chemistry, biomedical science and engineering [24]. Given its nature, stochastic resonance appears very suitable for the current application as random and periodic vibrations often exist simultaneously in many rotating system applications.

In fact, some pioneering researchers have exploited stochastic resonance to harvest energy from random excitations. McInnes *et al*. [25] firstly suggested the possibility of improving the performance of nonlinear bi-stable harvesters using stochastic resonance and provided a numerical analysis to support such a proposition. By adding a periodically modulated excitation to a randomly excited bi-stable harvester, it has been found that the power is improved by about eight times over the power of the same harvester without stochastic resonance. Following this fundamental work, a bi-stable harvester was designed by Zhang *et al*. [26-27] to experimentally demonstrate stochastic resonance as a strategy for stochastic energy harvesting.

However, the existing research on stochastic resonance energy harvesting assumes *symmetric* potential function of the bi-stable harvester and considers *constant-frequency* excitations, which is insufficient to address several critical issues concerning the current application. Firstly, although torsional vibrations provide periodic excitations essential to stochastic resonance, they impose a *constant offset* (i.e., centrifugal force) to distort the symmetric potential function of the harvester, leading to potential function asymmetry. Many studies have already shown that potential function asymmetry will significantly deteriorate stochastic resonance [30,34]. Nonetheless, all these studies consider overdamped systems

where inertia is neglected. As vibration energy harvesting is meant to convert kinetic energy into electricity, inertia effects cannot be neglected. To the best of the authors' knowledge, in terms of random vibration energy harvesting, the only understanding is that when a bi-stable harvester is subject to additive white noise, potential function asymmetry always decreases optimal power generation . The influence of potential function asymmetry on a stochastic resonance harvester remains unknown. Secondly, in real-world applications, the rotation speed of machine often experiences acceleration (run-up) or deceleration (run-down) before it can reach a targeted value, which is equivalent to frequency up-sweep or down-sweep excitations. How frequency-sweep influences stochastic resonance is also an unanswered question.

Also, current stochastic resonance approaches are insufficient to support practical energy harvesting in rotating systems. Traditionally, studies related to stochastic resonance concentrated on inherent noise, such as white noise, in which many important theories were developed [35-37]. Consequently, when Zheng et al. [29] spearheaded application of stochastic resonance to energy harvesting in rotating tires, they inappropriately considered the noise excitation from road roughness as stationary white noise. In fact, for the several applications [6-10], noise excitation should be amplitude- and frequency-modulated by the angular position and rotational speed, respectively. Stochastic resonance under amplitude- or frequency-modulated noises is still an unanswered question and casts a great academic challenge with practical importance.

1.2 Objectives and Contribution of the Dissertation

The objectives of the dissertation are listed below:

1. Propose a new energy harvesting strategy to obtain sufficient power under a rotating environment. Theoretically and experimentally verify the feasibility of the proposed energy harvesting strategy.
2. Analyze how stochastic resonance changes under various conditions so that stochastic resonance can be applied to the real environment. The influence of the periodic signal to noise ratio on stochastic resonance will be investigated.
3. Develop energy harvesters for oil drilling and smart tire application where there is a large demand for energy harvesting. To verify the superiority of the proposed energy harvesting strategy, comparing the performance of proposed energy harvesters with conventional ones.

The research accomplished in this dissertation includes:

1) The dissertation revealed that stochastic resonance is particularly favorable to energy harvesting in rotating systems. Both numerical and experimental results show that stochastic resonance energy harvester has higher power and wider bandwidth than linear harvesters under a rotating environment.
2) The dissertation provides an analysis of how stochastic resonance changes for the various types of excitation that occur in real-world applications. Under the non-gaussian noise, the stochastic resonance frequency is shifted larger value. Furthermore, the co-existence of the vibrational & stochastic resonance is observed depending on the periodic signal to noise ratio.
3) Propose energy harvester for the general rotating shaft. For the oil drilling application, the periodic force in rotating shafts is biased, leading to potential function asymmetry. Numerical simulation shows that symmetric potential showed nearly seven times higher power output than the asymmetry cases. To solve the problem, an external magnet was placed above the bi-stable energy harvester to compensate for the biased periodic signal.
4) A self-tuning stochastic resonance energy harvester for the smart tire is proposed. The noise intensity in the rotating tire is amplitude-modulated, therefore, classical stochastic resonance theory cannot apply for this case. The dissertation provides a new analysis method based on signal to noise ratio (SNR). The results show that the stochastic resonance frequency for amplitude-

modulated noise is shifted to low value because total excited energy is decreased. To maintain optimal power generation over a wide range of rotating speed, a passively tuned system is implemented in a rotating tire via centrifugal force. An inward-oriented rotating beam is used to induce bistability via the centrifugal acceleration of the tire.

The research in this dissertation has several scientific merits. (1). it has the potential to revolutionize the approach of stochastic resonance energy harvesting in the rotating environment. (2). The new-developed energy harvesting strategy can be extended to the design of the energy harvester for general mechanical systems. (3). the research is interdisciplinary since it blends concepts of mechanical engineering and electrical engineering. It will bridge several separate areas and create new multidisciplinary knowledge.

1.3 Dissertation Organization

The introduction of this dissertation is presented in Chapter 1. Chapter 2 introduces the background of the rotating dynamics and stochastic resonance. Then, Chapter 3 proposes a method for solving stochastic nonlinear equations using the finite element method. In Chapter 4, further investigations of stochastic resonance are presented. In Chapter 5, a stochastic resonance energy harvester for the general rotating shaft is proposed. In Chapter 6, a self-tuning stochastic resonance energy harvester for the smart tire is proposed. The conclusions and future works of this project are stated in Chapter 7.

2. Background

2.1 Chapter Introduction

In this chapter, the theoretical backgrounds of stochastic resonance and rotating dynamics are investigated to establish the framework of stochastic resonance energy harvesting for rotary systems. Background knowledge of rotary dynamics reviewed in chapter 2.2. In chapter 2.3, their vibration characteristics are investigated based on rotary dynamics. The results show that stochastic resonance is a promising solution for energy harvesting in the rotating system. In chapter 2.4, Kramer's problem is examined under the rotating environment. In chapter 2.5, Background knowledge of stochastic resonance will be introduced in chapter 2.5. Through the numerical simulation, the feasibility of the stochastic resonance energy harvesting is verified.

2.2 Equivalent model of the rotating system

General rotating system can be classified to two categories. First one is shaft type which can be found on oil drilling or steam shaft. The other one is disk type which can be found on smart tire or hard disk. If radius of the system (R) is much larger than length of the system (L), the system can be categorized to disk type. Otherwise, the system can be considered to shaft type. There are no exact criteria for distinguishing disk and shaft but general rule of sum is R ≈ 5L. If R >> 5L, system can be considered as disk. When R << 5L, it can be categorized to shaft.

Using equivalent modeling of rotating system presented in Fig 2.1 the dynamic equation can be derived as

$$m\ddot{x}+(c_m+c_e)\dot{x}-k_1 x+k_3 x^3= f(t) \quad (2.1)$$

(a) (b)

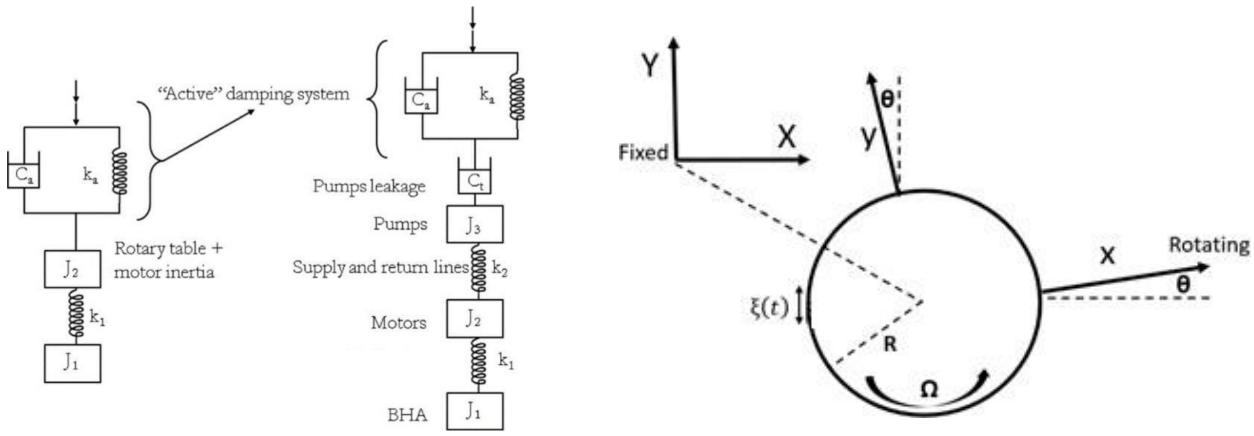

Figure 2.1. Equivalent mechanical representation of a rotating system. (a) Shaft type (b) Disk type

where m, k_1, and k_3 are equivalent mass, linear stiffness, and cubic stiffness of the bi-stable harvester respectively, c_m is mechanical damping coefficient, c_e is electrical damping coefficient and f(t) is external excitations. (Force or base excitation)

2.3 Vibration characteristics of rotating system

Figure 2.2 shows vibration response of rotating system using equation (2.1).

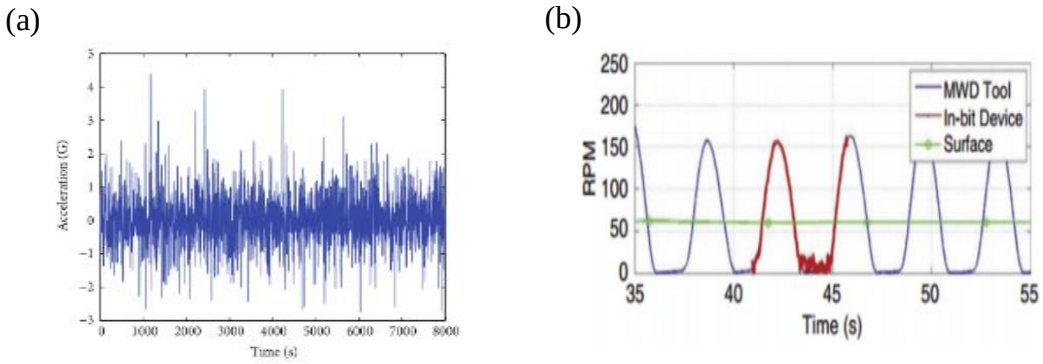

Figure 2.2 Vibration response of the rotating system presented in chapter 2.2. (a) Random Whirl vibration (b) Periodic stick-slip vibration

For the shaft case, two types of vibrations are observed in the simulation results: Random whirl vibration and periodic stick-slip vibration.

Whirl vibrations are typically caused by fluid-structure interactions between the shaft and surrounding fluid media, such as oil film between a shaft and journal in hydrodynamic journal bearings [49] and drilling mud between a drilling string and borehole wall during oil drilling process [66]. When the shaft receives a disturbing force such as a sudden surge of fluid pressure or external shock, the disturbance can lead to centripetal forces, driving the shaft ahead of or behind its nominal rotation speed in a forward or backward circular motion and resulting in a whirling path around the bearing within the bearing clearance. The fluid motion is typically nonstationary and possibly turbulent. Consequently, whirl vibrations often possess stochastic or random characteristics. For examples, Fig. 2.2 displays the vibration responses due to whirling, recorded from three real-world examples of rotating machines, including oil drilling string [50,65] and crankshaft for diesel engine [67]. As seen in Fig. 2.2, all the vibrations are highly random.

Stick-slip vibrations, on the other hand, are often periodic. Figure. 2.3 shows the vibration responses due to stick-slip, recorded from the same systems in Fig. 2.2. As shown in Fig. 23, on contrary to random whirling, all the stick-slip vibrations are periodic. Stick-slip vibration arises when the static friction is high. It is characterized by alternation of the stick phase and slip phase. At the stick phase, the shaft comes to standstill because of the high static friction. Torsional energy is stored because of the shaft is continuously driven at the same time. When this torsional energy exceeds the static friction, the shaft

enters the slip phase and its rotating speed accelerating into maximum. After that, the rotating speed decreases because of dynamic friction and returns to the stick phase again. As a result, the rotating speed of the shaft fluctuates periodically [51]. Although stick-slip vibrations are not purely harmonic in the real world but are periodic. Since stochastic resonance also occurs under non-harmonic periodic signals, it is possible to use a stick-slip vibration as a weak periodic signal to induce stochastic resonance.

As investigated so far, rotation system has two dominant vibrations: Whirl (random) and weak periodic signal (Stick-slip). Therefore, stochastic resonance harvesting promising solution to harvest sufficient energy in the rotating system.

2.4 Kramer's problem under rotating environment

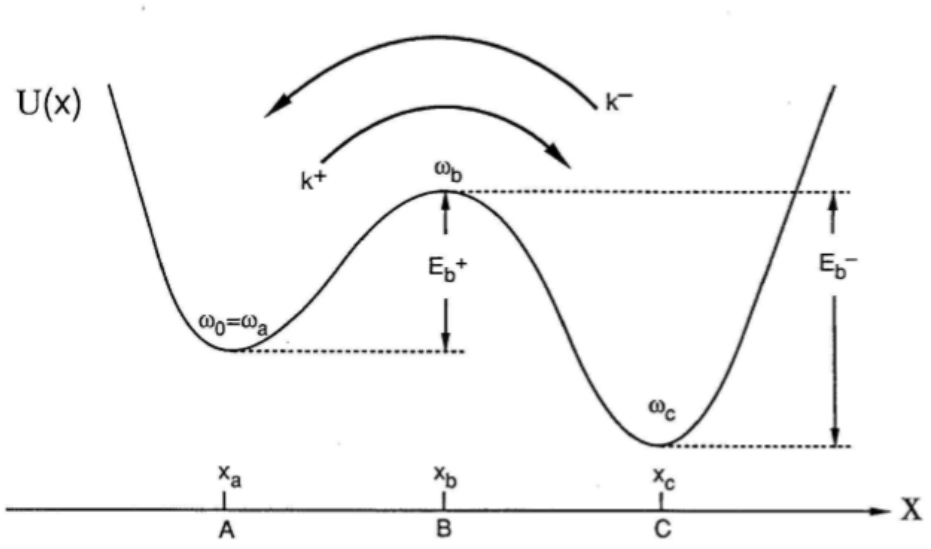

Figure 2.3. Schematic representation of a bi stable potential excited by noise input [37].

Before moving to stochastic resonance, we will examine the case where only noise excitation is applied to the bistable system. Kramer investigated this problem for the thermal escape problem. [36] Here, we will examine the problem using two state-approach. The answers to these questions rely on an analytical expression of the signal-to-noise ratio (SNR) who se maximum corresponds to stochastic resonance [35]. To derive the SNR, we will employ the two-state approach [41]. The solution process is briefly described as follows.

Let $n_{\pm}(t)$ be the populations in each equilibrium x_+ and x_- of the bi-stable oscillator under stochastic excitations, defined as $n_+(t) = \int_0^\infty P(x,t)dx$ and $n_-(t) = 1 - n_+(t)$, respectively, where $P(x,t)$ is the probability density function of the oscillator displacement x. According to [40], $n_{\pm}(t)$ are governed by the *master equation* for the probability distribution:

$$\frac{dn_-(t)}{dt} = -\frac{dn_+(t)}{dt} = W_+(t)n_+ - W_-(t)n_- \qquad (2.2)$$

where $W_+(t)$ and $W_-(t)$ are the nonstationary transition rates from the state x_+ to x_- and from the state x_- to x_+, respectively. Eqn. (2.2) is a first-order ordinary differential equation whose closed-form solutions are available as long as $W_+(t)$ and $W_-(t)$ are known. In other words, the SNR completely relies on the transition rates that can be obtained by solving the Fokker-Planck equation [43]

$$\partial_t P(x,t) = -\partial_x\{[k_1 x - k_3 x^3 - \varepsilon\cos(\Omega t)]P(x,t)\} + \mathrm{D}\partial_x^2\{\cos(\Omega t)P(x,t)\} \tag{2.3}$$

Eqn. (2.3) yields the explicit expression of the transition rate

$$W(t) = \frac{1}{\mathrm{Dcos}(\Omega t)}\int_{-1}^{1}\exp\left[\frac{\Phi(x)}{\mathrm{Dcos}(\Omega t)}\right]dx\int_{-\infty}^{x}\exp\left[-\frac{\Phi(y)}{\mathrm{Dcos}(\Omega t)}\right]dy \tag{2.4}$$

where $\mathrm{Dcos}(\Omega t)$ is the modulated noise intensity and $\Phi(x)$ is an integral of the potential function of the bi- stable oscillator. Finally, Eqs. (2.2) and (2.4) will be used to find the maximum and bandwidth of the SNR. Note that the weak periodic force does not have to be harmonic [56]. The linear stiffness ($-k_1$) and cubic stiffness (k_3) result from the double-well potential of the bi-stable oscillator. Finally, c is the damping of the oscillator. The double-well potential is created by the magnetic interaction between the tip magnet and the fixed magnet. The oscillation of such a cantilever beam in single DOE modelling is represented by the particle motion in the double-well potential. If there is only random excitation, noise induced hopping will occur according to the following transition rate r_k, also known as Kramer's rate.

2.5 Principle of Stochastic resonance

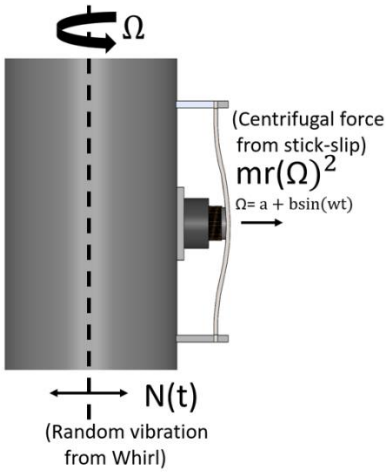

Figure 2.4. Schematic representation of energy harvesting for rotating system excited by both noise input and periodic signal.

Now suppose that periodic signal added to the system with bistable energy harvester. (Fig 2.4) The dynamic equation of the energy harvester is written as

$$m\ddot{x}+c\dot{x} - k_1x + k_3x^3 = N(t)+\varepsilon\sin(\Omega t) \tag{2.5}$$

The left-hand side of Eq. (2.5) indicates the bi-stable oscillator, and $N(t)$ and $\varepsilon\sin(\Omega t)$ are inherent noise and weak periodic excitation, respectively. The linear stiffness $(-k_1)$ and cubic stiffness (k_3) result from the double-well potential of the bi-stable oscillator. Finally, c is the mechanical damping of the oscillator. Referred to Fig. 4 a typical bi-stable cantilever beam consisting of a double-well potential is created by the magnetic interaction between the tip magnetic and the fixed magnetic. It follows that the oscillation of the cantilever beam is represented by the particle motion in the double-well potential. If there is only random excitation, noise induced hopping will occur according to the following transition rate r_k, also known as Kramer's rate introduced in previous chapter,

$$r_k = \frac{w_0 w_b}{2c} e^{\left(-\frac{\Delta U}{D}\right)} , \tag{2.6}$$

where D is the noise strength, $w_0 = \sqrt{\frac{U'(0)}{m}}$, $w_b = \sqrt{\frac{U'(\pm x_b)}{m}}$, $\Delta U = \frac{{k_1}^2}{4k_3}$, and , $U = \frac{1}{2}k_1x^2 + \frac{1}{4}k_3x^4$ is the potential function of the bi-stable oscillator.

When the potential barrier is much higher than the noise strength (ΔU / D »1), the transition rate becomes smaller, which means that there is very little hopping (Fig.2.4 (a)), and intra-well motion dominates. If a weak periodic force is subsequently applied to the system, the double-well potential is periodically tilted up and down by the periodic force. When the average waiting time (amount of time until next hopping occurs) $T_K = \frac{1}{r_k}$ is matched with the half of the forcing period T_Ω, noise-induced hopping between the potential wells becomes synchronized with the periodic tilting, and then the particle mass will persistently roll back and forth between the potential wells, indicating the onset of stochastic resonance. Pictorial illustration is given in Fig 2.5

$$2T_K = \frac{2}{r_k} = T_\Omega = 1/f_{SR} \qquad (2.7)$$

Let us point out the mechanism of stochastic resonance. When a weak periodic signalis applied to a bistable system, it serves to periodically modulate the potential by raising and lowering the wells as shown in Fig.2.3. Essentially, the additive forcing changes alternately the relative depth of the potential wells, increasing the probability of jumps between wells twice per modulation period. At a critical value of the noise intensity, the particle in a well arrives at the neighborhood of the local maximum (barrier), almost

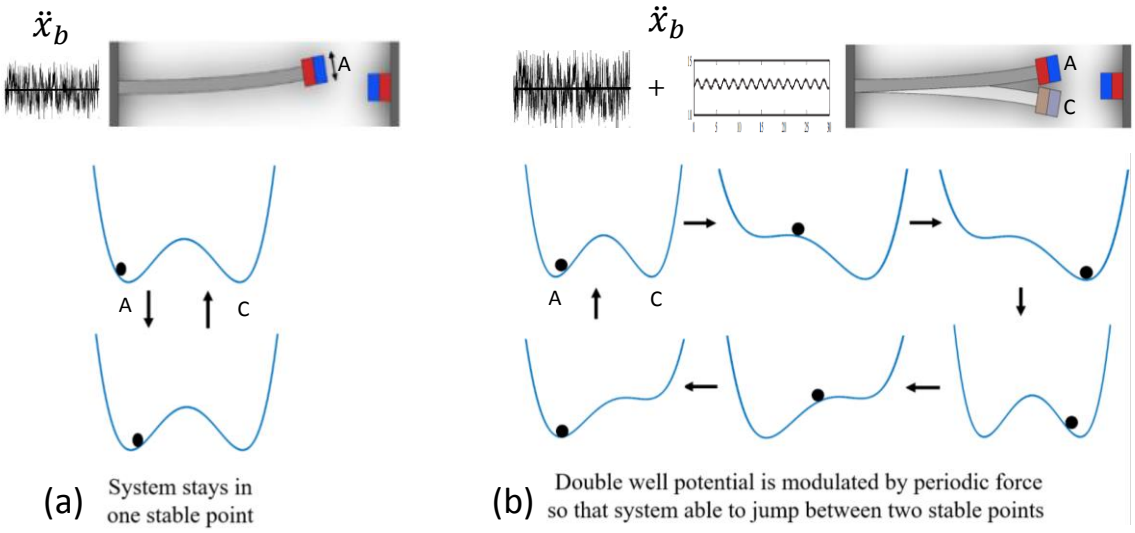

Figure 2.5. Description of stochastic resonance: (a) Intra-well motion (b) Inter-well motion.

when the barrier height seen by it is minimum so that the noise is able to push it to the other well. Thus, there is a synchronization between the periodic

force and the output signal resulting in a periodic switching of the particle from one well to another well. The essential ingredients for stochastic resonance consists of a nonlinear system, a weak signal and a source of noise. In bistable systems, the underlying mechanism of stochastic resonance is easily appreciated. The oscillator in Eq. (2.25) has a double-well potential $V(x_1) = \frac{1}{2}k_1x_1^2 + \frac{1}{4}k_3x_1^4$. When the particle is only excited by weak noise ($\varepsilon = 0$), it oscillates around an equilibrium point (intra-well motion) until accumulating enough kinetic energy to escape to another equilibrium point (inter-well transition), as shown in Fig. 2. 3(a). If a weak periodic force is added to the system ($\varepsilon \neq 0$), the double-well potential is periodically tilted up and down, as shown in Fig. 2. 3(b). When the transition rate (also known as *Kramers' rate*) $r_k = 1/\tau_\epsilon$ of the noise-induced escape becomes synchronized with the periodic tilting, the particle will roll back and forth between the potential wells (in the statistical average), manifesting stochastic resonance. As a result of synchronization, stochastic resonance can only occur when the average hopping time $T_K = 1/r_k$ is synchronized with half of the forcing period T_Ω [55], i.e., $2T_K = {}^2/_{r_k} = T_\Omega$.

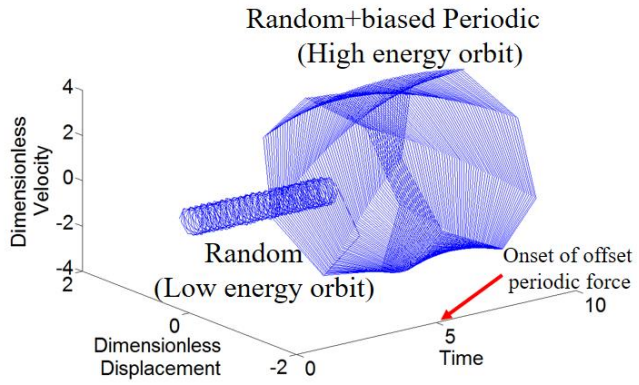

Figure 2.6. Effect of stochastic resonance (SR): Before 5s, only noise is excited to the system. After 5s, periodic excitation added with noise excitation which leads to stochastic resonance.

Figure. 2.6 illustrates the phase trajectory of the dimensionless displacement and velocity of bistable energy. Before t=5s, the system was vibrating at a low energy intra-well orbit, but at t=5s a periodic force is introduced. The system jumps into a high energy inter-well orbit after t=5s. Therefore, large output can be achieved by adding bistable energy harvester to the rotating system.

3. Fokker Planck equation for stochastic nonlinear systems

3.1 Chapter introduction

As introduced earlier, the stochastic term is included in the equation of motion, which is not easy to solve with a typical ode solver. In this chapter, we will learn how to solve nonlinear stochastic ordinary differential equations (SODE) using the Fokker-Plank-Kolomov (FPK) equation. First, differential form of stochastic equation (Ito form) is introduced with its theoretical background. In chapter 3.3, nonlinear SODE is solved using Runge-Kutta 4th order method. The results clearly show that R-K solver will fail to solve nonlinear SODE. Mathematician found a way to solve the equation by transforming the original stochastic ordinary differential equation to deterministic partial differential equation (FPK equation). In chapter 3.4, Kramers–Moyal expansion method is introduced to transform SODE to FPK equation. In chapter 3.5, FPK equation is solve using Iso-parametric FEM(Finite element method) formulation.

3.2 Ito form of stochastic equation

Stochastic calculus is the field of mathematics used for the modeling of random systems. Most of random process are based on continuous non-smooth function. This makes impossible to use typical derivative process because they are unable to be defined on non-smooth function. Ito provides theory of integration where integral equations do not require derivative process. It is called *Ito calculus*. The detail theoretical background of Ito calculus is introduced in reference [84].

Using Ito calculus, equation (2.25) can be written as differential form as following,

$$d\epsilon_1 = \epsilon_2 dt$$

$$d\epsilon_2 = (-\bar{c}\epsilon_2 - \mu\epsilon_1 + \theta{\epsilon_1}^3 + q\sin(wt))dt + \sigma dW, \qquad (3.1)$$

where W is a Brownian motion process such that $\frac{dW}{dt} = \xi(t)$.

The equation normalized as following parameters,

$\epsilon_1 = \frac{x}{r}$, $\bar{c} = \frac{c_m + c_e}{\sqrt{mk_1}}$, $\mu = \frac{k_1}{m(r_k)^2}$, $\rho = \frac{k_2}{m(r_k)^2 r}$, $\theta = \frac{k_3}{m(r_k)^2 r^2}$, $\sigma = \frac{\sqrt{2D}}{(r_k)^2 r}$, $q = \frac{a}{r_k}$

Referred to a typical bi-stable cantilever beam, where the double-well potential is created by the magnetic interaction between the tip magnet and the fixed magnet. The oscillation of such a cantilever beam in single DOE modelling is represented by the particle motion in the double-well potential. If there is only random excitation, noise induced hopping will occur according to the following transition rate r_k, also known as Kramer's rate. The stick-slip vibration is forcing the oscillator in terms of centrifugal force $mr(\Omega_0 + \Omega_1\sin(wt))^2$. Mathematically speaking, the centrifugal force should be a function of the displacement x as well, i.e., $r = r' +$, and give rise to a parametric excitation $m(\Omega_0 + \Omega_1\sin(wt))^2 x$ to the harvester. However, in common practice, the magnitude of $m(\Omega_0 + \Omega_1\sin(wt))^2$ is much less than the linear stiffness k_1. For example, when the proposed energy harvester (to be shown in Sec. 4) is operating at a common shaft rotation speed, the maximum magnitude of $m(\Omega_0 + \Omega_1\sin(wt))^2$ is less than 3% of k_1 (6.32 N/m vs. 275 N/m); hence the parametric excitation effect can be neglected for simplicity. Therefore, the centrifugal force is considered as a function of the effective radius throughout this paper. Also, the inductance of the electromagnetic harvester is ignored so that the energy harvesting circuitry can be effectively modeled as electrical damping c_e [49].

Contrary to the general case, periodical forces in rotating shaft has a constant offset. The constant offset will distort the symmetric potential to an asymmetric one. In the case of a typical periodic force without constant offset, the potential well is appropriately modulated to favor inter-well hopping well

3.3 Solving stochastic equation using ode solver

In this section, equation 3.1 is solved numerically using Euler-Murayama method.

(a) (b)

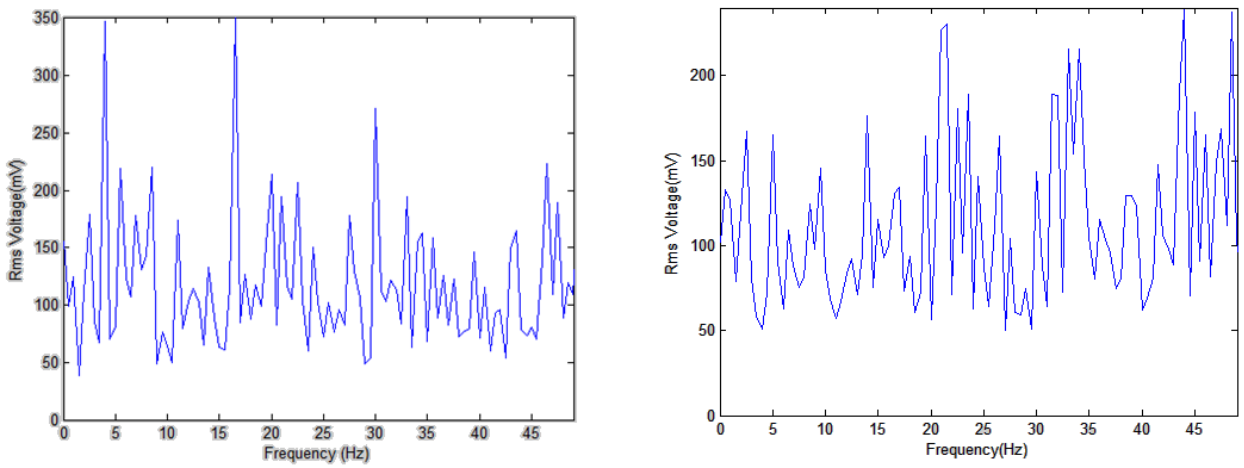

Figure 3.1 Convergence problem of classical Euler-Murayama method on stochastic nonlinear equation. (a) 1st trial (b) 2nd trial with same condition

Figure 3.1 shows the results of solution for stochastic equation (3.1) is not converge with Euler-Murayama method. There are some difference between up-sweep and down-sweep. In the case of up-sweep, the peak is shifted a little to right and a jump phenomenon (a phenomenon suddenly entering the lower branch from the higher branch) occurs in the higher frequency band. In the down-sweep case, the peak is shifted to the left and the jump phenomenon happens in the lower frequency band. Therefore, the hysteretic effect is observed in the presented energy harvester. Also, stochastic resonance occurs for both up-sweep and down-sweep cases. The experiment results show the similar trend as the numerical simulation although there is a little error (10% in peak values) between them. SNR(β, β_i^*) of three traditional harvesters each of which has constant linear and cubic stiffness coefficients $k_1((\beta_i^*)^2)$ and $k_3((\beta_i^*)^2)$, where β_i^* denotes a specific driving speed and $i = 1,2,3$, are also plotted in dashed and dotted lines. There are several things worth noting in Fig. 6. First, the peaks of SNR(β, β_i^*) correspond to stochastic resonance of the traditional harvesters. In this regard, the rotation speed β_i^{max} that corresponds

to the peak, i.e., SNR(β_i^{max}, β_i^*)=max(SNR(β, β_i^*)) and max(·) denotes the maximum operator, is considered as the stochastic resonance frequency at a specific rotation speed β_i^*; in other words, one can define the stochastic resonance frequency as $f_{SR}(\beta_i^*) = \beta_i^{max}$. Second, since SNR($\beta, \beta$) of the self-tuning harvester is computed by continuously tuning linear and cubic stiffness coefficients, the solid curve can be obtained by connecting SNR(β^*, β^*) of the traditional harvesters within a range of β^* of interest. As such, if SNR(β, β^*) intersects with SNR(β, β) at its peak, the self-tuning harvester is within the self-tuning region wherein the harvester achieve the maximum attainable power at a specific rotating speeds. SNR(β, β_1^*) and SNR(β, β_2^*) (dashed curves) are two examples of such cases. As seen, the peaks of the dashed curves coincide with the solid curve, indicating that the self-tuning harvester is perfectly tuned to achieve stochastic resonance at these two driving speeds (β_1^* and β_2^*). On the other hand, if SNR(β, β^*) does not intersect at the peak, the self-tuning harvester leaves the self-tuning region and is considered as "off-tuned". SNR(β, β_3^*) (dotted curve) is one example of such cases. As seen, the peak of the dotted curve deviates from the solid curve, indicating that the harvester is off tuned at this specific driving speed (β_3^*).

3.4 Transformation of stochastic equation using Kramers-Moyal expansion

Typical method for solve SODE not works well for nonlinear problem because stochastic term causes numerical instability. Mathematician found a way to solve the equation by transforming the original equation to other equation which is more easier to deal with. By applying transform, an original stochastic ordinary differential equation is converted to deterministic partial differential equation. In this chapter, Kramers–Moyal expansion method is introduced to transform SODE to FPK equation.

In stochastic process Kramers-Moyal expansion method indicate the Taylor series expansion of the original equation. [85]. This expansion transform integro-differential original equation to partial differential equation.

Applying Kramers Moyal expansion to equation (3.1), the FPK equation can be derived from the above stochastic ordinary differential equation, i.e.,

$$\frac{\partial P}{\partial t} = -\epsilon_2 \frac{\partial P}{\partial \epsilon_1} + 2\bar{c}\frac{\partial(\epsilon_2 P)}{\partial \epsilon_2} + (-\mu\epsilon_1 + \rho{\epsilon_1}^2 + \theta{\epsilon_1}^3 - (s + q\sin(wt))^2) + \frac{\partial P}{\partial \epsilon_2} + \sigma\frac{\partial^2 P}{\partial {\epsilon_2}^2}, \qquad (3.2)$$

where $P(\epsilon_1, \epsilon_2)$ is the probability density function of ϵ_1 and ϵ_2.

Upon solving Eq. (3.2), average displacement and velocity (also power) can be obtained by calculating the statistical moment of the probability density function P.

A constant quadratic stiffness k_2 was passively chosen to compensate the centrifugal force to enhance power generation. In this regard, the rotation speed of the shaft was held at a reference value (optimal rotation speed). However, in common practice, rotation speed is never held at a reference value; hence the centrifugal force will change as the rotation speed changes. As a result, the constant quadratic stiffness k_2 can no longer compensate the centrifugal force properly, resulting in decrease in power. To identify the working range of the harvester, we performed simulation to calculate generated power of the harvester at various rotation speeds. The threshold of working range was defined by using the -3dB criteria (i.e., 0.707*peak power). It shows generated power of the harvester at ±30% of the optimal rotation speed. The power decreases as the rotation speed moves away from the optimal rotation speed, indicating the effect of k_2 is weaken. With the -3dB criteria, the working range is identified as ±10% of the optimal rotation speed. In this section, we propose a novel energy harvesting strategy that particularly suits rotating shafts, which not only takes advantage of stochastic resonance, but also compensates the constant

offset in the periodic vibration by using magnetic force. The harvester is attached on a rotating shaft. It consists of a post buckled beam, a metal cylinder wound with copper coil installed to the mid-span of the beam, a magnet fixed to the side wall of a rotating shaft, and a pair of magnets fixed to the top of the harvester frame and to the mid-span of the beam respectively.

Real size of the harvester is relatively small compared to the shaft. The length of the harvester is 1m. Typical oil drill pipe weighs about 10 kg/m (6.65lb/ft) while our harvester weighs about 0.09 kg. Considering the section of the shaft in effect, the shaft can be modeled as a rotating disk and the harvester can be as a point mass. It follows that the rotating inertia of the shaft section is about 0.0288 kg· m^2 while that of the harvester is about 0.00038 kg· m^2; hence the rotating inertia of the harvester is 1.3% of the drill pipe, which means that the harvester contributes little to the dynamics of the rotating shaft.

To emulate the real-world applications, the shaft is simultaneously subject to a random whirl vibration $N(t)$ and a periodic stick-slip torsional vibration of $\Omega = \Omega_0 + \Omega_1 \sin wt$, where Ω_0 is a constant rotation speed (offset) and $\Omega_1 \sin wt$ is a sinusoidal fluctuation to approximate the torsional vibration at a fluctuation frequency w. As a result, the centrifugal force $mr\Omega^2$ will excite the harvester, where m is the mass of the coil and r is the effective radius from the harvester to the shaft axis.

The post-buckled beam creates the double-well potential necessary for stochastic resonance. When excited by the whirl (random noise) and stick-slip vibration (periodic signal), the beam will undergo large oscillation due to stochastic resonance. Consequently, the attached coil will rapidly pass though the side wall magnet, generating electricity due to electromagnetic transduction.

The periodic excitation (centrifugal force) for a rotating shaft is offset by a constant value. To resolve the issue, an external force is needed to compensate the offset. In this paper, we employ a pair of magnets to compensate the constant offset; It shows the potential energy curves of the bi-stable beam with and without the magnet. The potential well of the harvester is originally symmetric (blue solid line) when the shaft is at rest ($\Omega = 0$). When the rotational speed $\Omega = \Omega_0$, it becomes asymmetric (red solid line). Finally, with the appropriate external magnetic force, it becomes symmetric again (green dashed line). Note that the magnetic force was not explicitly modeled. Instead, it was included in the total nonlinear restoring force ($-k_1 \text{ x} + k_2x^2 + k_3 x^3$) which is the sum of magnetic force and the nonlinear restoring force of the buckled beam. This nonlinear restoring force includes quadratic term to compensate potential asymmetry due to centrifugal force. Special attention has to be given that the constant offset due to centrifugal force

is implemented as constant acceleration in the following experiment section due to limitation of our current equipment

3.5 Solving FPK equation through finite element method

Discretizing Eq. (3.4) by FEM yields a set of ordinary differential equations (ODE) governing the probability density function of each element $\mathbf{P} = [P_1, P_2, \cdots, P_e, \cdots]$, where P_e is the probability density function of element e (3.4). He and Daqaq [94] pointed out that responses of a nonlinear bi-stable oscillator subject to Gaussian white noise is very different from the Gaussian process, and typical statistic linearization will fail to solve the governing stochastic equation. They instead proposed a finite element method (FEM) to solve the Fokker-Plank-Kolomov (FPK) equation of the bi-stable oscillator. In the following, we will apply this method to our problem. Unlike the case in [95], our problem includes periodic forces in addition to random excitations to investigate stochastic resonance. The FPK equation deals with random vibration problems by transforming a stochastic ordinary differential equation into a deterministic partial differential equation that governs the probability density function of displacement ϵ_1 and velocity ϵ_2 of the bi-stable system.

$$\mathbf{M}\dot{\mathbf{P}}+\mathbf{K}\mathbf{P} = \mathbf{A}(\mathrm{s} + \mathrm{q}\sin(\mathrm{wt}))^2, \tag{3.3}$$

where M_{kl}, K_{kl}, A_{kl} are

$$\mathrm{M}_{kl} = \int_A N_k N_l \, \mathrm{d}\epsilon_1 d\epsilon_2, \; \mathrm{A}_{kl} = \int_A \frac{\partial N_k}{\partial \epsilon_2} N_l \mathrm{d}\epsilon_1 d\epsilon_2 ,$$
$$\mathrm{K}_{kl} = \int_A -\epsilon_2 \frac{\partial N_k}{\partial \epsilon_1} N_l \mathrm{d}\epsilon_1 d\epsilon_2 + \int_A (\bar{c}\epsilon_2 - \mu\epsilon_1 + \rho{\epsilon_1}^2 + \theta{\epsilon_1}^3) \frac{\partial N_k}{\partial \epsilon_2} N_l \mathrm{d}\epsilon_1 d\epsilon_2 + \sigma \int_A \frac{\partial N_k}{\partial \epsilon_2} \frac{\partial N_l}{\partial \epsilon_2} \, \mathrm{d}\epsilon_1 d\epsilon_2 \tag{3.4}$$

The shape function N_k, N_l are chosen to be iso-parametric function which is unity at nodes *k*, *l*, and *A* is the area of each element. (Figure 3.2)

$$\boldsymbol{N_1} = \frac{(\boldsymbol{b}-\boldsymbol{x_1})(\boldsymbol{h}-\boldsymbol{x_2})}{\boldsymbol{4bh}}, \; \boldsymbol{N_2} = \frac{(\boldsymbol{b}+\boldsymbol{x_1})(\boldsymbol{h}-\boldsymbol{x_2})}{\boldsymbol{4bh}}, \; \boldsymbol{N_3} = \frac{(\boldsymbol{b}-\boldsymbol{x_1})(\boldsymbol{h}+\boldsymbol{x_2})}{\boldsymbol{4bh}}, \; \boldsymbol{N_4} = \frac{(\boldsymbol{b}+\boldsymbol{x_1})(\boldsymbol{h}+\boldsymbol{x_2})}{\boldsymbol{4bh}} \tag{3.5}$$

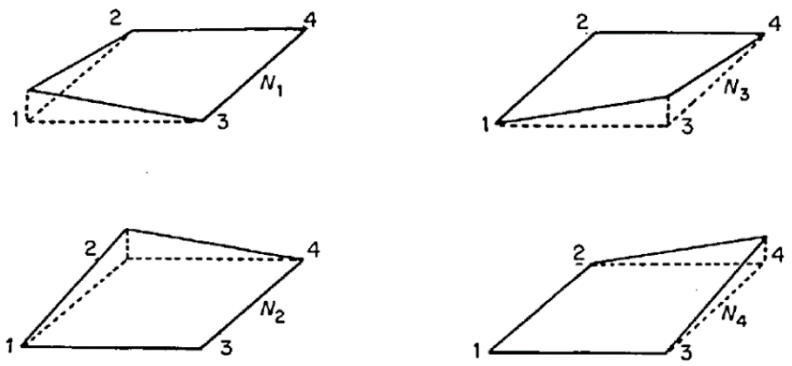

Figure 3.2 Iso-parametric shape function for solving FPK equation [96].

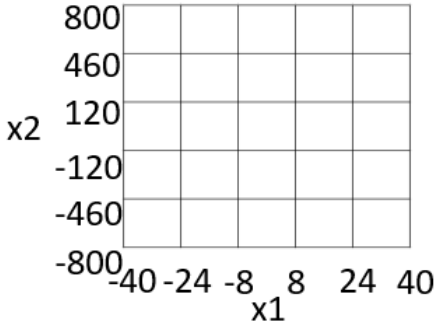

Figure 3.3 Finite element mesh used for the solution of equation (3.5).

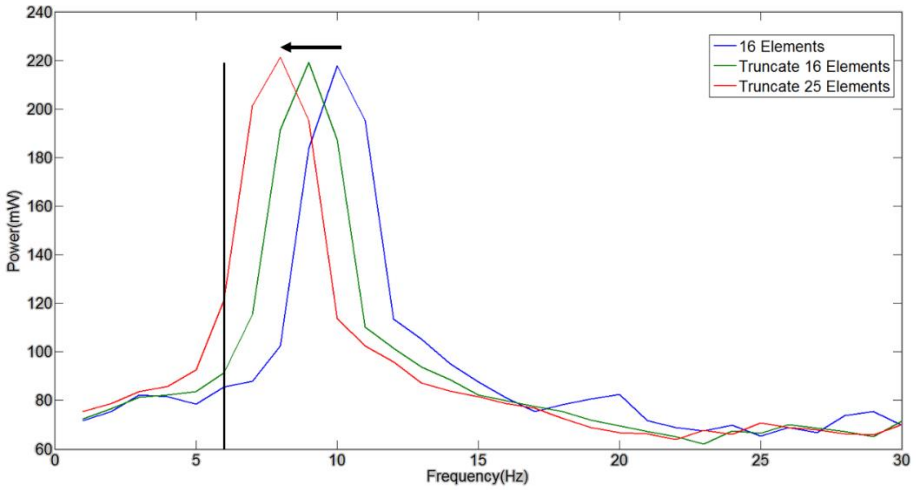

Theoretical SR frequency: 5.8 Hz (Predicted by Kramers formula $f_{SR}=\frac{w_0 w_b}{4\pi c} e^{(-\frac{\triangle U}{D})}$)

Figure 3.4 Convergence study of FEM solution and comparison with analytical prediction from Kramer's formula.

Convergence study of FEM method is carried to verify its performance. As the number of element increased, peak frequency is approaches 5.8 Hz which is Theoretical SR frequency predicted by Kramer's formula. This results verifies feasibility of FEM approaches.

4. Influences of magnitude of weak periodic signal on the stochastic resonance

4.1 Chapter introduction

In this chapter, we investigate the influences of the ratio between the weak periodic signal magnitude and input noise intensity, called RPN, on dynamics and stochastic resonance energy harvesting. The existing research on stochastic resonance energy harvesting assumes the magnitude of the periodic signal is 'weak'. Gammaotini et al [83] defined the 'weak' periodic magnitude as the magnitude that does not cause inter-well motion between a bistable system. However, there is no discussion on the exact criteria for 'weak' periodic signal magnitude. Since the ratio between the weak periodic signal magnitude and input noise intensity (called RPN) varies in real environments, it is necessary to define the exact criteria for 'weak' periodic signal magnitude. Another question is 'If RPN is larger than the critical value, how do the dynamics of the system change?' If the periodic signal magnitude is much larger than noise intensity, the system exhibits similar dynamics as a typical bi-stable energy harvester. However, none of the aforementioned works investigated the dynamics of the system when the magnitude of the periodic signal is "intermediate" level. In response to the limitations of the state-of-the-art, we will for the first time address these issues that must be considered before one can practically apply stochastic resonance to harvest energy from the environment. Specifically, the influence of the ratio between the magnitude of the weak periodic signal and noise intensity on the dynamics of the system will be investigated. Also, the exact criteria for weak periodic signal magnitude are established. The experiment setup was also built to verify the simulation.

4.2 Critical value of weak periodic magnitude

In this chapter, we will establish criteria for magnitude of periodic signal stochastic resonance. The criteria are determined as the RPN value that the difference between analytical SNR and numerical SNR started to become larger. Since analytical SNR presented in section 2.2 based on classical stochastic resonance theory [24], it is no longer valid when periodic signal of the system is not 'weak' anymore.

Numerical SNR is obtained from the frequency response of the system. Equation of motion is normalized as follows.

$$\ddot{\epsilon}_1+\bar{c}\dot{\epsilon}_1-\bar{k}_1\epsilon_1+\bar{k}_3{\epsilon_1}^3=\sigma\ \xi(t)+q\sin(wt) \qquad (4.1)$$

where $\xi(t)$ is the unit white noise with $\langle\ \xi\ (0),\ \xi\ (t)\ \rangle= 2\delta(t)$, and the dimensionless variable and parameters are

$$\epsilon_1 = \frac{x}{r}, \bar{c}=\frac{c_m+c_e}{\sqrt{mk_1}}, \bar{k}_1 = \frac{k_1}{m(r_k)^2}, \bar{k}_3 = \frac{k_3}{m(r_k)^2r^2}, s=\frac{\varepsilon}{r_k}$$

Numerical SNR is calculated from the numerical output responses of Equation (4.1). Specifically, it is obtained from ratio of numerical output power spectrum of ϵ_1 to noise power spectrum of σ (t).
We define the ratio of the periodic signal magnitude to noise intensity (RPN) as

$$\text{RPN} = \frac{q}{\sigma} = \frac{(r_k)^2 r\varepsilon\sqrt{\frac{k_1}{k_3}}}{D\sqrt{2D}} \qquad (4.2)$$

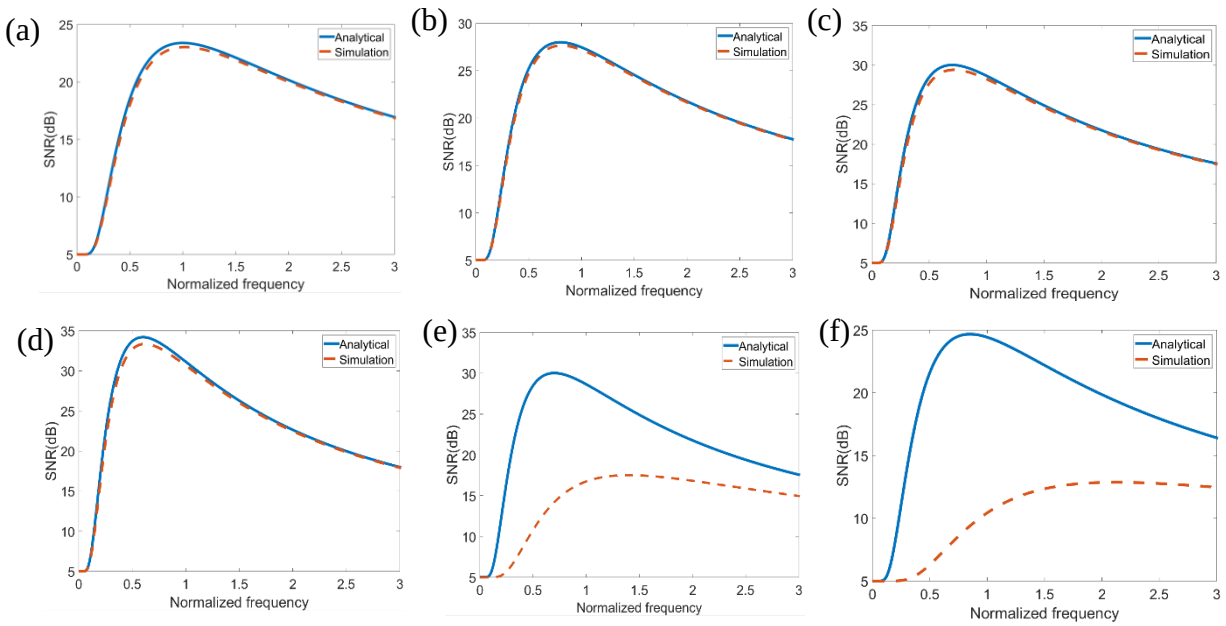

Figure. 4.1 Comparison of analytical and numerical SNR under different ratio for fixed parameters.

$\bar{k}_1$=1, $\bar{k}_3$=1, $\bar{c} = 1$

(a) $\frac{q}{\sigma}$ = 0.1, (b) $\frac{q}{\sigma}$ = 0.15, (c) $\frac{q}{\sigma}$ = 0.2, (d) $\frac{q}{\sigma}$ = 0.25, (e) $\frac{q}{\sigma}$ = 0.28, (f) $\frac{q}{\sigma}$ = 0.35

Figure 4.1 presents a comparison of analytical and numerical SNR under fixed parameters. When PNR ($\frac{q}{\sigma}$) is smaller than 0.28, analytical and numerical SNR matches well. When PNR ($\frac{q}{\sigma}$) become larger than 0.28, however, the error started to become larger which means the system no longer described by classical stochastic resonance theory.

(a) (b)

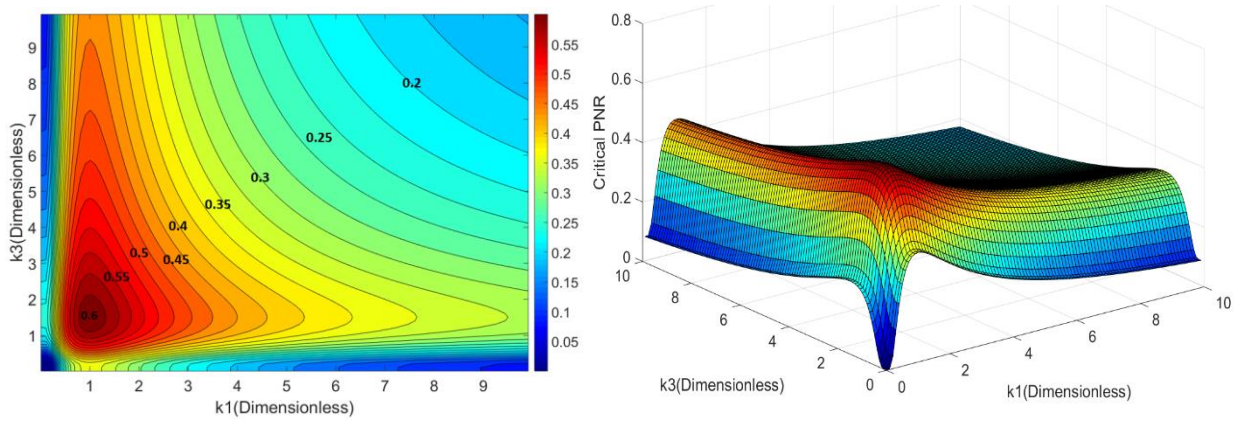

Figure 4.2 Critical RPN under different dimensionless stiffness. (a) Altitude plot (b) 3D plot

Figure 4.2 presents how the critical RPN value changes as the system parameters change. The results are based on numerical SNR obtained from the frequency response of the system. Since damping does not have a significant effect on stochastic resonance [95], only the effects of linear stiffness and nonlinear stiffness are investigated. The critical value of RPN is determined when the average error between analytical SNR and numerical SNR becomes larger than 20%. Figure 4.2 (a) presents results using an altitude plot while Figure 4.2 (b) depicts results through a 3D plot. The results show that critical RPN becomes smaller when both linear stiffness and nonlinear stiffness become large.

4.3 Influence of periodic signal to noise ratio on dynamics of system

In this section, the influence of RPN on the dynamics of the system is investigated. He and Daqaq [42] pointed out that responses of a nonlinear bi-stable oscillator subject to Gaussian white noise is very different from the Gaussian process, and typical statistic linearization will fail to solve the governing stochastic equation. They instead proposed a finite element method (FEM) to solve the Fokker-Plank-Kolomov (FPK) equation of the bi-stable oscillator. In the following, we will apply this method to our problem. Unlike the case in [43], our problem includes periodic forces in addition to random excitations to investigate stochastic resonance. The FPK equation deals with random vibration problems by transforming a stochastic ordinary differential equation into a deterministic partial differential equation that governs the probability density function of displacement ϵ_1 and velocity ϵ_2 of the bi-stable system. The stochastic differential equation (Ito form [84]) of Equation (4.1) is

$$d\epsilon_1 = \epsilon_2 dt$$
$$d\epsilon_2 = (-\bar{c}\epsilon_2 + \bar{k}_1\epsilon_1 - \bar{k}_3{\epsilon_1}^3 + q\sin(wt))dt + \sigma dW, \quad (4.3)$$

where W is a Brownian motion process such that $\frac{dW}{dt} = \xi(t)$.

The FPK equation can be derived from the above stochastic ordinary differential equation, i.e.,

$$\frac{\partial P}{\partial t} = -\epsilon_2 \frac{\partial P}{\partial \epsilon_1} + 2\bar{c}\frac{\partial(\epsilon_2 P)}{\partial \epsilon_2} + (-\mu\epsilon_1 + \bar{k}_1{\epsilon_1}^2 + \bar{k}_3{\epsilon_1}^3 - q\sin(wt))\frac{\partial P}{\partial \epsilon_2} + \sigma\frac{\partial^2 P}{\partial {\epsilon_2}^2}, \quad (4.4)$$

where $P(\epsilon_1, \epsilon_2)$ is the probability density function of ϵ_1 and ϵ_2.

Discretizing Eq. (4.3) by FEM yields a set of ordinary differential equations (ODE) governing the probability density function of each element $\mathbf{P} = [P_1, P_2, \cdots, P_e, \cdots]$, where P_e is the probability density function of element e [96]

$$\mathbf{M\dot{P}} + \{\mathbf{K} - \mathbf{A}\epsilon\sin(\mathbf{wt})\}\mathbf{P} = \mathbf{0}, \quad (4.5)$$

where M_{kl}, K_{kl}, A_{kl} are

$$M_{kl} = \int_A N_k N_l \, d\epsilon_1 d\epsilon_2, \; A_{kl} = \int_A \frac{\partial N_k}{\partial \epsilon_2} N_l d\epsilon_1 d\epsilon_2 ,$$

$$K_{kl} = \int_A -\epsilon_2 \frac{\partial N_k}{\partial \epsilon_1} N_l d\epsilon_1 d\epsilon_2 + \int_A (\bar{c}\epsilon_2 - \mu\epsilon_1 + \theta\epsilon_1^3) \frac{\partial N_k}{\partial \epsilon_2} N_l d\epsilon_1 d\epsilon_2 + \sigma \int_A \frac{\partial N_k}{\partial \epsilon_2} \frac{\partial N_l}{\partial \epsilon_2} d\epsilon_1 d\epsilon_2 \quad (4.6)$$

The shape function N_k, N_l are chosen to be iso-parametric function which is unity at nodes *k*, *l*, and *A* is the area of each element.

Upon solving Eq. (4.6), the average displacement and velocity (also power) can be obtained by calculating the statistical moment of the discretized probability density function **p**. For example, the dimensionless power $\bar{P}$ can be calculated according to the following equation.

$$\bar{P} = \zeta_e < \epsilon_2^2 > = \zeta_e \int_{-q_2 l}^{q_2 h} \int_{-q_1 l}^{q_1 h} \epsilon_2^2 P(\epsilon_1, \epsilon_2) dq_1 dq_2 \approx \zeta_e \sum_i \sum_j \epsilon_{2i}^2 p_{ij} d\epsilon_1 d\epsilon_2 \quad (4.7)$$

where h , l are upper limit and lower limit of integration boundary, q_{2i} and p_{ij} are dimensionless speed and probability density, ζ_e is the electrical damping ratio. Since we used electromagnetic harvester, the inductance of the harvester is ignored so that the energy harvesting circuitry can be effectively modeled as electrical damping ζ_e [97].

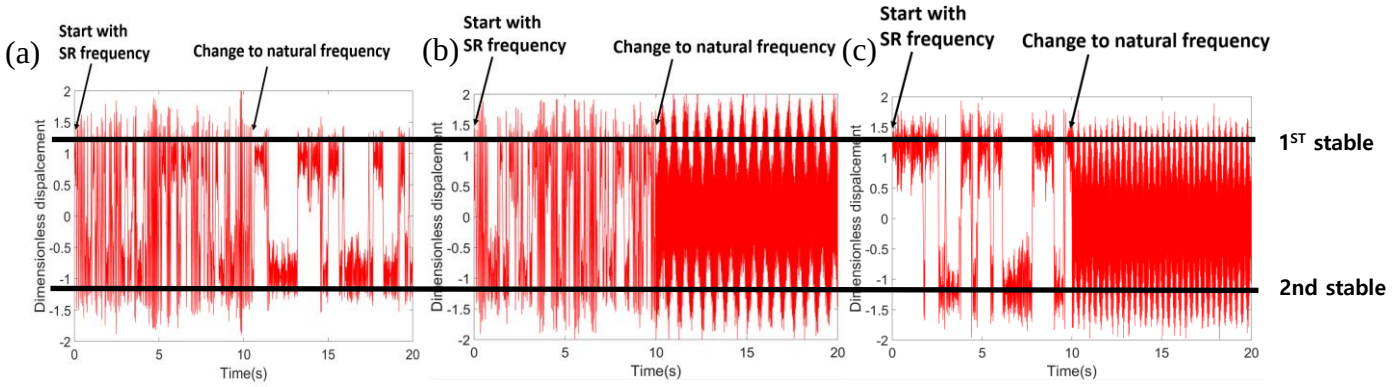

Figure 4.3 Time response of displacement for stochastic resonance energy harvester. (a) $\frac{q}{\sigma}$ = 0.1 , (b) $\frac{q}{\sigma}$ = 1 , (c) $\frac{q}{\sigma}$ = 3

Figure 4.3 shows the time displacement response of the harvester with respect to different RPN values. The frequency of the periodic signal is started from the stochastic resonance frequency (32.3 Hz). At t=10s, the frequency is changed to the natural frequency of the system (21.8 Hz). For Figure 4.3 (a), snap-through motion occurs frequently when the frequency of the periodic signal matches stochastic resonance frequency which leads to stochastic resonance. When the frequency of the periodic signal is changed to the natural frequency, however, snap-through rarely occurs. When RPN becomes larger (Fig 4.3(b)), snap -through occurs for both stochastic resonance frequency and natural frequency. For large RPN value (Fig 4.3 (c)), snap- through only occurs for natural frequency cases.

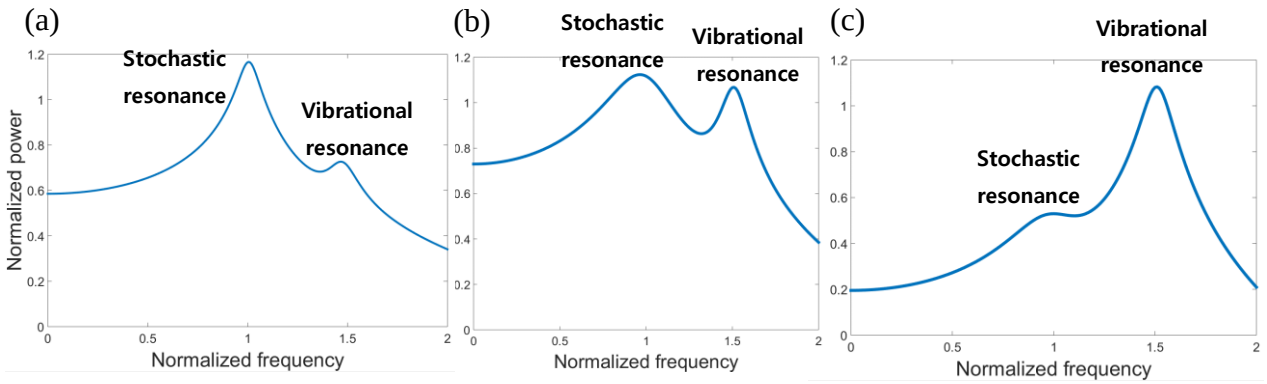

Figure 4.4 Power output of stochastic resonance energy harvester. (a) $\frac{q}{\sigma}$ = 0.1, (b) $\frac{q}{\sigma}$ = 1, (c) $\frac{q}{\sigma}$ = 3

Figure 4.4 presents the power output of stochastic resonance energy harvester respect to different PNR values. When the ratio $(\frac{\varepsilon}{D})$ is small, stochastic resonance is dominant. As the ratio $(\frac{\varepsilon}{D})$ grows larger, both vibrational & stochastic resonance is observed in the system. Vibration resonance occurs in natural frequency (Frequency is normalized at the stochastic resonance frequency) while stochastic resonance occurs in stochastic resonance frequency, which can be called multi resonance phenomena. The phenomena especially advantageous for energy harvesting because wide-bandwidth can be achieved for the system. These results justify the feasibility of creating multi resonance in a bi-stable system as in the case of multiple linear resonant systems.

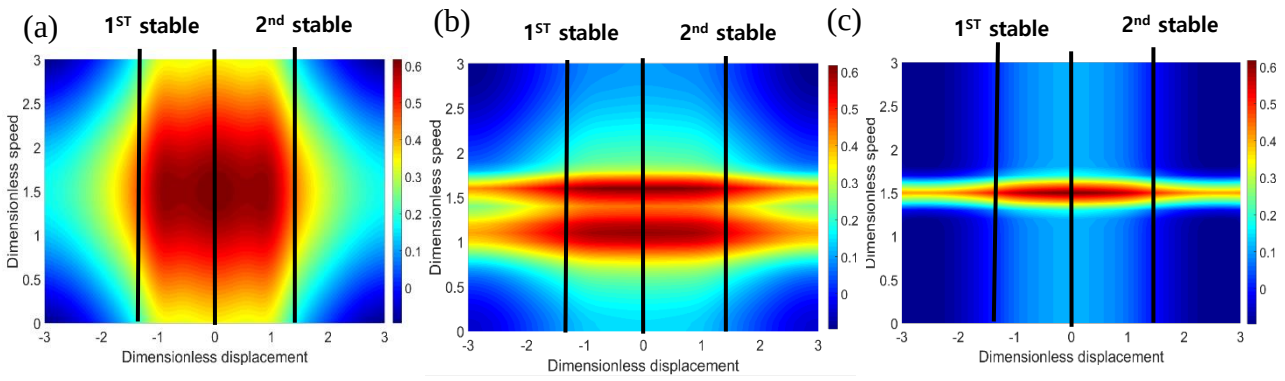

Figure 4.5 Probability density plot of stochastic resonance harvester. (a) $\frac{q}{\sigma}$ = 0.1 (b) $\frac{q}{\sigma}$ = 1 (c) $\frac{q}{\sigma}$ = 3

Figure 4.5 shows the probability density plot of the stochastic resonance energy harvester for different RPN value. The x-axis represents the dimensionless displacement, the y-axis represents the absolute dimensionless velocity. As the value of the density plot becomes higher, the system tends to have corresponding displacement and velocity. As indicated in figure 4.5, stable points of the system are located at -1.25 and 1.25. When RPN ($\frac{q}{\sigma}$) is small, probability density plot spreads over a wide range because the influence of random excitation is dominant. As the RPN becomes larger, the density plot begins to concentrate on a specific region. In the case of Fig. 4.5 (b), the density plot is concentrated in the region where the velocity 1 and 1.6, where 1 is the region due to stochastic resonance and 1.6 is the region due to vibration resonance. When the RPN is large, the system only confined to a narrow region. This is because the system tends to more deterministic as periodic signals becoming dominant.

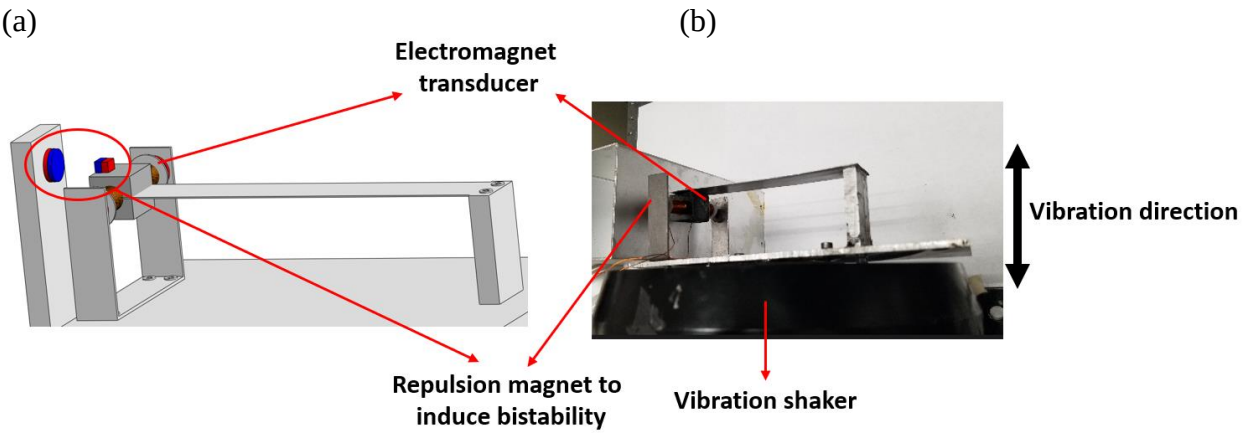

Figure 4.6. Experiment setup. (a) Configuration (b) Bistable harvester installed in the vibration shaker

We built a prototype (Fig. 4.6) to verify the numerical simulation. The prototype consists of a magnet-induced bistable cantilever beam with an electro-magnetic transducer. Beam dimension is 150mm (L) × 25mm (W) × 0.4mm (T). A Sentek vibration shaker is used to drive energy harvester. We input a 0.3~1g white noise to the shaker while adding a 0.05g~1g periodic signal, varying from 5 Hz to 100Hz sweep. Total excitation magnitude is fixed even when RPN values become different.

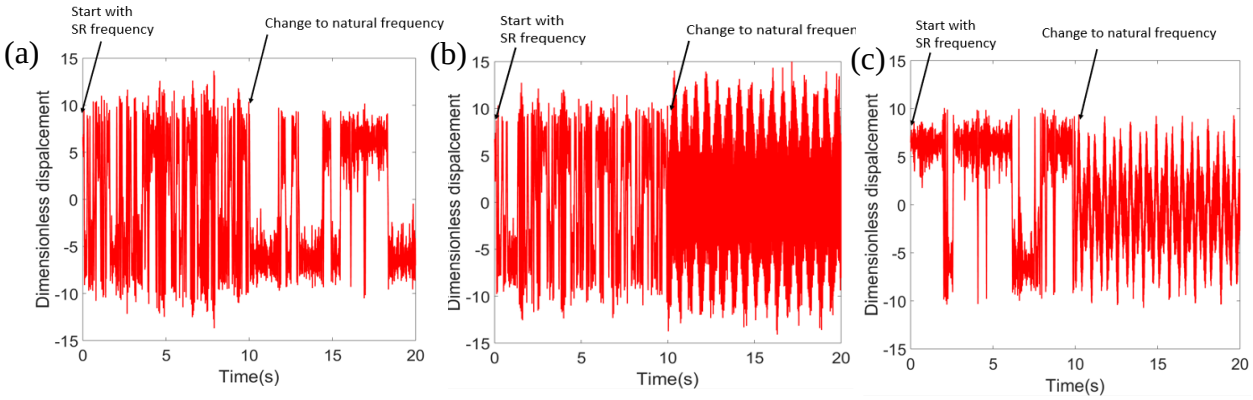

Figure 4.7 Time response of stochastic resonance energy harvester. (a) $\frac{q}{\sigma} = 0.1$, (b) $\frac{q}{\sigma} = 1$, (c) $\frac{q}{\sigma} = 3$

Figure 4.7 shows the power output of stochastic resonance energy harvester respect to different RPN values. Although the experiment results show a similar trend as simulation results, the error between simulation and experiment results become larger when RPN is in the intermediate level. The maximum

error is calculated to be 15%. This is because the classical stochastic resonance theory is no longer valid when RPN is at the intermediate level.

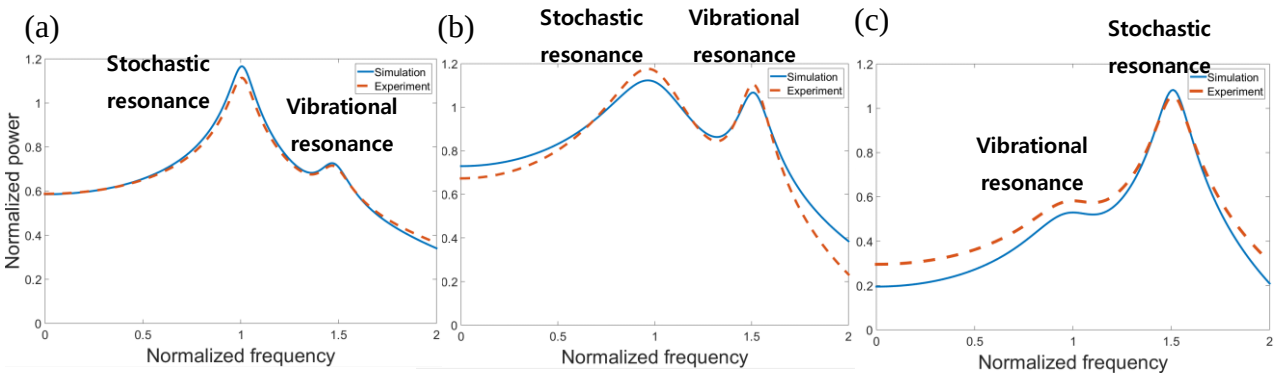

Figure 4.8 Power output of stochastic resonance energy harvester. (a) $\frac{q}{\sigma}$ = 0.1, (b) $\frac{q}{\sigma}$ = 1, (c) $\frac{q}{\sigma}$ = 3

Figure 4.8 shows the probability density plot of the stochastic resonance energy harvester for different RPN value. Compare to simulation results (Figure 4.4), asymmetry is observed for experimental results. This is due to the asymmetry of the experiment setup. However, experiment results still show a similar trend as simulation results.

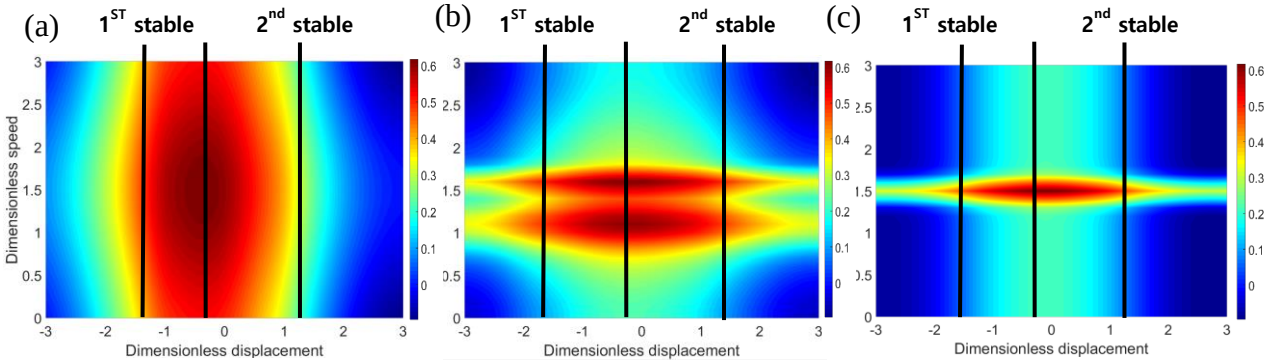

Figure 4.9 Probability density plot of stochastic resonance harvester. (a) $\frac{q}{\sigma}$ = 0.1 (b) $\frac{q}{\sigma}$ = 1 (c) $\frac{q}{\sigma}$ = 3

Figure 4.9 shows the probability density plot of the stochastic resonance energy harvester for different RPN value. Compare to simulation results (Figure 4.5), asymmetry is observed for experimental results.

This is due to the asymmetry of the experiment setup. However, experiment results still show a similar trend as simulation results.

4.4 Chapter summary

In this chapter, we investigated the influences of the ratio of periodic signal magnitude and noise intensity (called RPN) on the dynamics of the system and energy harvesting. First, the criteria of weak periodic signal magnitude are established. The criteria are determined at the RPN value that the difference between analytical SNR and numerical SNR starts to become larger. Depending on the linear and nonlinear stiffness constants of the system, the critical values varies from 0.2 to 0.6. When RPN becomes larger than the critical value, both vibration and stochastic resonances are observed in the system. We refer to the coexistence of such two resonances in a single-DOF bi-stable system as multi-resonance phenomenon. The phenomenon can be very beneficial for energy harvesting because the bandwidth of the system can be increased up to 60% compared to single resonance case. Experiment results show good agreement with the numerical simulation with around 15% of errors, which verifies multi-resonance phenomenon.

5. Stochastic resonance harvesting for general rotating shaft

5.1 Chapter introduction

In this chapter, stochastic resonance is considered to harvest energy from two typical vibrations in rotating shafts: random whirl vibration and periodic stick-slip vibration. A numerical analysis based on a finite element method was conducted to investigate stochastic resonance with potential function asymmetry. An electromagnetic energy harvesting system was constructed to experimentally verify the numerical analysis. System identification was performed to obtain the parameters needed in the numerical analysis.

5.2 Stochastic resonance in general rotating shaft

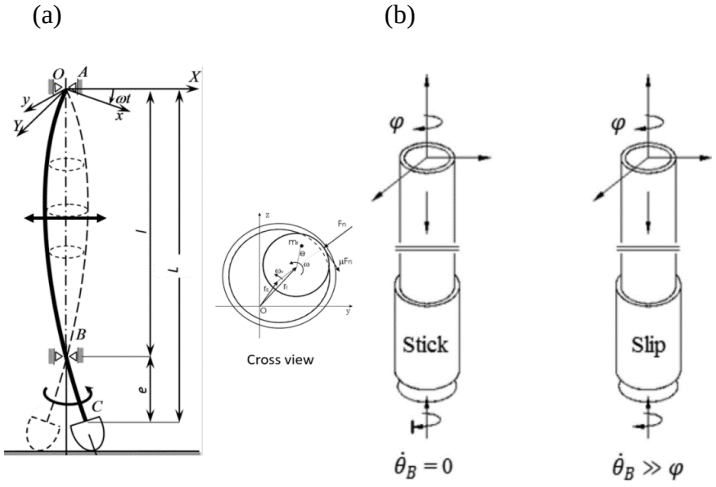

Figure 5.1 . Vibrations in a rotating shaft [68]: (a) Lateral vibration (whirl) (b) Torsional vibration (stick-slip).

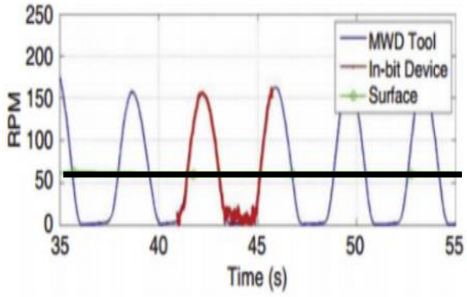

Figure 5.2 Vibration response from stick-slip in various rotating shaft system. (Oil drilling) Solid thick line indicates the offset of the periodic signal [65].

As investigated in chapter 2, the dominant vibration of oil drilling is whirl and stick slip. Therefore, stochastic resonance harvesting can be achieved by adding only a bistable harvester. On contrary to traditional stochastic resonance introduced in chapter 2, stochastic resonance in rotating shafts is more involved, due to whirl and stick-slip vibrations. To simplify the problem, we assume that the bi-stable oscillator is subject to a random whirl vibration $\sqrt{2D}\xi(\mathrm{t})$ with noise intensity D and a stick-slip vibration $\Omega_0 + \Omega_1 \sin(\mathrm{wt})$, where Ω_0 is a constant offset (nominal rotation speed of the shaft) and $\Omega_1 \sin(\mathrm{wt})$ is a fluctuation signal with excitation frequency w due to the alternation between the stick and slip phase.

It follows that if a bi-stable energy harvester is considered in a rotating shaft, the dynamic equation is written as

$$\mathrm{m}\ddot{x}+(c_m+c_e)\dot{x}-k_1\,\mathrm{x}+k_3\,x^3=\mathrm{m}\sqrt{2D}\xi(\mathrm{t})+\mathrm{mr}(\Omega_0+\Omega_1\sin(\mathrm{wt}))^2 \qquad (5.1)$$

where m, k_1, and k_3 are mass, linear stiffness, and cubic stiffness of the bi-stable harvester respectively, c_m is mechanical damping coefficient, c_e is electrical damping coefficient due to energy harvesting circuitry, D is noise intensity, r is the effective radius from the harvester to the shaft axis, Ω_0 is the nominal shaft rotation speed, and Ω_1 and w are magnitude and frequency of the periodic force respectively. It is assumed that the harvester uses electromagnetic transduction to convert vibration energy into electricity.

Note that the stick-slip vibration is forcing the oscillator in terms of centrifugal force $\mathrm{mr}(\Omega_0 + \Omega_1 \sin(\mathrm{wt}))^2$. Mathematically speaking, the centrifugal force should be a function of the

displacement x as well, i.e., $r = r' + x$ in Eq. (5.1), and give rise to a parametric excitation $m(\Omega_0 + \Omega_1 \sin(wt))^2 x$ to the harvester. However, in common practice, the magnitude of $m(\Omega_0 + \Omega_1 \sin(wt))^2$ is much less than the linear stiffness k_1. For example, when the proposed energy harvester (to be shown in Sec. 5.) is operating at a common shaft rotation speed, the maximum magnitude of $m(\Omega_0 + \Omega_1 \sin(wt))^2$ is less than 3% of k_1 (6.32 N/m vs. 275 N/m); hence the parametric excitation effect can be neglected for simplicity. Therefore, the centrifugal force is considered as a function of the effective radius throughout this paper. Also, the inductance of the electromagnetic harvester is ignored so that the energy harvesting circuitry can be effectively modeled as electrical damping c_e [69].

Contrary to the general case, periodical forces in rotating shaft has a constant offset. The constant offset will distort the symmetric potential to an asymmetric one. In the case of a typical periodic force without constant offset, the potential well is appropriately modulated to favor inter-well hopping; see Fig. 5.3 (a). If the periodic force has a constant offset, the double-well potential favors one potential well, resulting in an asymmetric potential well; see Fig. 5.3 (b). Consequently, it becomes difficult to jump from the potential well + to the opposite potential well −, and thus stochastic resonance will become weakened . To resolve the issue, an external force is needed to compensate the offset of the periodic force.

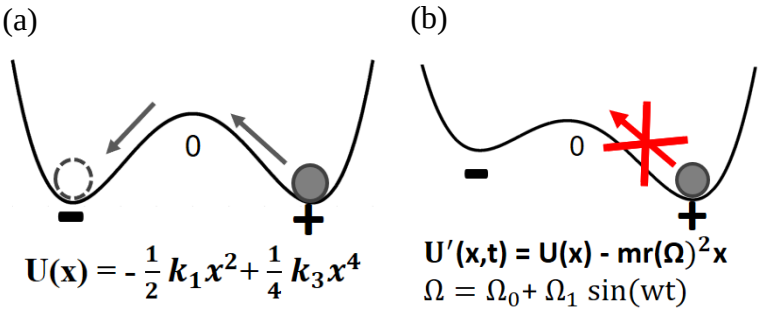

Figure 5.3 Compare of stochastic resonance in symmetric and asymmetric potential. (a) Original symmetric potential when the shaft is at rest (b) Asymmetric potential due to the centrifugal force, resulted from stick-slip vibration

5.3 Effect of potential asymmetry due to centrifugal force

To investigate stochastic resonance with potential function asymmetry, we added a quadratic stiffness k_2x^2 to the original equation (5.2). With appropriate values of k_2, the asymmetric potential.

$$m\ddot{x}+(c_m+c_e)\dot{x}-k_1 x+k_2x^2+k_3 x^3=m\sqrt{2D}\xi(t) + mr(\Omega_0 + \Omega_1\sin(wt))^2 \quad (5.2)$$

He and Daqaq [94] pointed out that responses of a nonlinear bi-stable oscillator subject to Gaussian white noise are very different from Gaussian process, and typical statistic linearization will fail to solve the governing stochastic equation. They instead proposed a finite element method (FEM) to solve the Fokker-Plank-Kolomov equation (FPK) of the bi-stable oscillator. In the following, we will apply this method to our problem. Unlike Daqaq's case, our problem includes periodic forces in addition to random excitations to investigate stochastic resonance. The FPK equation deals with random vibration problems by transforming a stochastic ordinary differential equation into a deterministic partial differential equation which governs the probability density function of displacement x and velocity $\dot{x}$ of the bi-stable system. To facilitate the solution process, Eq. (5.4) is rewritten in a dimensionless form as

$$\ddot{\epsilon_1}+\bar{c}\dot{\epsilon_1}-\mu\epsilon_1+\rho{\epsilon_1}^2+\theta{\epsilon_1}^3= \sigma\,\xi(t)+ (s + q\sin(wt))^2 \quad (5.3)$$

Dimensionless variable and parameters are

$$\epsilon_1 = \frac{x}{r}, \bar{c}=\frac{c_m+c_e}{\sqrt{mk_1}}, \mu = \frac{k_1}{m(r_k)^2}, \rho = \frac{k_2}{m(r_k)^2r}, \theta = \frac{k_3}{m(r_k)^2r^2}, \sigma = \frac{\sqrt{2D}}{(r_k)^2r}, s=\frac{a}{r_k}, q=\frac{b}{r_k}$$

The stochastic differential equation (Ito form) of equation (5.3) is

$$d\epsilon_1= \epsilon_2 dt$$

$$d\epsilon_2= (-\bar{c}\epsilon_2 + \mu\epsilon_1 - \rho{\epsilon_1}^2 - \theta{\epsilon_1}^3 + (s + q\sin(wt))^2)dt + \sigma dW, \quad (5.4)$$

where W is a Brownian motion process such that $\frac{dW}{dt} = \xi(t)$.

The FPK equation can be derived from the above stochastic ordinary differential equation, i.e.,

$$\frac{\partial P}{\partial t} = -\epsilon_2 \frac{\partial P}{\partial \epsilon_1} + 2\bar{c}\frac{\partial(\epsilon_2 P)}{\partial \epsilon_2} + (-\mu\epsilon_1 + \rho{\epsilon_1}^2 + \theta{\epsilon_1}^3 - (s + q\sin(wt))^2)\frac{\partial P}{\partial \epsilon_2} + \sigma\frac{\partial^2 P}{\partial {\epsilon_2}^2}, \quad (5.5)$$

where $P(\epsilon_1, \epsilon_2)$ is the probability density function of ϵ_1 and ϵ_2.

Discretizing Eq. (8) by FEM yields a set of ordinary differential equations (ODE) governing the probability density function of each element $\mathbf{P} = [P_1, P_2, \cdots, P_e, \cdots]$, where P_e is the probability density function of element e [96]

$$\mathbf{M}\dot{\mathbf{P}} + \{\mathbf{K} - \mathbf{A}(s + q\sin(wt))^2\}\mathbf{P} = \mathbf{0}, \quad (5.6)$$

where M_{kl}, K_{kl}, A_{kl} are

$$M_{kl} = \int_A N_k N_l \, d\epsilon_1 d\epsilon_2, \; A_{kl} = \int_A \frac{\partial N_k}{\partial \epsilon_2} N_l d\epsilon_1 d\epsilon_2,$$

$$K_{kl} = \int_A -\epsilon_2 \frac{\partial N_k}{\partial \epsilon_1} N_l d\epsilon_1 d\epsilon_2 + \int_A (\bar{c}\epsilon_2 - \mu\epsilon_1 + \rho{\epsilon_1}^2 + \theta{\epsilon_1}^3)\frac{\partial N_k}{\partial \epsilon_2} N_l d\epsilon_1 d\epsilon_2 + \sigma\int_A \frac{\partial N_k}{\partial \epsilon_2}\frac{\partial N_l}{\partial \epsilon_2} d\epsilon_1 d\epsilon_2 \quad (5.7)$$

The shape function N_k, N_l are chosen to be iso-parametric function which is unity at nodes *k*, *l*, and *A* is the area of each element.

As it was demonstrated in Sec. 5.2, centrifugal force will distort the potential energy of the bi-stable harvester, resulting in potential asymmetry. A reference rotation speed is chosen to conduct the numerical simulation. Upon solving Eq. (5.7), average displacement and velocity (also power) can be obtained by calculating the statistical moment of the probability density function P.

For example, average power can be calculated according to the following equation.

$$\text{<Dimensionless Power>} = \bar{c}_e < {\epsilon_2}^2 > = \bar{c}_e \int_{-\epsilon_2 l}^{\epsilon_2 h}\int_{-\epsilon_1 l}^{\epsilon_1 h} {\epsilon_2}^2 P d\epsilon_1 d\epsilon_2 \approx \bar{c}_e \sum_i \sum_j {\epsilon_2}_i^2 P_{ij} d\epsilon_1 d\epsilon_2 \quad (5.8)$$

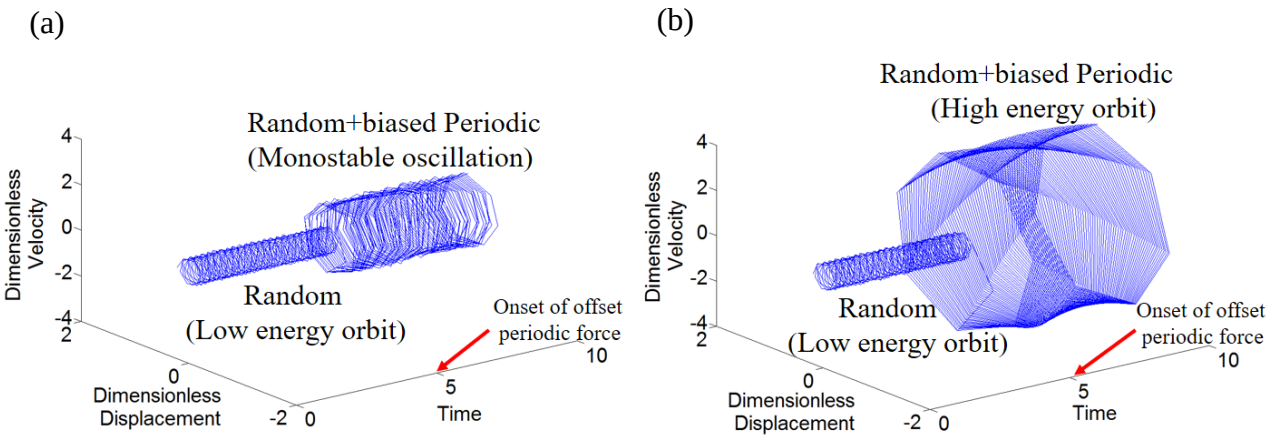

Figure 5.4. Phase trajectories of the system: (a) Asymmetric potential ($k_2 = 0$) (b) Symmetric.

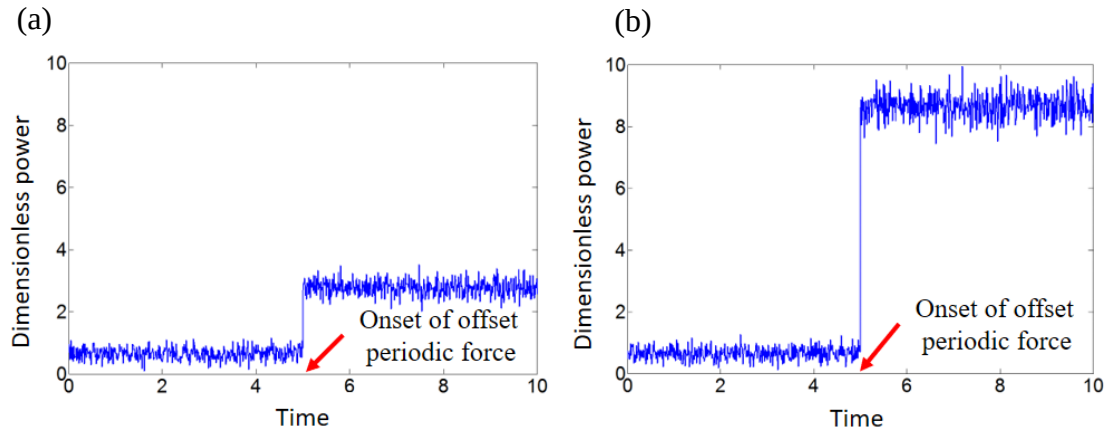

Figure 5.5 Time response of the system: (a) Asymmetric potential ($k_2 = 0$). (b) Symmetric potential ($k_2 > 0$).

To investigate stochastic resonance with potential asymmetry, we solve Eq. (5.5) numerically for symmetric potential and asymmetric potential. Symmetric potential is obtained by choosing a proper value of k_2 to compensate the constant offset in centrifugal force (cf. Eq. (5.6)) while asymmetric potential is obtained by setting $k_2 = 0$.

Figure. 5.6 illustrates the phase trajectory of the dimensionless displacement and velocity of each case. Before t=5s, the system was vibrating at a low energy intra-well orbit, but at t=5s a periodic force with constant offset (in the form of $mr\Omega^2 = mr(\Omega_0 + \Omega_1 \sin wt)^2$) is introduced. In the symmetric potential case, the system jumps into a high energy inter-well orbit after t=5s. For the asymmetric potential case, however, the system remains in low energy orbit. The time responses shown in Fig. 5.6 also confirm this finding. Furthermore, Fig. 5.6 compares the symmetric potential with the asymmetric potential in

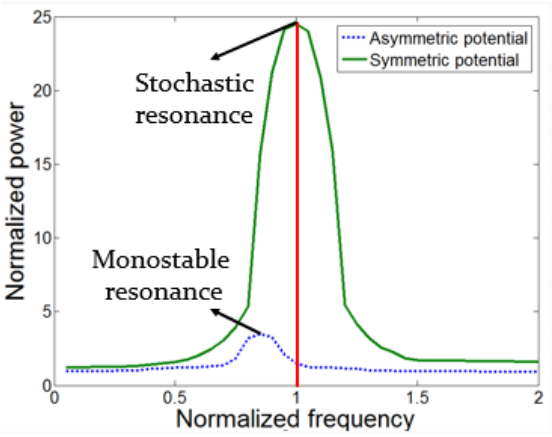

Figure. 5.6 Comparison of amplitude spectrum in asymmetric potential and symmetric potential.

the amplitude spectrum. Electrical damping $\bar{c}_e$ was optimized for both asymmetric potential and symmetric potential case. Note that the excitation frequency is normalized with respect to the stochastic resonance frequency. As expected, the effect of stochastic resonance is significantly reduced in the asymmetric potential case. On the other hand, in the case of symmetric potential, the output of the stochastic resonance is not deteriorated. These results show the stochastic resonance with symmetric potential is much stronger that that with the asymmetric potential. For equation (5.5), a constant quadratic stiffness k_2 was passively chosen to compensate the centrifugal force to enhance power generation. In this regard, the rotation speed of the shaft was held at a reference value (optimal rotation speed). However, in common practice, rotation speed is never held at a reference value; hence the centrifugal force will change as the rotation speed changes. As a result, the constant quadratic stiffness k_2 can no longer compensate the centrifugal force properly, resulting in decrease in power. To identify the working range of the harvester, we performed simulation to calculate generated power of the harvester at various rotation speeds. The threshold of working range was defined by using the -3dB criteria (i.e., 0.707*peak power). Figure 5.7 shows generated power of the harvester at $\pm$30% of the

optimal rotation speed. As seen in Fig. 5.7, the power decreases as the rotation speed moves away from the optimal rotation speed, indicating the effect of k_2 is weaken. With the -3dB criteria, the working range is identified as $\pm$10% of the optimal rotation speed.

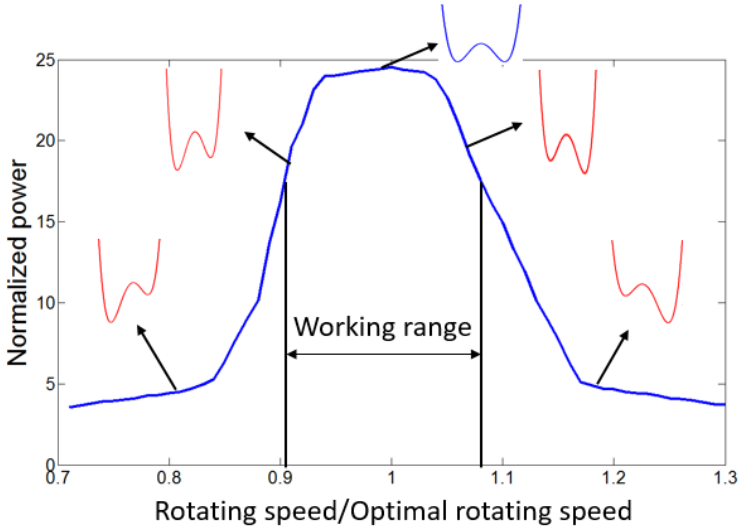

Figure 5.7 The working range of the harvester with respect to various rotation speeds. Selective potential energies of the harvester are plotted for reference.

5.4 Magnetic-enhanced stochastic resonance energy harvesting strategy

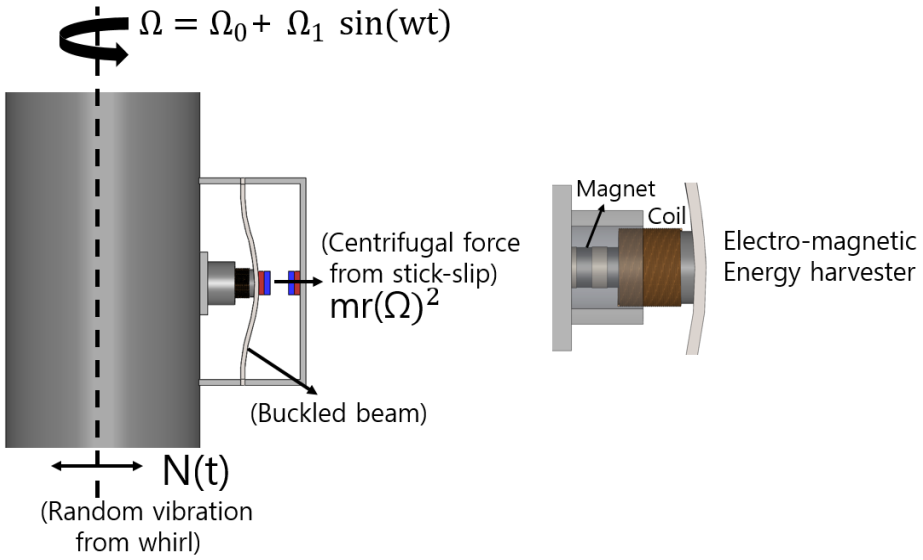

Figure 5.8 Stochastic resonance energy harvesting concept for rotating shaft. Note that the harvester is not drawn in proportion.

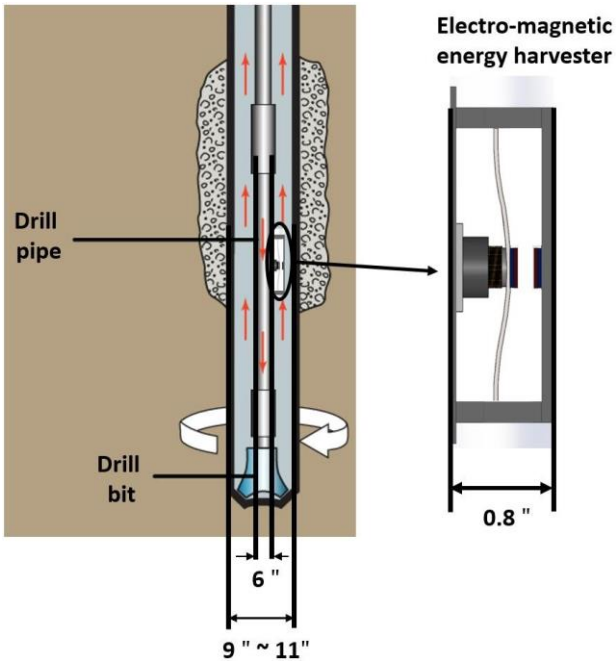

Figure 5.9 Comparison of dimension in the deep-down hole.

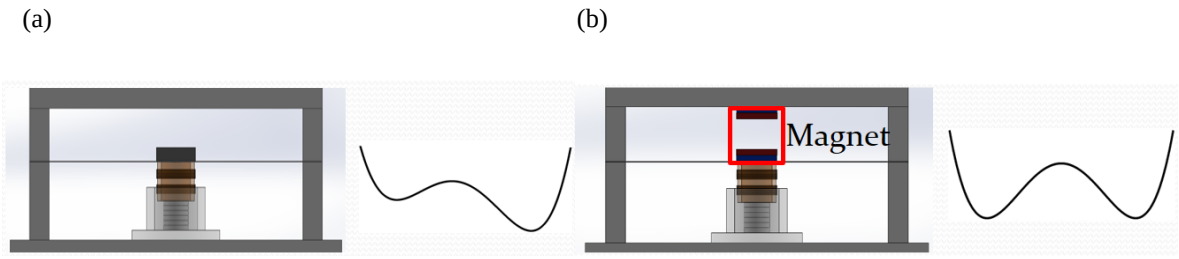

Figure 5.10 Experiment configuration of symmetric and asymmetric potential. (a) Asymmetric potential due to centrifugal force. (b) Symmetric potential resumed by magnetic force.

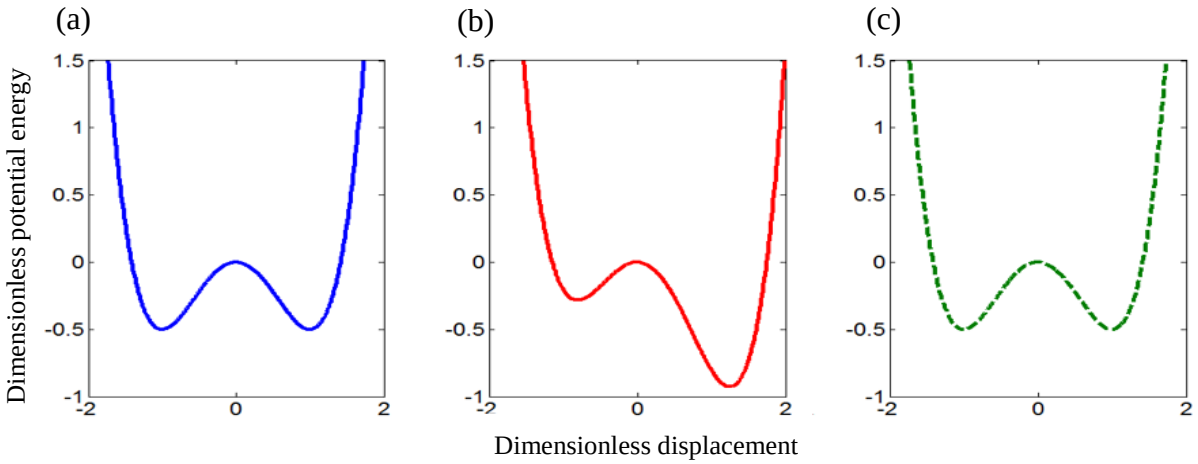

Figure 5.11 Potential energy curves for different rotating speed. (a) shaft at the rest $\Omega = 0$, (b) shaft is rotating $\Omega > 0$, (c) magnet is added.

In this section, we propose a novel energy harvesting strategy that particularly suits rotating shafts, which not only takes advantage of stochastic resonance, but also compensates the constant offset in the periodic vibration by using magnetic force. As shown in Fig. 5.8, the harvester is attached on a rotating shaft. It consists of a post buckled beam, a metal cylinder wound with copper coil installed to the mid-span of the beam, a magnet fixed to the side wall of a rotating shaft, and a pair of magnets fixed to the top of the harvester frame and to the mid-span of the beam respectively.

Note that Fig. 5.8 is not drawn in proportion. Real size of the harvester is relatively small compared to the shaft. The length of the harvester is 1m. Typical oil drill pipe weighs about 10 kg/m (6.65lb/ft) while our harvester weighs about 0.09 kg. Considering the section of the shaft in effect, the shaft can be modeled as a rotating disk and the harvester can be as a point mass. It follows that the rotating inertia of the shaft section is about 0.0288 kg$\cdot m^2$ while that of the harvester is about 0.00038 kg$\cdot m^2$; hence the rotating inertia of the harvester is 1.3% of the drill pipe, which means that the harvester contributes little to the dynamics of the rotating shaft.

Figure 5.9 shows the dimension comparison of drill hole diameter, pipe diameter and height of proposed energy harvester. The most critical design parameter for proposed energy harvester is height. This is because the gap between the wall of the drill hole and pipe is limited. For usual cases, the gap is (9-6)/2 and the maximum magnitude of lateral vibration is 0.5 [68]. Therefore, the height of the harvester should be smaller than 1. As presented in figure 5.9, the height of harvester is 0.8 which is much smaller than the design constraint (The safety factor of 1.25).

To emulate the real-world applications, the shaft is simultaneously subject to a random whirl vibration $N(t)$ and a periodic stick-slip torsional vibration of $\Omega = \Omega_0 + \Omega_1 \sin \mathrm{w}t$, where Ω_0 is a constant rotation speed (offset) and $\Omega_1 \sin \mathrm{w}t$ is a sinusoidal fluctuation to approximate the torsional vibration at a fluctuation frequency w. As a result, the centrifugal force $mr\Omega^2$ will excite the harvester, where m is the mass of the coil and r is the effective radius from the harvester to the shaft axis. The post-buckled beam creates the double-well potential necessary for stochastic resonance. When excited by the whirl (random noise) and stick-slip vibration (periodic signal), the beam will undergo large oscillation due to stochastic resonance. Consequently, the attached coil will rapidly pass though the side wall magnet, generating electricity due to electromagnetic transduction.

As illustrated in Fig. 5.8, the periodic excitation (centrifugal force) for a rotating shaft is offset by a constant value. To resolve the issue, an external force is needed to compensate the offset. In this paper, we employ a pair of magnets to compensate the constant offset; see Fig. 5.10. Figure 5.11 shows the potential energy curves of the bi-stable beam with and without the magnet. As seen in Fig. 5.11, the potential well of the harvester is originally symmetric (blue solid line) when the shaft is at rest ($\Omega = 0$). When the rotational speed $\Omega = \Omega_0$, it becomes asymmetric (red solid line). Finally, with the appropriate external magnetic force, it becomes symmetric again (green dashed line). Note that the magnetic force

was not explicitly modeled. Instead, it was included in the total nonlinear restoring force ($-k_1$ x + $k_2x^2 + k_3 x^3$) which is the sum of magnetic force and the nonlinear restoring force of the buckled beam. This nonlinear restoring force includes quadratic term [70-71] to compensate potential asymmetry due to centrifugal force. Special attention has to be given that the constant offset due to centrifugal force is implemented as constant acceleration in the following experiment section due to limitation of our current equipment. In the next section, we will demonstrate that when compared with the case without compensating magnetics, the use of a pair of compensating magnetics indeed increases power generation when the centrifugal force consists of a constant offset.

5.5 Experimental verification

In this section, we will conduct experiments to verify the numerical analysis in Section 3 using the energy harvester proposed in Section 5.4. Figure. 5.12 shows the experiment setup. A bi-stable buckled beam is installed on a shaker. The beam dimension is 150mm(L)× 25mm(W) × 0.4mm(T). An electromagnetic transducer is used to generate electricity. Furthermore, a pair of magnets are added to the top of the frame and to the mid-span of the beam respectively to compensate the offset of the centrifugal force. A SENTEK dynamics (VT-1000) is used to drive the harvester. In this experimental study, we excite the harvester with an equivalent random excitation and periodic force, which have the same effect as the whirl and stick-slip vibration considered in the simulation.

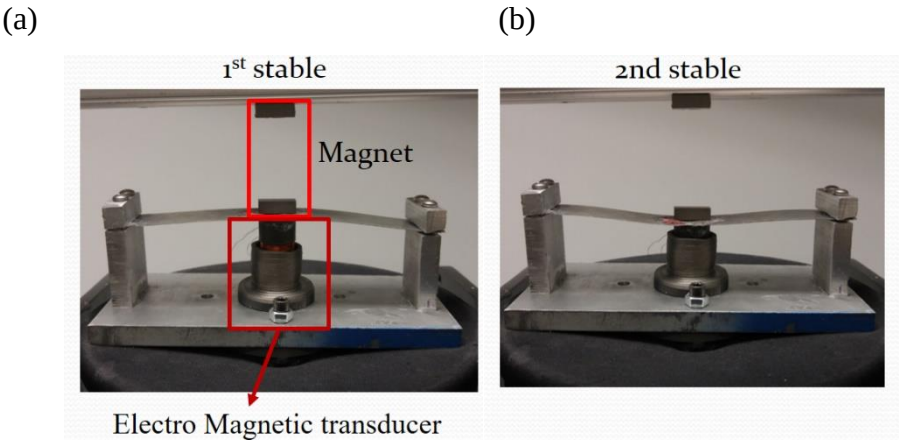

Figure 5.12 Experiment setup of stochastic resonance energy harvester with magnet: (a) 1st stable (b) 2nd stable.

Since modeling the force-displacement relation and damping coefficient is difficult, we performed a system identification to associate the simulation and experiment [70]. A force sensor (PCB208C02) is used to measure the nonlinear force of the system. In Fig. 5.12, the red circle indicates the measurement results while the blue line indicates the fitting curve. The root mean square error of curve fitting is R=0.83. Damping coefficient is determined via trial and error. Figure. 5.13 compares the amplitude spectrum of simulation with system identification and actual experiment. A 13% error is observed in terms of the peak value of stochastic resonance, showing that the system identification renders satisfactory results.

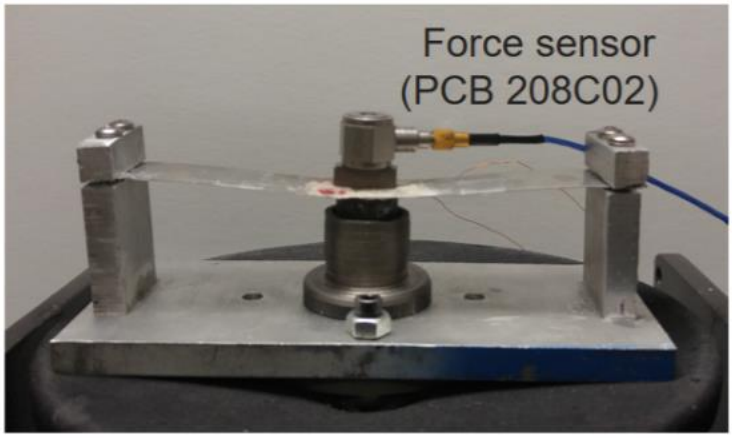

Figure 5.13 Experiment setup to measure force-displacement curve.

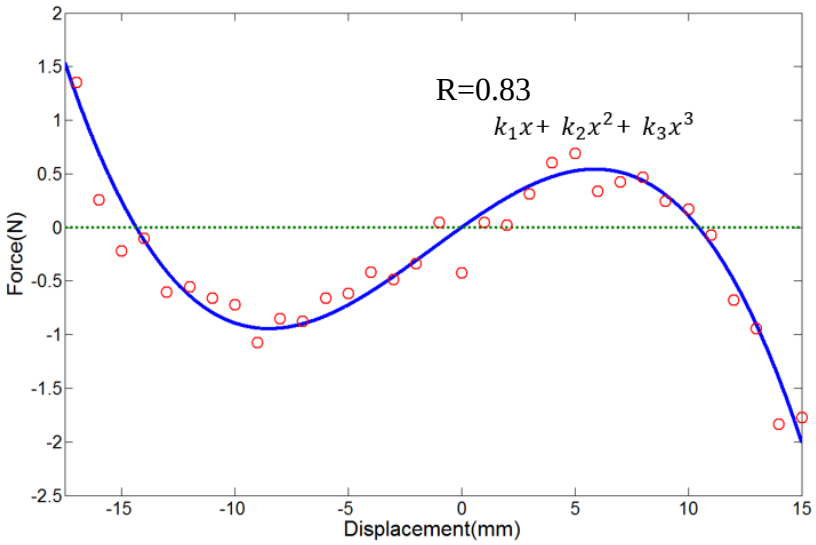

Figure 5.14 Nonlinear restoring force-displacement fitting curve.

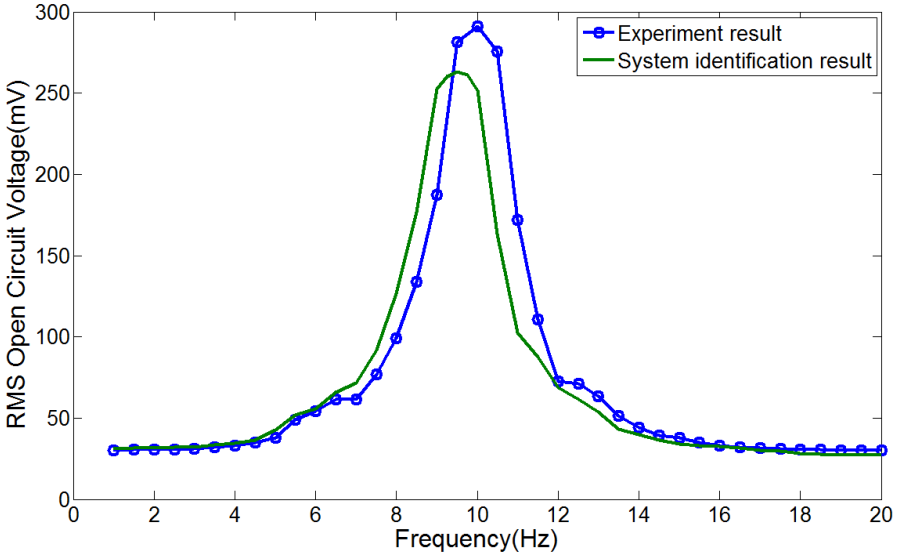

Figure 5.15 Comparison of the amplitude spectrum between simulation with system identification and experiment.

White noise (intensity D=0.13) and a weak periodic signal with offset 0.08g and magnitude 0.06g were input to the shaker. The periodic signal was varying from 0 to 20 Hz while the offset was kept constant. The magnitude of the input was determined from real oil drilling data

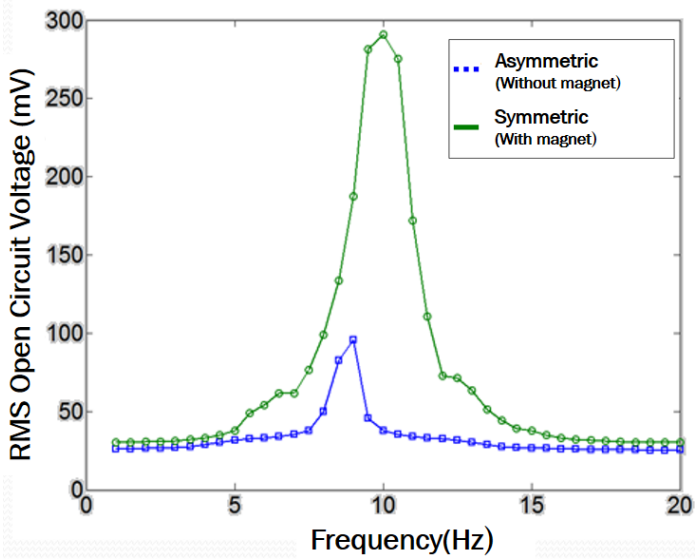

Figure 5.16 Comparison of amplitude spectrum in the asymmetric potential energy harvester (without magnet) and the symmetric potential energy harvester (with magnet).

(Schlumberger.Ltd). All the values were scaled down to 5:1 because the real size of the harvester (to be applied to an oil drilling string) is about five times larger than the experiment setup.

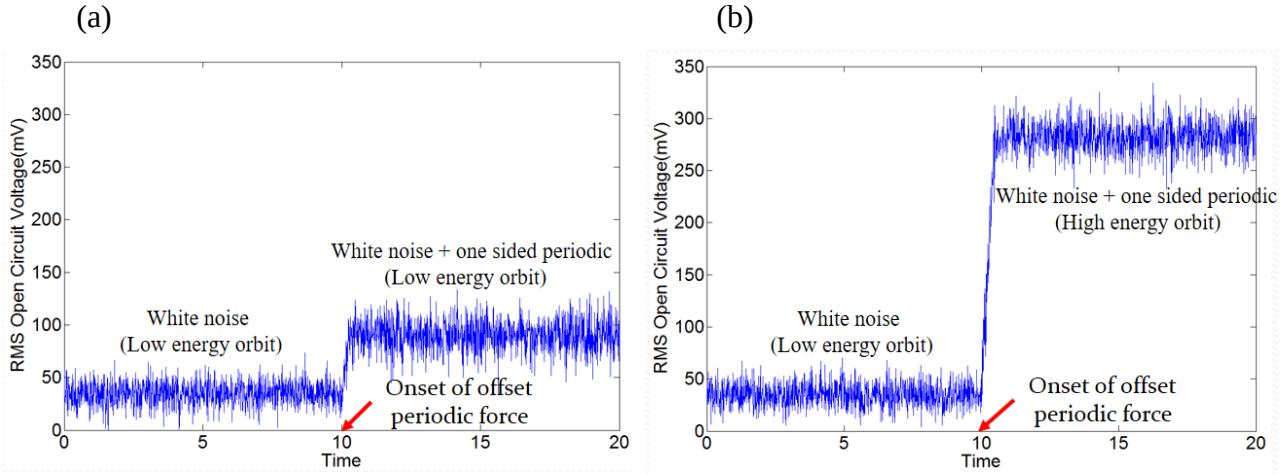

Figure 5.17 Time response of the experiment setup: (a) without compensating magnets (asymmetric potential) (b) with compensating magnets (symmetric potential).

Figure. 5.17 compares the asymmetric potential harvester (without compensating magnets) and the symmetric potential harvester (with compensating magnets) in the amplitude spectrum. Peak voltage was 287 mV at 9.8 Hz for the symmetric potential harvester while 93 mV at 9.2 Hz for the asymmetric potential harvester. The trend of experiment result coincides with numerical results obtained earlier. Figure. 18 shows the time response. In the first 10 seconds, the harvester was excited only by the white noise. A periodic force with constant offset was added at 10 seconds. It is clear that for the symmetric potential case, the oscillation of the harvester jumps from the low energy branch into the high energy branch with the assistance of periodic signal.

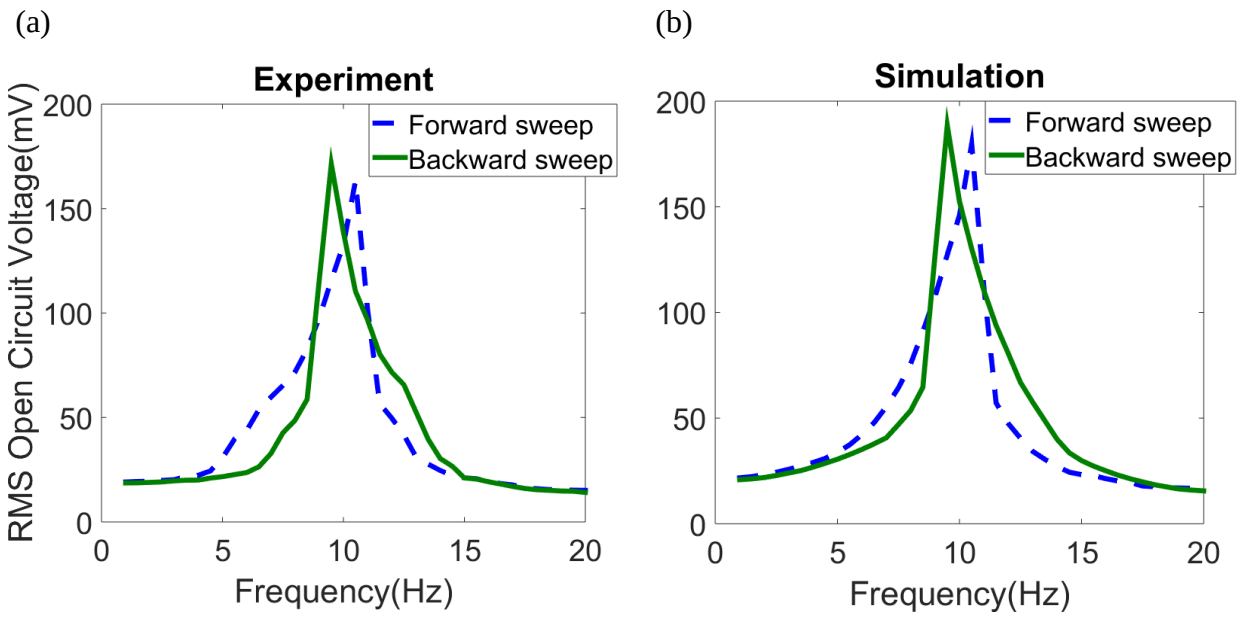

Figure 5.18 Frequency sweep test result: (a) Experiment (b) Simulation.

A frequency-swept test was conducted to investigate the influences of frequency-sweep on stochastic resonance. Sweep signal at a rate of 0.5 Hz/s is performed. The sweep frequency response of the harvester is shown in Fig. 5.18. As shown in Fig. 5.18, there are some difference between up-sweep and down-sweep. In the case of up-sweep, the peak is shifted a little to right and a jump phenomenon (a phenomenon suddenly entering the lower branch from the higher branch) occurs in the higher frequency band. In the down-sweep case, the peak is shifted to the left and the jump phenomenon happens in the lower frequency band. Therefore, the hysteretic effect is observed in the presented energy harvester. Also, stochastic resonance occurs for both up-sweep and down-sweep cases. The experiment results show the similar trend as the numerical simulation although there is a little error (10% in peak values) between them.

5.6 Chapter summary

In this chapter, we investigated the use of stochastic resonance to extract vibration energy from a rotating shaft. Two types of shaft vibrations were considered, random whirl vibration and periodic stick-slip vibration. Our analysis showed that stick-slip vibrations impose a constant offset in the centrifugal force and distorts the potential function of a bi-stable harvester, leading to potential function asymmetry. To investigate stochastic resonance with potential asymmetry, we conducted a numerical analysis where we solved the FPK equation of the bi-stable harvester. Numerical results of the harvester with symmetric and asymmetric potential were compared. The former showed nearly seven times higher power output than the latter. Also, effects of rotation speed were studied. With the -3dB criteria, the working range of the harvester was identified as $\pm 10\%$ of the optimal speed. An electromagnetic energy harvesting system was constructed to experimentally verify the numerical analysis. On contrary to traditional stochastic resonance harvesters, the proposed harvester uses magnetic force to compensate the offset in the centrifugal force. System identification was performed to obtain the parameters needed in the numerical analysis. With the identified parameters, the numerical simulations showed good agreement with the experiment results around 10% of errors, which verified the simulation results. Peak voltage was found to be 287 mV at 9.8 Hz for the symmetric potential case while only 93 mV at 9.2 Hz for the asymmetric potential case. Furthermore, stochastic resonance was observed to have hysteretic behavior in a frequency-sweep analysis, rendering frequency difference between up-sweep and down-sweep excitations. Both numerical and experimental investigation verified the advantage of the presented energy harvesting strategy which can be applied to various rotating shaft system such as oil drilling.

6. Self-tuning stochastic resonance energy harvesting for smart tire

6.1 Chapter introduction

In this chapter, we propose an energy harvester for rotating systems under modulated noise excitations by taking advantage of self-tuning stochastic resonance with particular application to power smart tire. It is an electromagnetic energy harvester consisting of an inward oriented rotating beam subjected to centrifugal force induced buckling. The compressive centrifugal force induces bistability to the harvester. The equation of motion is derived to investigate the effect of self-tuning. The tuning performance is verified by analysis of Kramers rate and signal-to-noise ratio (SNR). Numerical simulation is conducted to simulate the harvested power in a passenger car tire at different driving speeds. A rotating platform is built to mimic the tire rotation.

6.2 Self-tuning stochastic resonance induced via a centirifugal stiffening effect

Traditional stochastic resonance harvesters are only efficacious when the driving frequency is near to the stochastic resonance frequency. To overcome this critical drawback, we propose a self-tuning stochastic resonance harvester that passively tunes its stochastic resonance frequency with the driving speed. The design is shown in Fig. 6.1. The harvester consists of two parts, a frame and a cantilever beam with a tip mass. One end of the frame is attached to the tire rim while the other end (distal end with respect to the tire center) is free. The root of the cantilever beam is fixed to the free end of the frame while the tip mass is pointing at the center of the tire, i.e., the beam is inward oriented, which allows the beam to be buckled by the centrifugal force when the rotation speed reaches a threshold, resulting in a bistable buckled beam induced by the centrifugal force. Furthermore, an electromagnetic transducer is used to have a high-power density, which consists of the lower part of the frame made of ferromagnetic material, two permanent magnets attached inside the lower part of the frame and the tip mass made of

ferromagnetic material around which copper coils are wound to generate magnetic flux, as shown in Fig. 3(a). As the beam oscillates, the coils continuously cross the magnetic flux, generating electricity. The inductance L of the electromagnetic harvester is ignored because the impedance of inductance is much smaller than that of resistance (L $w_{max} = 128.27\ \Omega \gg$ R $= R_L + R_{internal} = 1000 + 951.24 = 1951.24\Omega$); thus, the electromagnetic effect is simplified and represented by the electrical damping coefficient as following [69].

$$c_e = \frac{K^2}{R_L + R_{internal}} \tag{6.1}$$

where R_L is external load resistance, $R_{internal}$ is internal resistance of coil, K is electromechanical coupling constant

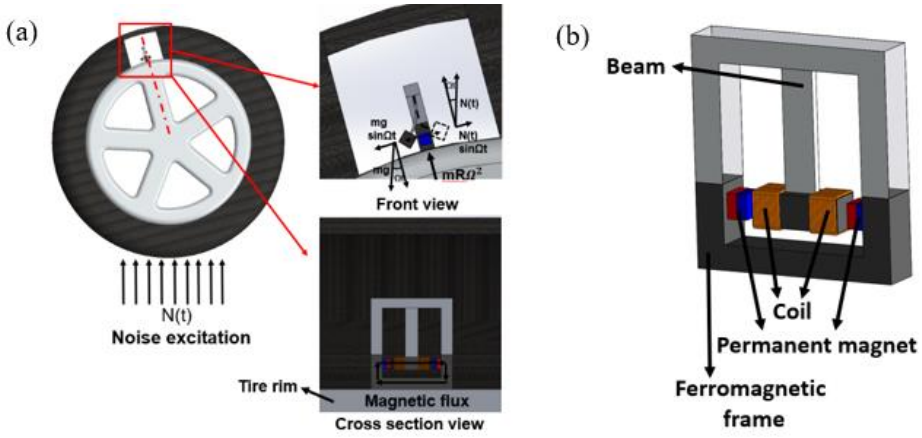

Figure 6.1 Self-tuning stochastic resonance energy harvester for rotating tires: (a) installation of the harvester in a tire and(b) the design of the harvester.

To have a high-power density, the magnetic flux of the electromagnetic transducer is simulated using FEMM (Finite Element Method Magnetic) software; see Fig. 6.2. The design parameters of the transducer are shown in Fig. 4(a) and the magnetic flux simulation is shown in Fig. 6.2 (b). Maximization of the magnetic flux yields the following results: Distance between the ferromagnetic tip mass and frame d_1: 10 mm; Distance between the magnets and coil d_2: 3 mm and length of the coil d_3: 7mm. It turns

out that the most critical parameter is the distance between magnet and coil d_2. Due to limitations in manufacturing, $d_2 = 5$ mm is used throughout the rest of the paper although the optimal value is 3 mm.

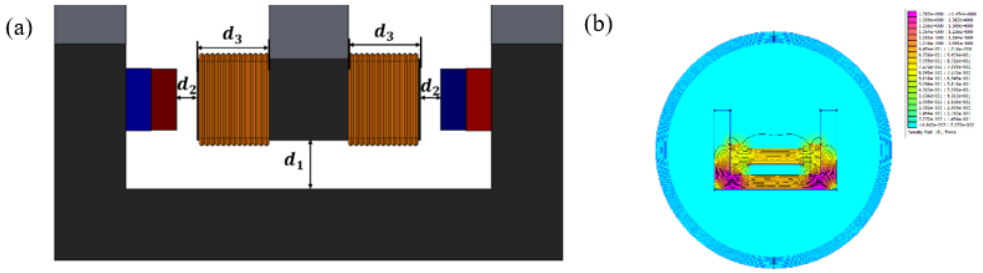

Figure 6.2 Magnetic flux simulation performed by FEMM: (a) geometric parameters considered and (b) simulation results.

Figure 6.3 shows a schematic diagram of the harvester when used in a rotating tire. There are two things worth noting in Fig. 6.3. First, the harvester is subjected to excitations in the circumferential direction generated by the ground noise $\mathrm{N}(t)$ and gravitational acceleration g. As the harvester rotates along with the tire, the amplitude of the noise and gravity excitation in the circumferential direction is modulated by the angular position of the tire; thus the beam is excited by amplitude-modulated excitations, $\mathrm{N}(t)\sin(\Omega t)$ and $g\sin(\Omega t)$, as shown in Fig. 5(a). Furthermore, the excitation frequency Ω is equal to the driving speed. As a result, the noise and gravity excitation are also frequency-modulated when the driving speed changes, which is very different from the scenario of traditional stochastic resonance harvesters (cf. Eq. (1)). Second, due to the inward orientation, the beam will be buckled by the centrifugal force when the rotating speed reaches a threshold, resulting in a bistable system of two stable equilibria, $S1$ and $S2$. The positions of $S1$ and $S2$ (thus the potential well function) will change with the rotating speed; thus, the stochastic resonance frequency will change accordingly as it is a function of the potential well function; see Eq. (3). Note that the noise intensity $D(\Omega) = D_0 + D_1\Omega$, where D_0 and D_1 are constant, is assumed to increase linearly with the driving speed, which corresponds to the measurements obtained from real vehicles [33].

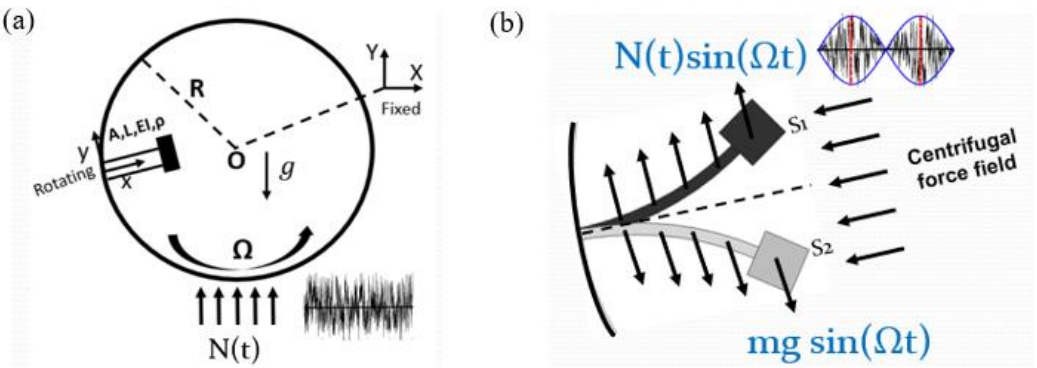

Figure 6.3 Schematic diagram of inward oriented rotating beam energy harvester: (a) Whole system. (b) Freebody diagram of beam.

To derive the equation of motion of the harvester, the procedure of Turhan and Bulut [31] is used. After including the inertial forces of the tip mass and the noise and gravity excitation along the beam, the equation of motion of the proposed harvester is approximated by the 1st vibration mode of the cantilever beam with tip mass as

$$q'' + 2\zeta\lambda q' + k_1(\beta^2)q + k_3(\beta^2)q^3 = K\varepsilon \sin\beta\tau + K\varepsilon n(\tau)\sin\beta\tau \qquad (6.2)$$

where q is the generalized coordinate of the 1st mode, λ is the eigenvalue of the mode, $\zeta = \frac{c_m + c_e}{2\sqrt{mk_1}}$ is the damping ratio, $\alpha = R/L$ is the ratio between the radius R of rotation (rim radius plus harvester frame height) and beam length L, $\beta = \Omega/\omega_0$ is the dimensionless rotation speed normalized by $\omega_0 = \sqrt{\frac{EI}{\rho AL^4}}$, where E is the Young's modulus, I is the moment of inertia, ρ is the density, and A is the cross sectional area of the beam, $\varepsilon = g/L\Omega^2$ is the dimensionless gravity excitation where gravitational acceleration g is normalized by the centrifugal acceleration $L\Omega^2$ at the beam tip, $n(\tau) = N(\tau)/g$ is the dimensionless noise excitation where the original noise excitation is normalized by the gravity excitation, and $\tau = t/\omega_0$ is the dimensionless time, prime(s) denote derivative(s) with respect to τ and K is a modal force constant. Note that ε represents a weak excitation as the centrifugal acceleration at the beam tip is typically more a hundred times larger than gravitational acceleration in a rotating tire. Also, modal noise intensity in

the 1st mode can be defined as $d = (\frac{K\varepsilon}{g})^2 D$, which is derived via $K\varepsilon n(\tau) = \frac{K\varepsilon N(\tau)}{g} = \frac{K\varepsilon\sqrt{2D}}{g}\xi(\tau)$ $= \sqrt{2\left(\frac{K\varepsilon}{g}\right)^2 D}\xi(\tau) = \sqrt{2d}\xi(\tau)$.

Furthermore,

$$\begin{cases} k_1(\beta^2) = \lambda^4 - \beta^2 T_l \\ k_3(\beta^2) = C - \beta^2 T_{nl} \end{cases} \tag{6.3}$$

are the self-tuning linear and cubic stiffness of the harvester, where λ^4 and C are the modal linear and cubic stiffness, which are tuned by T_l and T_{nl}, the tuning factors due to the centrifugal acceleration. The reader is referred to Appendix A.1-2 for details of the derivation.

As seen in Fig. 6.4(b), under the influence of the centrifugal field, the beam is buckled when the rotation speed reaches a threshold, which occurs when the modal linear stiffness is negated by the centrifugal acceleration, i.e., when $\lambda^4 - \beta^2 T_l = 0$. Thus, the critical buckling speed (Critical speed 1) is

$$\Omega^{cr1} = \omega_0\sqrt{\frac{\lambda^4}{T_l}} \tag{6.4}$$

When the rotating speed exceeds the critical buckling speed, two stable equilibria can be represented as function of rotating speed [80] as follows

$$y_{equilibrium} = \pm\varphi\sqrt{\frac{-(\lambda^4 - \beta^2 T_l)}{C - \beta^2 T_{nl}}} \tag{6.5}$$

Fig 6.6 (a) graphically shows the relation between the two stable equilibria and rotating speed using Eq (6.7). Furthermore, the natural frequency of the 1st mode around a given equilibrium can be represented as

$$f = \frac{w_0}{2\pi}\sqrt{|\lambda^4 - T_l\beta^2|} \tag{6.6}$$

Fig 6.4 (b) shows the natural frequency of the current system using Eq (6.5). Furthermore, the natural frequency at selected rotational speeds was also measured experimentally (Open circuit and no base

excitation) and plotted with circle markers in Fig. 6.4(b). As shown, the measurements follow the trend of the theoretical prediction well, indicating that the system is indeed bistable after the critical rotation speed.

If rotating speed β reaches another threshold, which occurs when the modal non-linear stiffness is negated by the centrifugal acceleration, i.e., when $C - \beta^2 T_{nl}$. Thus, the critical buckling speed (Critical speed 2) is

$$\Omega^{cr2} = \omega_0 \sqrt{\frac{C}{T_{nl}}} \tag{6.7}$$

When the rotating speed exceeds the critical speed 2, there is no restoring force exists equation in (6.2). This means that the system does not exhibit vibratory motion anymore.

(a)

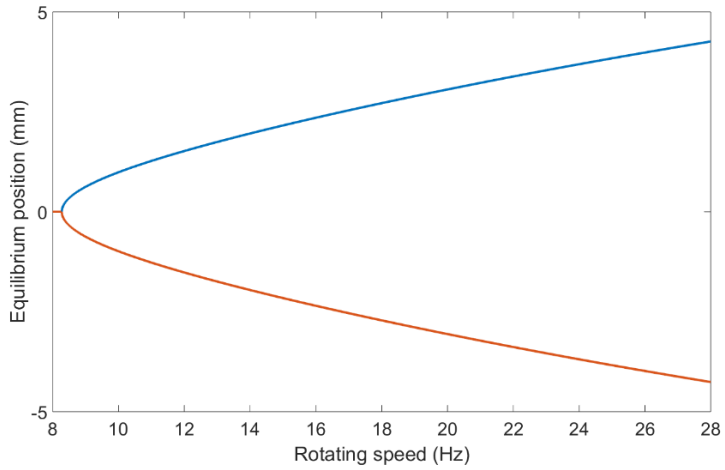

(b)

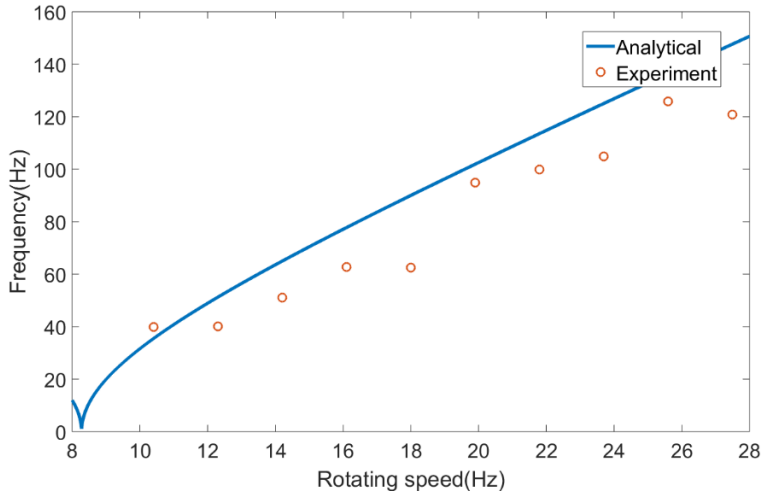

Figure 6.4 Bistability of self-tuning harvester: (a) Equilibrium position vs rotating speed (b) Natural frequency vs rotating speed.

6.3 Stochastic resonance for modulate noise

When the noise excitation has constant intensity, the stochastic resonance frequency of the harvester can be determined by the Kramers rate in Eq. (6.3). After substituting $k_1 = \lambda^4 - \beta^2 T_l$ and $k_3 = C - \beta^2 T_{nl}$ from Eq. (6.3) into Eq. (2.6), one obtains the self-tuning stochastic resonance frequency

$$f_{SR} = \frac{\sqrt{2}|\lambda^4 - \beta^2 T_l|}{8\pi\zeta}\omega_0 e^{\left(-\frac{(\lambda^4 - \beta^2 T_l)^2}{4(C-\beta^2 T_{nl})d(\beta)}\right)} \tag{6.8}$$

As seen in Eq. (6.8), the self-tuning stochastic resonance frequency of the harvester is a function of the dimensionless driving speed β. By properly choosing the beam parameters, the beam can tune its stochastic resonance frequency according to the driving speed. Note that Eq. (6.8) are only valid when the noise intensity is constant.

For rotating tires, the noise intensity is amplitude-modulated; see Fig. 6.3(b). For some cases, using average noise intensity over one period ($D_{avg} = \int_0^T sin\,\beta\, dt$) for equation (6.8) provides decent approximation. Most of the cases, however, it is not. To investigate how noise modulation influences stochastic resonance, the signal-to-noise ratio (SNR) of Eq. (6.4) is derived using the two-state method [87]. Details of the derivation are provided in Appendix A.3. Equation (6.9) shows the SNR.

$$\text{SNR}(\beta,\beta^*) = \frac{s_s(\beta)}{s_n(\omega=\beta,\beta)} = \frac{2\sqrt{2}k_1^3(K\varepsilon)^2}{\beta D^2 k_3} e^{-\frac{k_1^2}{3D\beta k_3}}\left[1-\frac{\frac{3k_1^3(K\varepsilon)^2}{10\pi^2\beta D^2 k_3}e^{-\frac{5k_1^2}{6D\beta k_3}}}{\frac{2k_1^2}{\pi^2}e^{-\frac{5k_1^2}{6D\beta k_3}}+\beta^2}\right]^{-1} \tag{6.9}$$

where $k_1((\beta^*)^2)$ and $k_3((\beta^*)^2)$ are the linear and cubic stiffness coefficients defined in Eq. (6.3) and β^* is a dummy variable which is introduced for the purpose of demonstration. Note that β^* is not shown in Eq. (6.9) for the sake of simplicity. In this way, if $\beta^* = \beta$, Eq. (6.9) presents SNR of the proposed self-tuning harvester (referred to as self-tuning harvester hereafter). On the other hand, if β^* corresponds to a specific driving speed, Eq. (6.9) represents SNR of a traditional stochastic resonance harvester without self-tuning (referred to as traditional harvester hereafter) with constant linear and cubic stiffness coefficients equaling $k_1((\beta^*)^2)$ and $k_3((\beta^*)^2)$ under modulated noise excitations. By taking derivative

SNR over β^* and set it to zero ($\frac{d(SNR)}{\beta^*} = 0$), stochastic resonance frequency f_{sr} can be calculated as Equation (3). This means at β^*=$2\pi f_{sr}$ the SNR is maximal.

The example harvester of Table 6.1 is used for demonstration, whose SNR(β, β) is computed by substituting the parameters in Table 6.1 into Eq. (6.9) and plotted in solid line in Fig. 6.5 Furthermore, SNR(β, β_i^*) of three traditional harvesters each of which has constant linear and cubic stiffness coefficients $k_1((\beta_i^*)^2)$ and $k_3((\beta_i^*)^2)$, where β_i^* denotes a specific driving speed and $i = 1,2,3$, are also plotted in dashed and dotted lines. There are several things worth noting in Fig. 6. First, the peaks of SNR(β, β_i^*) correspond to stochastic resonance of the traditional harvesters. In this regard, the rotation speed β_i^{max} that corresponds to the peak, i.e., SNR(β_i^{max}, β_i^*)=max(SNR(β, β_i^*)) and max(·) denotes the maximum operator, is considered as the stochastic resonance frequency at a specific rotation speed β_i^*; in other words, one can define the stochastic resonance frequency as $f_{SR}(\beta_i^*) = \beta_i^{max}$. Second, since SNR($\beta, \beta$) of the self-tuning harvester is computed by continuously tuning linear and cubic stiffness coefficients, the solid curve can be obtained by connecting SNR(β^*, β^*) of the traditional harvesters within a range of β^* of interest. As such, if SNR(β, β^*) intersects with SNR(β, β) at its peak, the self-tuning harvester is within the self-tuning region wherein the harvester achieve the maximum attainable power at a specific rotating speeds. SNR(β, β_1^*) and SNR(β, β_2^*) (dashed curves) are two examples of such cases. As seen, the peaks of the dashed curves coincide with the solid curve, indicating that the self-tuning harvester is perfectly tuned to achieve stochastic resonance at these two driving speeds (β_1^* and β_2^*). On the other hand, if SNR(β, β^*) does not intersect at the peak, the self-tuning harvester leaves the self-tuning region and is considered as "off-tuned". SNR(β, β_3^*) (dotted curve) is one example of such cases. As seen, the peak of the dotted curve deviates from the solid curve, indicating that the harvester is off tuned at this specific driving speed (β_3^*).

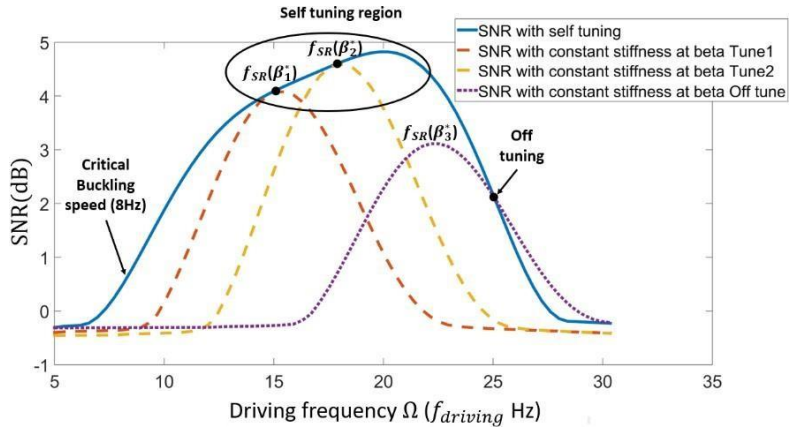

Figure 6.5 SNR versus rotation speed Ω to investigate effect of self-tuning.

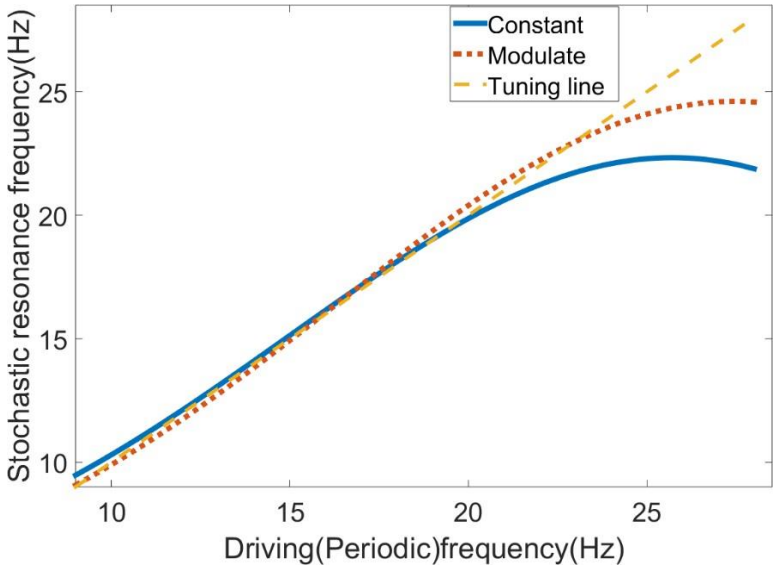

Figure 6.6 Stochastic resonance frequency versus driving frequency for modulated noise and non modulated noise.

Figure 6.6 compare stochastic resonance frequency versus driving frequency for modulated and non-modulate case. For the non-modulated case, it is calculated based on equation (6.8). For the modulated case, it is derived by taking derivative on equation (6.9) over frequency and find maximum value of that.

As shown, in both cases the harvester tracks the time varying driving frequency of the tire until a certain frequency after which f_{SR} deviates from the driving frequency more than 5%. This certain frequency is defined as 'off-tuning frequency'. This means that stochastic resonance occurs regardless of the driving speed (which corresponds to the driving frequency) change until it reaches to the off-tuning frequency. Therefore, optimal power generation can be achieved over a wide range of vehicle speeds. As the driving frequency is increased over the threshold, however, off-tuning starts as seen from fig 6.6. This leads to sharp decline of stochastic resonance frequency and the harvester cannot track the driving frequency any more. Thus, it is important to choose parameters to delay detuning as much as possible.

Table 6.1 Parameters of example harvester 1.

Beam dimension	$64.5 \times 8 \times$
Tip mass	$20 \times 20 \times$
Tip mass weight	7.8 g
Young's modulus	70 GPa
Density	2.7 g/cm^3
Rotating radius	203 mm
Damping ratio	0.25

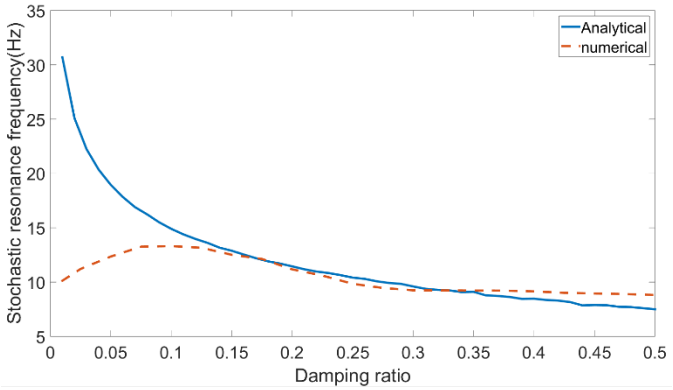

Figure 6.7 Comparison of stochastic resonance frequency determined by analytical SNR and numerical SNR.

Finally, to validate Eq. (6.9), a numerical scheme (see details in Sec. 3) is developed to solve Eq. (6.9) to determine the stochastic resonance frequency numerically. Figure 6.7 compares the numerically and analytically determined stochastic resonance frequencies at different damping ratios. Since the SNR formula uses the Kramers rate that assumes moderate damping (see Eq. (6.8)), the numerical and analytical results agree well with each other in the moderate damping region (0.2~0.5) while mismatch occurs at the lower damping region (<0.1).

6.4 Numerical simulation of smart tire energy harvester

In this section, numerical simulation is conducted to examine how much power the proposed harvester generates in a rotating tire. A P 215/60/R16 tire is chosen which has a diameter of 66.55 cm (26.2"), a section width of 21.59 cm (8.5"), a sidewall height of 12.95 cm (5.1") and a wheel diameter of 40.64 cm (16"). Two harvester designs which are estimated to generate at least 30 mW power in the tire are provided whose parameters are listed in Table 2. One design has a longer beam length and smaller tip mass than the other.

Table 6.2. Parameters of energy harvester using in simulation.

	Harvester1	Harvester2
Beam dimension (L × W ×	90 × 20 ×	64.5 ×
Tip mass dimension (W×	35 × 20 ×	35 × 20 ×
Tip mass weight	25 g	40 g
Young's modulus	70 GPa	
Density (Aluminum)	2.7 g/cm^3	
Mechanical damping ratio	0.055	
Mechanical damping ratio	0.201	
Car tire type	P 215/60/R16	

The numerical scheme proposed by He et al. [83] is used to calculate the power of the harvesters, where Eq. (6.2) is transformed into the Fokker Plank Kolomov equation (FPK), governing the probability density function of the modal displacement q and velocity $\dot{q}$. The procedure is briefly explained as follows. First, Eq. (6.2) is arranged into the Ito form as,

$$dq_1 = q_2 dt$$

$$dq_2 = \{-2\zeta\lambda q_2 - (\lambda^4 - \beta^2 T_l) q_1 + (C - \beta^2 T_{nl}) {q_1}^3 + K\varepsilon \sin\beta\tau\} d\tau + K\varepsilon \sin\beta\tau \, dW, \quad (6.10)$$

where $q_1 = q$ and $q_2 = \dot{q}$. Next, the FPK equation can be derived from the above Ito form as [84],

$$\frac{\partial P}{\partial t} = -q_2 \frac{\partial P}{\partial q_1} + 2\zeta\lambda \frac{\partial (q_2 P)}{\partial q_2} + (-(\lambda^4 - \beta^2 T_l) q_1 + (C - \beta^2 T_{nl}) {q_1}^3 - K\varepsilon \sin\beta\tau) \frac{\partial P}{\partial q_2} + K\varepsilon \sin\beta\tau \frac{\partial^2 P}{\partial {q_2}^2} \quad (6.11)$$

where $P(q_1, q_2)$ is the probability density function.

Discretizing Eq. (6.11) by the finite element method proposed by He at al. [94] yields a set of ordinary differential equation

$$\mathbf{M}\dot{\mathbf{p}} + \mathbf{K}\mathbf{p} = \mathbf{A}\mathbf{q}\sin\beta\tau, \quad (6.12)$$

where **p** is the nodal vector consisting of the probability density at each node of the finite elements and **M, K** and **A** are matrices whose entries M_{kl}, K_{kl}, A_{kl} are defined as

$$M_{kl} = \int_A N_k N_l \, dq_1 dq_2, \; A_{kl} = \int_A \frac{\partial N_k}{\partial q_2} N_l dq_1 dq_2 ,$$

$$K_{kl} = \int_A -q_2 \frac{\partial N_k}{\partial q_1} N_l dq_1 dq_2 + \int_A (2\zeta\lambda q_2 - (\lambda^4 - \beta^2 T_l) q_1 + (C - \beta^2 T_{nl}) {q_1}^3) \frac{\partial N_k}{\partial q_2} N_l dq_1 dq_2 + K\varepsilon \int_A \frac{\partial N_k}{\partial q_2} \frac{\partial N_l}{\partial q_2} \, dq_1 dq_2 \quad (6.13)$$

where N_k, N_l are the iso-parametric shape functions, subscripts k, l are indices of the nodes and A is the area of the element. Upon solving Eq. (6.13), the average displacement and velocity (also power) can be obtained by calculating the statistical moment of the discretized probability density function **p**. For example, the dimensionless power $\bar{P}$ can be calculated according to the following equation.

$$\bar{P} = \zeta_e < {q_2}^2 > = \zeta_e \int_{-q_2 l}^{q_2 h} \int_{-q_1 l}^{q_1 h} q_2^2 P(q_1, q_2) dq_1 dq_2 \approx \zeta_e \sum_i \sum_j q_{2i}^2 p_{ij} dq_1 dq_2 \quad (6.10)$$

where h, l are upper limit and lower limit of integration boundary, q_{2i} and p_{ij} are dimensionless speed and probability density, ζ_e is the electrical damping ratio.

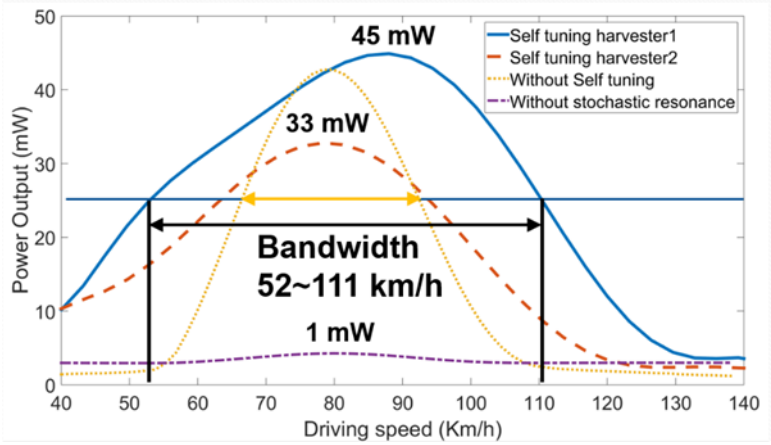

Figure 6.8. Numerical simulation of power output for real tire environment.

Figure 6.8 presents the harvested power of the proposed harvester between 40 km/h to 140 km/h. A traditional stochastic resonance harvester without the self-tuning mechanism and a linear harvester without self-tuning and stochastic resonance are considered as the baselines, whose power are also plotted in Fig. 6.8. As seen, the proposed harvester can generate significantly larger power and has a wider bandwidth compared to the baselines. Furthermore, the peak power of Harvester 1 is 45 mW, which is much larger than what was achieved in previous tire energy harvesters reported in the literature [14-20]. In addition, the bandwidth is 52~111 km/h (with half power bandwidth criteria), which is about 1.8 times larger when compared to the traditional stochastic resonance harvester. Also, simulation for Harvester 2 (smaller length and heavier tip mass) is conducted. The maximum power output is 33 mW, showing fairly large output compare to its size. In short, these simulation results show that the proposed harvester has the potential to provide sufficient power to smart tires.

6.5 Experimental verification with rotating platform

An experiment is conducted to validate the numerical simulation. A horizontal rotating platform is built to simulate the tire environment, as shown in Fig. 6.11 and Fig. 6.12. A Quansar shake table is used to provide excitation. The excitation $2(N(t)+g)\cos(\frac{\Omega}{2}t)$ is used to account for gravitational acceleration because the excitation is applied horizontally. (As described in Fig 2 (a), the original excitations were $(N(t)+g)\sin(\Omega t)$. Amplitude of noise: 0.31g~0.96g)) Although, there is inconsistency between rotating speed $(\frac{\Omega}{2})$ and excitation frequency(Ω), the basic concept of self-tuning remains unchanged. To simulate tire rotation, the rotating beam is mounted on a Marathon electric motor. The harvester is installed at the end of the rotating beam and a counter mass is also installed on the opposite side for dynamic balance. A Mooshimeter smartphone data logger is used to record the data. A 1k resistor, is used to measure the power. All the parameters and the excitations are scaled down to 1/3 compared to Harvester 1.

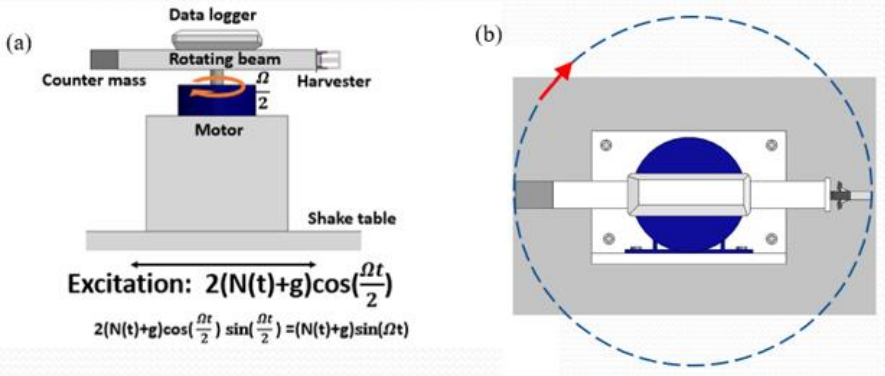

Fig 6.9 Equivalent horizontal rotating platform for tire energy harvesting: (a) front view and (b) top view.

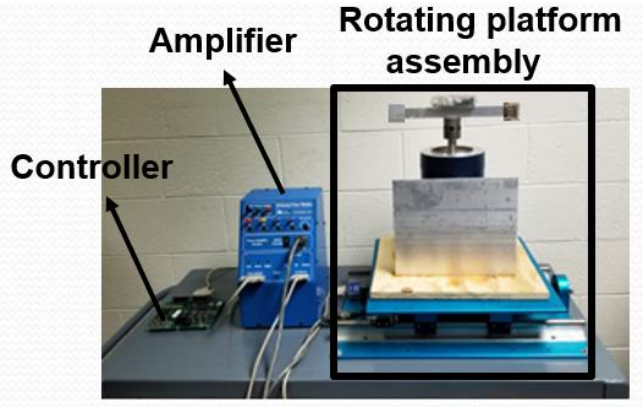

Fig 6.10 Experiment setup of stochastic resonance harvester for modulated noise.

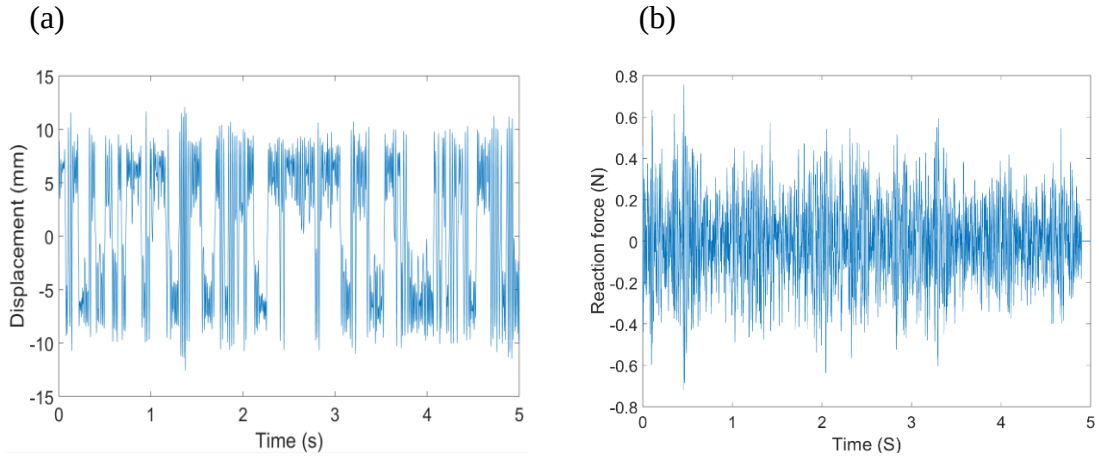

Fig 6.11. Displacement and Reaction force measurement results. (a) Displacement of tip mass at 300 rpm (b) Reaction force due to tip mass vibration.

Fig 6.11 (a) shows measured displacements of the tip mass at the rotating speed 300 rpm. The tip mass is vibrating between the two stable equilibria shown in Fig 6.6 (a). When tip mass vibrates as shown in fig 6.13 (a), rotating imbalance may occur due to reaction forces induced by tip mass vibration. To investigate whether tip mass vibration negatively change the tire balance, reaction force due to the tip mass vibration is measured. Fig 6.13 (b) shows that the vibration of tip mass does not affect tire

balance. Rms magnitude of reaction force is only 0.0088g which is much smaller compared to typical vibration of the tire.

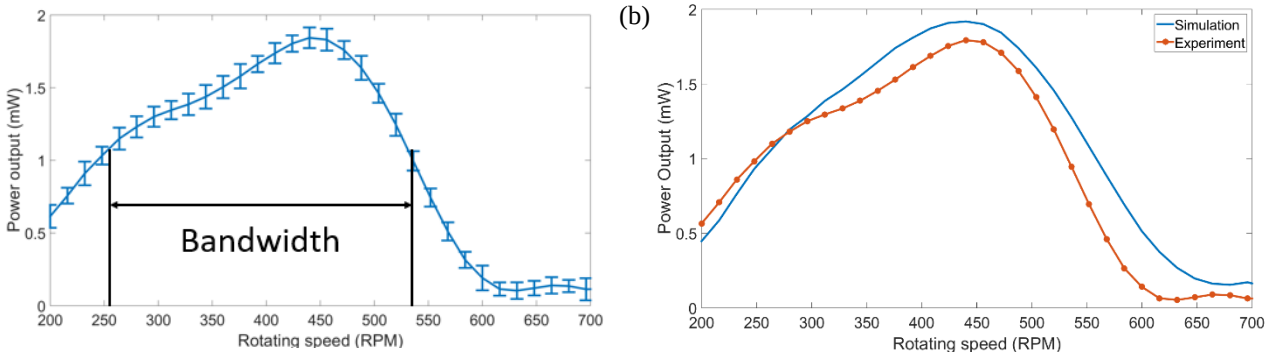

Figure 6.12. Voltage output of harvester respect to driving speed. (a) Experiment results with error bar (b) Compare with simulation results

Figure 6.12 (a) shows the power output of the harvester with error bar. The power is maximum at 445 rpm. Using the half bandwidth criterion, the bandwidth is calculated as 251 to 539 rpm. Figure 6.12 (b) presents that the trend of the experiment results coincides with numerical simulation. Note that the simulation parameters of Fig. 6.12 are also scaled down to 1/3. The error is around 8~13%. The error becomes larger as the rotating speed increases. This is because unnecessary vibration of the shake table appears at the high rotating speed.

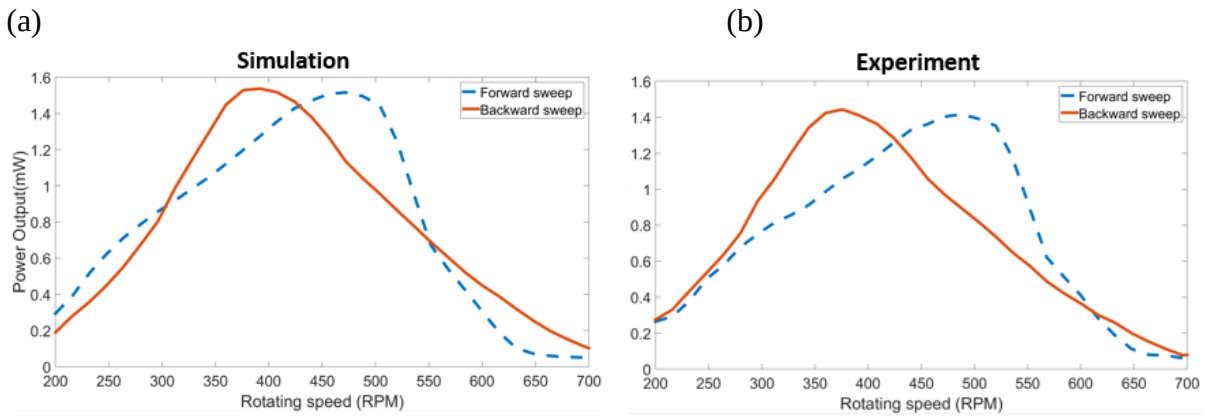

Figure 6.13. Frequency sweep test results. (a) Simulation (b) Experiment

A frequency-swept test was conducted to investigate whether harvester perform well under time varying rotation speed which is closed to real driving condition. Sweep signal at a rate of 1 Hz/s is performed. The sweep frequency response of the harvester is shown in Fig. 6.13. As in the typical nonlinear systems [53,56], hysteresis effect occurs for proposed harvester. Also, stochastic resonance is clearly observed for both up-sweep and down-sweep cases. The experiment results show that the harvester operates well in a frequency varying environment which is closed to real driving condition.

6.6 Field test results

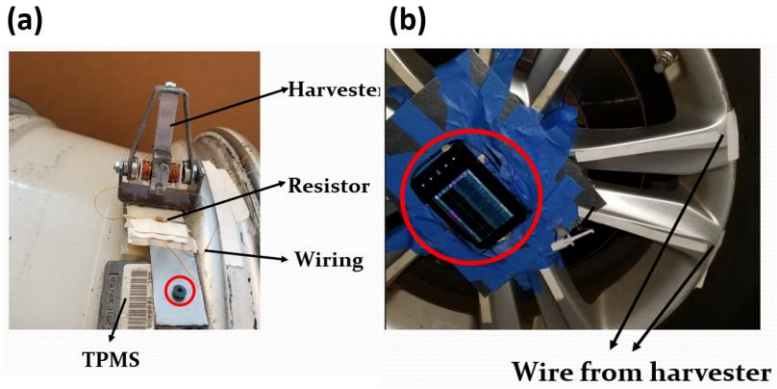

Figure 6.14. Energy harvester prototype for field test.

In this chapter, we performed on-road tests under different driving speeds and record the power with energy harvesting circuit. Also, we will build data transmitter to get various data from sensors As presented in Figure 6.14, Energy harvester and circuit assembly is installed on the tire rim with tire pressure monitoring sensor (TPMS). Power output was measured using DSO nano V3 oscllоscope.

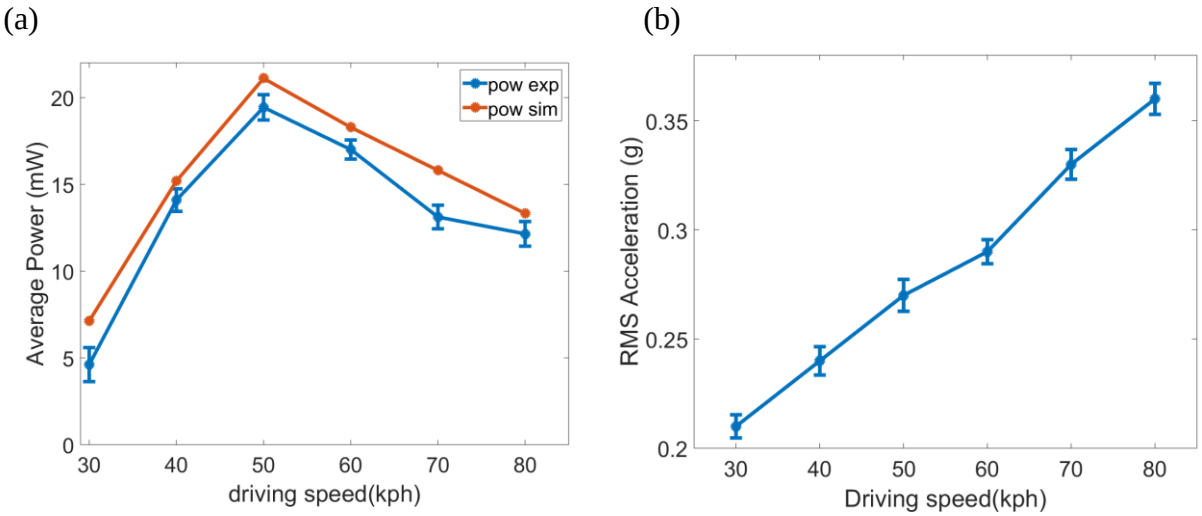

Figure 6.15. Results from the field test. (a) Power output (b) Base acceleration

Figure 6.15 depicts results from road test. Power output was measured for 30, 40, 50, 60, 70 and 80 kph five times each. The results peaked at 50 kph which corresponds to stochastic resonance frequency of the system. Maximum power output was around 18 mW. Noise excitation at the tire also measured to investigate relation between noise intensity and driving speed. The results shows that noise intensity is increased as driving speed increases

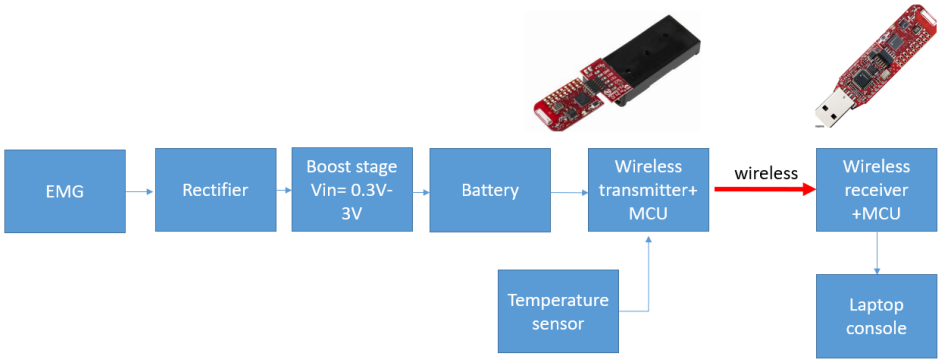

Figure 6.16. Energy harvesting circuit implementation.

The structure of energy harvesting circuit is presented in Figure 6.16. The electric circuit includes a rectifier, buck-boost converter, wireless communication module, and microprocessor. Since voltage level of electromagnetic harvester is not enough to charging the battery, boost converter is used to increase voltage. In this demonstration, temperature of the system is monitored and transmitted through wireless communication module.

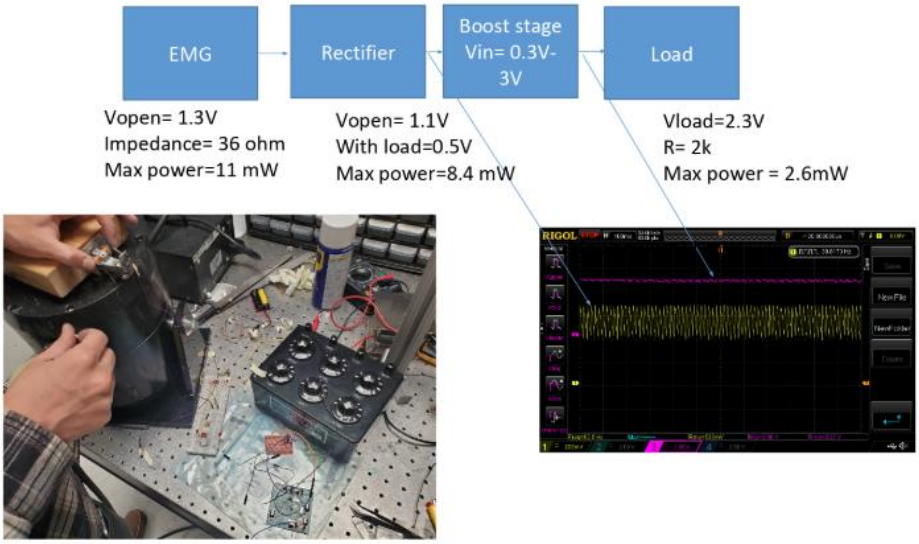

Figure 6.17. Test of energy harvesting circuit with self-tuning energy harvester.

In lab test was conducted with harvester-circuit assembly. Figure 6.17 demonstrates the results. The harvester is excited using Sentek vibration shaker. Initially, maximum power of electromagnetic harvester at optimal load is 11 mW. Power output drops to 2.6 mW because of the rectifier and boost stage. The results output is enough to charge the battery.

6.7 Chapter summary

In this paper, we propose a self-tuning stochastic resonance energy harvester for providing power to smart tires. Passively tuned system is implemented in a rotating tire via centrifugal force. An inward oriented rotating beam is used to induce bistability via the centrifugal acceleration of the tire. Equation of motion of the rotating beam is derived for numerical simulation. To investigate stochastic resonance under modulated noise excitations, a closed-form formula that predicts the signal-to-noise ratio is derived. By using the formula, the stochastic resonance frequency of the harvester is determined. The formula is validated via numerical simulation. Numerical analyses are carried out to investigate the performance of the harvester in a passenger tire. In the simulation, maximum power of 20 mW is achieved. The half-power bandwidth of the harvester is around 52~111 km/h (32 mph ~ 70 mph). Experiment is conducted in a 1/3 scaled horizontal rotating platform to verify the numerical simulation. Both numerical and experimental investigations verify the advantage of the presented energy harvester for smart tires. A frequency sweep test also shows the effectiveness of harvester under frequency varying environment close to real driving conditions.

7. Conclusion and Future work

Up to now following conclusions can be drawn from the work accomplished in this dissertation

1) The dissertation revealed that stochastic resonance is particularly favorable to energy harvesting in rotating systems. Both numerical and experimental results show that stochastic resonance energy harvester has higher power and wider bandwidth than linear harvesters under a rotating environment.
2) The dissertation provides an analysis of how stochastic resonance changes for the various types of excitation that occur in real-world applications. The co-existence of the vibrational & stochastic resonance is observed depending on the periodic signal to noise ratio.
3) Propose energy harvester for the general rotating shaft. For the oil drilling application, the periodic force in rotating shafts is biased, leading to potential function asymmetry. Numerical simulation shows that symmetric potential showed nearly seven times higher power output than the asymmetry cases. To solve the problem, an external magnet was placed above the bi-stable energy harvester to compensate for the biased periodic signal.
4) A self-tuning stochastic resonance energy harvester for the smart tire is proposed. The noise intensity in the rotating tire is amplitude-modulated, therefore, classical stochastic resonance theory cannot apply for this case. The dissertation provides a new analysis method based on signal to noise ratio (SNR). The results show that the stochastic resonance frequency for amplitude-modulated noise is shifted to low value because total excited energy is decreased. To maintain optimal power generation over a wide range of rotating speed, a passively tuned system is implemented in a rotating tire via centrifugal force. An inward-oriented rotating beam is used to induce bistability via the centrifugal acceleration of the tire.

The future work is summarized as follows.

1. Develop an analytical method to predict stochastic resonances with periodically modulated noises and study effects of frequency modulation.

2. Design high efficient energy harvesting circuits and integrate the proposed stochastic energy harvesters.

3. Conduct field tests for oil drilling and smart tire applications with an energy harvesting circuit.

4. Apply a stochastic resonance energy harvesting strategy to various rotating applications. Hard disk, Steal shaft, Gears, etc.

Reference

[1] Lynch JP, and Kenneth JL 2006 A summary review of wireless sensors and sensor networks for structural health monitoring. Shock and Vibration Digest, 38: 91-130.

[2] Park G, Rosing T, Todd MD, Farrar CR, and Hodgkiss W 2008 Energy harvesting for structural health monitoring sensor networks. Journal of Infrastructure Systems, 14: 64-79.

[3] Beeby SP, Tudor MJ, and White NM 2006 Energy harvesting vibration sources for microsystems applications." Measurement science and technology, 17: R175.

[4] Cheli, Federico, et al. "On the impact of 'smart tyres' on existing ABS/EBD control systems." Vehicle System Dynamics 48.S1 (2010): 255-270.

[5] Singh, Kanwar Bharat, Mustafa Ali Arat, and Saied Taheri. "Enhancement of collision mitigation braking system performance through real-time estimation of tire-road friction coefficient by means of smart tires." SAE International journal of passenger cars-electronic and electrical systems 5, no. 2012-01-2014 (2012): 607-624.

[6] Pohl, Alfred, Reinhard Steindl, and Leonhard Reindl. "The "intelligent tire" utilizing passive SAW sensors measurement of tire friction." IEEE transactions on instrumentation and measurement 48.6 (1999): 1041-1046.

[7] Zhang, Xiangwen, et al. "Intelligent tires based on wireless passive surface acoustic wave sensors." Intelligent Transportation Systems, 2004. Proceedings. The 7th International IEEE Conference on. IEEE, 2004.

[8] Todoroki, Akira, Shintaro Miyatani, and Yoshinobu Shimamura. "Wireless strain monitoring using electrical capacitance change of tire: part I—with oscillating circuit." Smart Materials and Structures 12.3 (2003): 403.

[9] Todoroki, Akira, Shintaro Miyatani, and Yoshinobu Shimamura. "Wireless strain monitoring using electrical capacitance change of tire: part II—passive." Smart Materials and Structures 12.3 (2003): 410.

[10] Matsuzaki, Ryosuke, and Akira Todoroki. "Intelligent tires based on measurement of tire deformation." Journal of solid mechanics and Materials engineering 2.2 (2008): 269-280.

[11] Braghin, F., et al. "Future car active controls through the measurement of contact forces and patch

features." Veh. Syst. Dyn 44 (2006): 3-13.

[12]Matsuzaki, Ryosuke, and Akira Todoroki. "Wireless monitoring of automobile tires for intelligent tires." Sensors 8.12 (2008): 8123-8138.

[13]Kubba, Ali E., and Kyle Jiang. "A comprehensive study on technologies of tyre monitoring systems and possible energy solutions." Sensors 14.6 (2014): 10306-10345.

[14]Bowen, C. R., and M. H. Arafa. "Energy harvesting technologies for tire pressure monitoring systems." Advanced Energy Materials 5.7 (2015).

[15]Van den Ende, D. A., H. J. Van de Wiel, W. A. Groen, and S. Van der Zwaag. "Direct strain energy harvesting in automobile tires using piezoelectric PZT–polymer composites." Smart materials and structures 21, no. 1 (2011): 015011.

[16]Wang, Yu-Jen, Chung-De Chen, and Cheng-Kuo Sung. "System design of a weighted-pendulum-type electromagnetic generator for harvesting energy from a rotating wheel." IEEE/ASME Transactions on Mechatronics 18, no. 2 (2013): 754-763.

[17]Tornincasa, Stefano, et al. "Energy harvester for vehicle tires: Nonlinear dynamics and experimental outcomes." Journal of Intelligent Material Systems and Structures 23.1 (2012): 3-13.

[18]Singh, Kanwar Bharat, et al. "Piezoelectric vibration energy harvesting system with an adaptive frequency tuning mechanism for intelligent tires." Mechatronics 22.7 (2012): 970-988

[19]Keck, Marian. "A new approach of a piezoelectric vibration-based power generator to supply next generation tire sensor systems." Sensors, 2007 IEEE. IEEE, 2007.

[20]Khameneifar, Farbod, and Siamak Arzanpour. "Energy harvesting from pneumatic tires using piezoelectric transducers." ASME 2008 Conference on Smart Materials, Adaptive Structures and Intelligent Systems. American Society of Mechanical Engineers, 2008.

[21]Hatipoglu, G., and H. Urey. "FR4-based electromagnetic energy harvester for wireless tyre sensor nodes." Procedia Chemistry 1.1 (2009): 1211-1214.

[22]Zhu, Dibin, Michael J. Tudor, and Stephen P. Beeby. "Strategies for increasing the operating frequency range of vibration energy harvesters: a review." Measurement Science and Technology 21.2 (2009): 022001.

[23]Daqaq, Mohammed F., et al. "On the role of nonlinearities in vibratory energy harvesting: a critical review and discussion." Applied Mechanics Reviews 66.4 (2014): 040801.

[24]Gammaitoni, Luca, et al. "Stochastic resonance." Reviews of modern physics 70.1 (1998): 223.

[25]McInnes, C. R., D. G. Gorman, and Matthew P. Cartmell. "Enhanced vibrational energy harvesting using nonlinear stochastic resonance." Journal of Sound and Vibration 318.4 (2008): 655-662.

[26]Zhang, Y., et al. "Broadband vibration energy harvesting by application of stochastic resonance from rotational environments." Eur. Phys. J. Spec. Top 224 (2015): 2687-2701.

[27]Zhang, Yunshun, et al. "Effectiveness testing of a piezoelectric energy harvester for an automobile wheel using stochastic resonance." Sensors 16.10 (2016): 1727.

[28]Gu, Lei, and Carol Livermore. "Passive self-tuning energy harvester for extracting energy from rotational motion." Applied Physics Letters 97.8 (2010): 081904.

[29]Zheng, Rencheng, et al. "An application of stochastic resonance for energy harvesting in a bistable vibrating system." Journal of Sound and Vibration 333.12 (2014): 2568-2587.

[30]Kim, Hongjip, et al. "Stochastic resonance energy harvesting for a rotating shaft subject to random and periodic vibrations: influence of potential function asymmetry and frequency sweep." Smart Materials and Structures 26.11 (2017): 115011.

[31]Turhan, Özgür, and Bulut, Gökhan. "On nonlinear vibrations of a rotating beam." Journal of sound and vibration 322.1-2 (2009): 314-335.

[32]Mann BP, and Sims ND 2009 Energy harvesting from the nonlinear oscillations of magnetic levitation. Journal of Sound and Vibration, 319(1), 515-530

[33]Mioduszewski,P. "Speed influence on tire/road noise inside a passenger car." Internoise 2000.Proceedings of the 29th international congress on noise control engineering, 2000, Voulume 2.

[34]He, Qifan, and Mohammed F. Daqaq. "Influence of potential function asymmetries on the performance of nonlinear energy harvesters under white noise." Journal of Sound and Vibration 333.15 (2014): 3479-3489.

[35] He, Qingbo, et al. "Multiscale noise tuning of stochastic resonance for enhanced fault diagnosis in rotating machines." Mechanical Systems and Signal Processing 28 (2012): 443-457.

[36] Benzi, Roberto, Alfonso Sutera, and Angelo Vulpiani. "The mechanism of stochastic resonance." Journal of Physics A: mathematical and general 14.11 (1981): L453.

[37] Hänggi, Peter, Peter Talkner, and Michal Borkovec. "Reaction-rate theory: fifty years after Kramers." Reviews of modern physics 62.2 (1990): 251.

[38] Zheng, Wei-mou. "Square-wave-driven stochastic resonance." Physical Review A 44.10 (1991): 6443.

[39] Su, Dongxu, et al. "On square-wave-driven stochastic resonance for energy harvesting in a bistable system." AIP Advances 4.11 (2014): 117140.

[40] Rajasekar, Shanmuganathan, and Miguel AF Sanjuan. Nonlinear resonances. Switzerland: Springer International Publishing, 2016.

[41] McNamara, B. "B. McNamara and K. Wiesenfeld, Phys. Rev. A 39, 4854 (1989)." Phys. Rev. A 39 (1989): 4854.

[42] Masana, Ravindra, and Mohammed F. Daqaq. "Relative performance of a vibratory energy harvester in mono-and bi-stable potentials." Journal of Sound and Vibration 330.24 (2011): 6036-6052

[43] P.Gross, M.Gu¨rgo¨ze, W.Kliem, Bifurcation and stability analysis of a rotating beam, Quarterly of Applied Mathematics 51 (4) (1993) 701–711

[44] Nonlinear analysis of the buckling and vibration of a rotating elasticum." International journal of mechanical sciences 36.7 (1994): 673-681

[45] Zohoor, H. and Kakavand, F., 2012. Vibration of Euler–Bernoulli and Timoshenko beams in large overall motion on flying support using finite element method. Scientia Iranica, 19(4), pp.1105-1116

[46] Lynch JP, and Kenneth JL 2006 A summary review of wireless sensors and sensor networks for structural health monitoring. Shock and Vibration Digest, 38: 91-130.

[47] Park G, Rosing T, Todd MD, Farrar CR, and Hodgkiss W 2008 Energy harvesting for structural health monitoring sensor networks. Journal of Infrastructure Systems, 14: 64-79.

[48] Beeby SP, Tudor MJ, and White NM 2006 Energy harvesting vibration sources for microsystems applications." Measurement science and technology, 17: R175.

[49] Leine RI, Van Campen DH, and Keultjes WJG 2002 Stick-slip whirl interaction in drillstring dynamics. Journal of Vibration and Acoustics, 124: 209-220.

[50] Xue Q, Wang R, Sun F, and Huang Z 2014 Chaotic vibration analysis of the bottom rotating drill string. Shock and Vibration, 2014: 429164.
[51] Adams ML 2000 Rotating machinery vibration. Vibrations-Willowbrook, 16: 12-13.
[52] Zhao S, and Erturk A 2013 On the stochastic excitation of monostable and bistable electroelastic power generators: relative advantages and tradeoffs in a physical system. Applied Physics Letters, 102: 103902.
[53] Cottone F, Vocca H, and Gammaitoni L 2009 Nonlinear energy harvesting. Physical Review Letters, 102: 080601.
[54] Masana R, and Daqaq MF 2011 Relative performance of a vibratory energy harvester in mono-and bi-stable potentials. Journal of Sound and Vibration 330: 6036-6052.
[55] Gammaitoni L, Hänggi P, Jung P, and Marchesoni F 1998 Stochastic resonance. Reviews of modern physics, 70: 223.
[56] McInnes, CR, Gorman DG, and Cartmell MP 2008 Enhanced vibrational energy harvesting using nonlinear stochastic resonance. Journal of Sound and Vibration 318: 655-662.
[57] Su D, Zheng R, Nakano K, and Cartmell MP 2014 On square-wave-driven stochastic resonance for energy harvesting in a bistable system. AIP Advances, 4: 117140.
[58] Zhang Y, Zheng R, Kaizuka T, Su D, Nakano K, and Cartmell MP 2015 Broadband vibration energy harvesting by application of stochastic resonance from rotational environments. The European Physical Journal Special Topics, 224: 2687-2701.
[59] Zheng R, Nakano K, Hu H, Su D, and Cartmell MP 2014 An application of stochastic resonance for energy harvesting in a bistable vibrating system. Journal of Sound and Vibration, 333: 2568-2587.
[60] Bouzat S, and Wio HS 1999 Stochastic resonance in extended bistable systems: The role of potential symmetry. Physical Review E, 59: 5142.
[61] Li JH 2002 Effect of asymmetry on stochastic resonance and stochastic resonance induced by multiplicative noise and by mean-field coupling. Physical Review E, 66: 031104.
[62] Perc M 2009 Stochastic resonance on paced genetic regulatory small-world networks: effects of asymmetric potentials. The European Physical Journal B-Condensed Matter and Complex Systems, 69: 147-153.

[63] He Q, and Daqaq MF 2014 Influence of potential function asymmetries on the performance of nonlinear energy harvesters under white noise. Journal of Sound and Vibration, 333: 3479-3489.
[64] Kim H, Tai WC, and Zuo L 2017 Stochastic resonance energy harvesting from general rotating shaft vibrations. SPIE Smart Structures and Materials+ Nondestructive Evaluation and Health Monitoring. International Society for Optics and Photonics, 2017, doi:10.1117/12.2259805 [65] Chevallier AM 2001 Nonlinear stochastic drilling vibrations. Doctoral dissertation, Rice University.
[66] Berry JE 2005 Oil whirl and whip instabilities—within journal bearings. Machinery lubrication magazine, May (2005), Issue 200505.
[67] Alford JS 1965 Protecting turbomachinery from self-excited rotor whirl. Journal of Engineering for Power, 87: 333-343.
[68] Tang L, Zhu X, Shi C, Tang J ,and Xu D 2015 Study of the influences of rotary table speed on stick-slip vibration of the drilling system. Petroleum, 1(4), pp.382-387.
[69] Mann BP, and Sims ND 2009 Energy harvesting from the nonlinear oscillations of magnetic levitation. Journal of Sound and Vibration, 319(1), 515-530.
[70] Zhou S, Cao J, Inman DJ, Lin J, Liu S, and Wang Z 2014 Broadband tristable energy harvester: modeling and experiment verification. Applied Energy, 133: 33-39.
[71] Perc M 2009 Stochastic resonance on paced genetic regulatory small-world networks: effects of asymmetric potentials. The European Physical Journal B-Condensed Matter and Complex Systems, 69: 147-153
[72] Benzi, R., Sutera, A. and Vulpiani, A. 1981 "The mechanism of stochastic resonance." Journal of Physics A: mathematical and general 14.11: L453.
[73] McNamara, B., Wiesenfeld, K. and Roy, R. 1988 "Observation of stochastic resonance in a ring laser." Physical Review Letters 60.25: 2626.
[74] Melnikov, V. I. "Schmitt trigger: A solvable model of stochastic resonance." 1993 Physical Review E 48.4 : 2481.
[75] Simonotto, E., Riani, M., Seife, C., Roberts, M., Twitty, J., & Moss, F. 1997 "Visual perception of stochastic resonance." Physical review letters 78.6 :1186.
[76] McInnes, CR, Gorman DG, and Cartmell MP 2008 Enhanced vibrational energy harvesting using nonlinear stochastic resonance. Journal of Sound and Vibration 318: 655-662.

[77] Wiggert, M. C., and D. C. Potter. "Mechanics of fluids." *Cengage Learning, Stamford, USA* (2002).
Li, S., Peng, Z., Zhang, A. and Wang, F. 2016 "Dual resonant structure for energy harvesting from random vibration sources at low frequency." Aip Advances 6.1 : 015019.
[78] Zhang Y, Zheng R, Kaizuka T, Su D, Nakano K, and Cartmell MP 2015 Broadband vibration energy harvesting by application of stochastic resonance from rotational environments. The European Physical Journal Special Topics
, 224: 2687-2701.
[79] Zheng R, Nakano K, Hu H, Su D, and Cartmell MP 2014 An application of stochastic resonance for energy harvesting in a bistable vibrating system. Journal of Sound and Vibration, 333: 2568-2587.
[80] Kim H, Tai W C, Parker J and Zuo L 2019 Self-tuning stochastic resonance energy harvesting for rotating systems under modulated noise and its application to smart tires Mech. Syst. Signal Process.
[81] Kim, H., Tai, W.C., Zhou, S. and Zuo, L 2017 "Stochastic resonance energy harvesting for a rotating shaft subject to random and periodic vibrations: influence of potential function asymmetry and frequency sweep." Smart Materials and Structures 26.11 : 115011
[82] Gammaitoni, L., Hänggi, P., Jung, P. and Marchesoni, F 1998 "Stochastic resonance." Reviews of modern physics 70.1 : 223.
[83] Fournie, David-Antoine. *Functional Ito calculus and applications*. Columbia University, 2010. Rajasekar, S. and Sanjuan, M.A., 2016. Nonlinear resonances. Switzerland: Springer International Publishing.
[84] Ghasemi, Fatemeh, et al. "Markov analysis and Kramers-Moyal expansion of nonstationary stochastic processes with application to the fluctuations in the oil price." *Physical Review E* 75.6 (2007): 060102.
[85] Tessone, C.J., Wio, H.S. and Hänggi, P., 2000. Stochastic resonance driven by time-modulated correlated white noise sources. Physical Review E, 62(4), p.4623.
[86] Cottone F, Vocca H, and Gammaitoni L 2009 Nonlinear energy harvesting. Physical Review Letters, 102: 080601.
[87] Casado-Pascual, J., Gómez-Ordónez, J., Morillo, M. and Hänggi, P., 2003. Two-state theory of

[88] Kuperman, M.N., Wio, H.S., Izús, G. and Deza, R., 1998 "Stochastic resonant media: Signal-to-noise ratio for the activator-inhibitor system through a quasivariational approach." Physical Review E 57.5 (1998): 5122.

[89] Siewert, U. and Schimansky-Geier, L., 1998. Analytical study of coupled two-state stochastic resonators. Physical Review E, 58(3), p.2843.

[90] McNamara, Bruce, and Kurt Wiesenfeld. 1989 "Theory of stochastic resonance." Physical review A 39.9 : 4854.

[91] McNamara, B. and Wiesenfeld, K., 1989. Theory of stochastic resonance. Physical review A, 39(9), p.4854.

[92] Lindner, J.F., Meadows, B.K., Ditto, W.L., Inchiosa, M.E. and Bulsara, A.R., 1995. Array enhanced stochastic resonance and spatiotemporal synchronization. Physical Review Letters, 75(1), p.3.

[93] Neiman, A. and Schimansky-Geier, L., 1995. Stochastic resonance in two coupled bistable systems. Physics Letters A, 197(5-6), pp.379-386.

[94] He Q, and Daqaq MF 2014 Influence of potential function asymmetries on the performance of nonlinear energy harvesters under white noise. Journal of Sound and Vibration, 333: 3479-3489.

[95] Gitterman, M. "Harmonic oscillator with fluctuating damping parameter." Physical Review E 69.4 (2004): 041101.

[96] Langley, R. S. "A finite element method for the statistics of non-linear random vibration." Journal of Sound and Vibration 101.1 (1985): 41-54.

[97] Mann BP, and Sims ND 2009 Energy harvesting from the nonlinear oscillations of magnetic levitation. Journal of Sound and Vibration, 319(1), 515-530.

[98] Rozanov, Yurii A. Probability theory: a concise course. Courier Corporation, 2013.

[99] Soong, Tsu T., and Mircea Grigoriu. "Random vibration of mechanical and structural systems." NASA STI/Recon Technical Report A 93 (1993).

[100] Lutes, Loren D., and Shahram Sarkani. Random vibrations: analysis of structural and mechanical systems. Butterworth-Heinemann, 2004.

Appendices

Appendix A

Equation of motion of rotating beam

Figure A1 shows the free body diagram of a cantilever Euler-Bernoulli beam clamped off the rotational axis and oriented inward. To describe the deformation of the beam, a curvilinear coordinate s is used to describe the position of the neutral axis of the beam during deformation, i.e., the Lagrangian description is used [77]. In addition, the beam position can be described by the x and y coordinates (Eulerian description). The beam is assumed to be inextensible and undergo

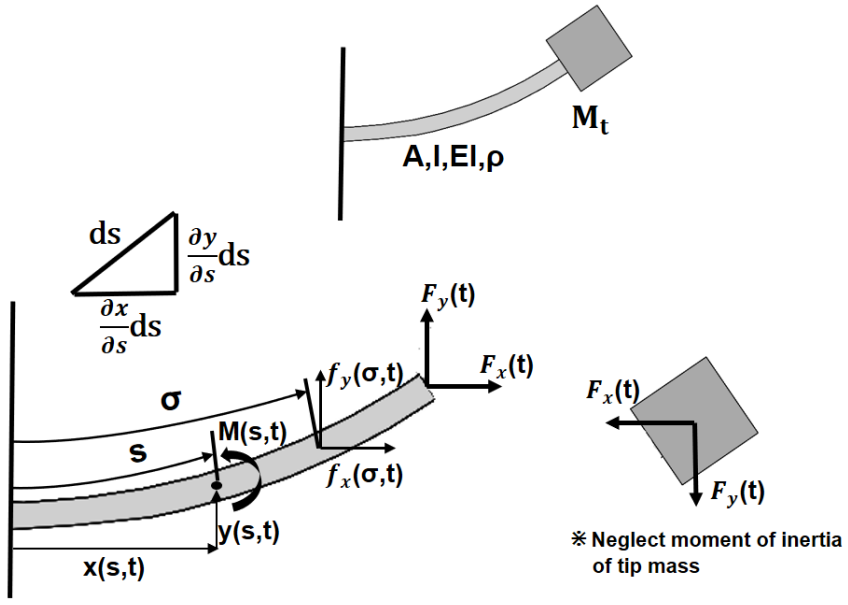

Figure A.1 Freebody diagram of the rotating beam with tip mass.

moderately large transverse vibrations. For the beam being inextensible, the following geometric relation holds

$$\left(\frac{\partial x}{\partial s}\right)^2 + \left(\frac{\partial y}{\partial s}\right)^2 = 1 \text{ or } \frac{\partial x}{\partial s} = \sqrt{1 - \left(\frac{\partial y}{\partial s}\right)^2} \cong 1 - \frac{1}{2}\left(\frac{\partial y}{\partial s}\right)^2 \tag{A.1}$$

where the binomial expansion is used and the second order nonlinear term is retained to consider the moderately large transverse deformation. With Eqn. (A1), the curvature $\kappa(s,t)$ of the deformed beam is approximated to the same order of accuracy as

$$\kappa(s,t) = \frac{\frac{\partial^2 y}{\partial s^2}}{\sqrt{1-\left(\frac{\partial y}{\partial s}\right)^2}} \cong \frac{\partial^2 y}{\partial s^2}\left(1 + \frac{1}{2}\left(\frac{\partial y}{\partial s}\right)^2\right) \tag{A.2}$$

The beam is subjected to distributed forces $f_x(s,t)$ and $f_y(s,t)$ and tip forces F_x and F_y in the x and y direction. The distributed forces include the inertial forces $f_x^{\Omega}(s,t)$ and $f_y^{\Omega}(s,t)$ due to tire rotation, inertial forces $\hat{f}_x(s,t)$ and $\hat{f}_y(s,t)$ due to vibrations observed in the rotating coordinate system and gravity and noise excitations. In other words,

$$f_x(s,t) = f_x^{\Omega}(s,t) + \hat{f}_x(s,t) \text{ and } f_y(s,t) = f_y^{\Omega}(s,t) + \hat{f}_y(s,t), \text{ where}$$

$$f_x^{\Omega}(s,t) = \rho A\left\{\Omega^2\left[R + \int_0^s \left(1 - \frac{1}{2}\left(\frac{\partial y}{\partial \sigma}\right)^2\right) \mathrm{d}\sigma\right] + 2\Omega\frac{\partial y}{\partial t}\right\}$$

$$f_y^{\Omega}(s,t) = \rho A\left\{\Omega^2 y + 2\Omega\int_0^s \frac{\partial y}{\partial \sigma}\frac{\partial^2 y}{\partial \sigma \partial t}\mathrm{d}\sigma\right\}$$

$$\hat{f}_x(s,t) = \rho A\int_0^s \left[\left(\frac{\partial^2 y}{\partial \sigma \partial t}\right)^2 + \frac{\partial y}{\partial \sigma}\frac{\partial^3 y}{\partial \sigma \partial t^2}\right]\mathrm{d}\sigma$$

$$\hat{f}_y(s,t) = -\rho A\int_0^s \frac{\partial y}{\partial \sigma}\frac{\partial^2 y}{\partial t^2}\mathrm{d}\sigma$$

$$f_x^{\mathrm{g}}(s,t) = -\rho A g\cos\Omega t \text{ and } f_x^{\mathrm{N}}(s,t) = -\rho A N(t)\cos\Omega t$$

$$f_y^{\mathrm{g}}(s,t) = \rho A g\sin\Omega t \text{ and } f_y^{\mathrm{N}}(s,t) = \rho A N(t)\sin\Omega t$$

(A.3)

Consider a tip mass M_t and neglect its moment of inertia. The tip forces due to the tip mass can then be simplified as concentrated forces acting upon the beam tip. Referring to Fig. A1, by summing all the applied forces and applying Newton's 2nd law to the tip mass, the tip forces can be derived as

$$F_x(t) = M_t a_x(L,t) = M_t \frac{\hat{f}_x(L,t) + f_x^{\Omega}(L,t) + f_x^{\mathrm{g}}(L,t) + f_x^{\mathrm{N}}(L,t)}{\rho A}$$

$$\cong M_t \Omega^2 \left[R + \int_0^L \left(1 - \frac{1}{2}\left(\frac{\partial y}{\partial \sigma}\right)^2 \right) \mathrm{d}\sigma \right]$$

$$F_y(t) = -M_t a_y(L,t) = -M_t \frac{\hat{f}_y(L,t) + f_y^{\Omega}(L,t) + f_y^{\mathrm{g}}(L,t) + f_y^{\mathrm{N}}(L,t)}{\rho A} \cong M_t \Omega^2 y(L,t)$$

(A.4)

where $a_x(L,t)$ and $a_y(L,t)$ are the accelerations at the tip, which are obtained by substituting L for s into Eqn. (A.3). In this paper, we are interested in how the tip mass enhances buckling the beam via the centrifugal acceleration; therefore, only distributed forces which are associated with centrifugal acceleration are retained in (A.4). This is justified when the rotation speed is high as the magnitude of centrifugal forces are proportional to the square of the rotation speed whereas other terms do not or linearly depend on the rotation speed.

With Eqns. (A.3-4), the moment $M(s,t)$ at an arbitrary point s on the beam can be derived as

$$M(s,t) = -F_x(t) \int_s^L \frac{\partial y}{\partial \eta} \mathrm{d}\eta - \int_s^L \left(f_x(\sigma,t) \int_s^{\sigma} \frac{\partial y}{\partial \eta} \mathrm{d}\eta \right) \mathrm{d}\sigma + F_y(t) \int_s^L \left(1 - \frac{1}{2}\left(\frac{\partial y}{\partial \eta}\right)^2 \right) \mathrm{d}\eta +$$

$$\int_s^L \left(f_y(\sigma,t) \int_s^{\sigma} \left(1 - \frac{1}{2}\left(\frac{\partial y}{\partial \eta}\right)^2 \right) \mathrm{d}\eta \right) \mathrm{d}\sigma \qquad \text{(A.5)}$$

Note that the integrals follow the tip and distributed forces are the moment arms with respect to the point s. The governing equation of the beam bending at a point s is then derived using $M(s,t) = \kappa(s,t)EI$, where EI are the bending rigidity which is assumed to be constant.

Substitution Eqns. (A.5) into $M(s,t) = \kappa(s,t)EI$ via (A.2-4), and taking the second partial derivative with respect to s by using the Leibniz rule lead to [31]

$$\rho A\{[1-\frac{1}{2}(\frac{\partial y}{\partial s})^2]\frac{\partial^2 y}{\partial t^2}+\frac{\partial y}{\partial s}\frac{\partial^2 y}{\partial s^2}\int_s^L \frac{\partial^2 y}{\partial t^2}\,d\sigma\}+\frac{\partial y}{\partial s}\hat{f}_x(s,t)-\frac{\partial^2 y}{\partial s^2}\int_s^L \hat{f}_x(\sigma,t)\,\mathrm{d}\sigma+EI\left\{[1+\frac{1}{2}(\frac{\partial y}{\partial s})^2]\frac{\partial^4 y}{\partial s^4}+3\,\frac{\partial y}{\partial s}\,\frac{\partial^2 y}{\partial s^2}\,\frac{\partial^3 y}{\partial s^3}+(\frac{\partial^2 y}{\partial s^2})^3\right\}-\frac{\partial^2 y}{\partial s^2}\left[F_x+\int_s^L\left(f_x^{\Omega}(\sigma,t)+f_x^{\mathrm{g}}(s,t)+f_x^{\mathrm{N}}(s,t)\right)\mathrm{d}\sigma\right]-\frac{\partial y}{\partial s}\frac{\partial^2 y}{\partial s^2}\left[F_y+\int_s^L f_y^{\Omega}(\sigma,t)\mathrm{d}\sigma\right]+\left(f_x^{\Omega}(\sigma,t)+f_x^{\mathrm{g}}(s,t)+f_x^{\mathrm{N}}(s,t)\right)\frac{\partial y}{\partial s}-f_y^{\Omega}(\sigma,t)\left[1-\frac{1}{2}(\frac{\partial y}{\partial s})^2\right]=0 \quad \text{(A.6)}$$

Note that in deriving (A.1), the nonlinear terms associated with the noise and gravity excitation are neglected as they are very small compared with those induced by tire rotation.

Galerkin's method is used to obtain a weak form solution for Eqn (A.1). Note that the dimensionless variables $u = s/L, v = y/L$ and $\mu = \frac{M_t}{\rho AL}$ along with the dimensionless parameters introduced in Eqn. (A.6) are introduced to obtain the solution. To this end, one introduces the Galerkin expansion

$v(u,\tau) = \sum_{i=1}^{n} g_i(\tau)\varphi_i(u)$

where $\varphi_i(u)$ is the i-th shape fuction and $g_i(u)$ is the corresponding generalized coordinate.

In this study, eigen-function of the linear cantilever beam with tip mass is chosen to be the shape function [45]

$$\varphi_i(u) = (\cos\lambda_i u - \cosh\lambda_i u) + \kappa_i(\sin\lambda_i u - \sinh\lambda_i u),\ \kappa_i = \left(\frac{\sin\lambda_i - \sinh\lambda_i + \lambda_i\mu(\cos\lambda_i - \cosh\lambda_i)}{\cos\lambda_i + \cosh\lambda_i - \lambda_i\mu(\sin\lambda_i - \sinh\lambda_i)}\right) \quad \text{(A.7)}$$

Where the λ_i is the eigenvalue of the characteristic equation,

$$1+\cos\lambda_i\cosh\lambda_i + \mu\,\lambda_i(\cos\lambda_i\sinh\lambda_i - \sin\lambda_i\cosh\lambda_i)=0 \quad \text{(A.8)}$$

Applying Galerkin's procedure to Eqn. (A.1), one obtains

$$\ddot{g}_i + 2\zeta\lambda_i\dot{g}_i + \lambda_i^4 g_i -$$

$$\beta^2 \sum_{j=1}^{n}(\alpha A_{ij}+B_{ij}+\delta_{ij}))\, g_j+2\beta \sum_{j=1}^{n}\sum_{k=1}^{n} G_{ijkl}\, g_j\, \dot{g}_k+\sum_{j=1}^{n}\sum_{k=1}^{n}\sum_{l=1}^{n}[\, C_{ijkl} g_j g_k \ddot{g}_l +$$

$$D_{ijkl} g_j \dot{g}_k \dot{g}_l+(E_{ijkl} - \beta^2 F_{ijkl})\, g_j g_k g_l]= K\varepsilon \sin\beta\tau + K\varepsilon n(\tau)\, sin\, \beta\tau \qquad \text{(A.9)}$$

The coupling terms $g_j\dot{g}_k$, $g_j g_k\ddot{g}_l$ and $g_j\dot{g}_k\dot{g}_l$ are related to Coriolis force and inertia force due to vibrations observed in the rotating coordinate system and are negligible when compared with rotation-related inertial forces, especially after the beam is buckled at high rotation speed. $2\zeta\lambda_i\dot{g}_i$ represents a general modal damping term. [31] (For the visco-elastic material cases, it is $2\zeta\lambda_i^4\dot{g}_i$. [77])

Thus, Eq. (A.7) is reduced to a set of 2nd order ordinary differential equations with cubic stiffness nonlinearity,

$$\ddot{g}_i + 2\zeta\lambda_i\dot{g}_i + \lambda_i^4 g_i - \beta^2 \sum_{j=1}^{n}(\alpha\,(A_{ij} + A_{ij}^{\mu})+(B_{ij} + B_{ij}^{\mu})+\delta_{ij})\, g_j+(E_{ijkl} - \beta^2(F_{ijkl} +$$

$$F_{ijkl}^{\mu}))\, g_j g_k g_l]= K\varepsilon \sin\beta\tau + K\varepsilon n(\tau)\sin\beta\tau \qquad \text{(A.10)}$$

Where the coefficient $A_{ij}, B_{ij}, E_{ijkl}, F_{ijkl}$ are

$$A_{ij}=\int_0^1[(1-u)\,\varphi_j^{''} - \varphi_j^{'}]\,\varphi_i du$$

$$A_{ij}^{\mu} = \int_0^1 \mu\varphi_j^{''}\varphi_i du$$

$$B_{ij}=\int_0^1[\{\tfrac{1}{2}(1-u^2)\}\,\varphi_j^{''} - u\varphi_j^{'}]\,\varphi_i du$$

$$B_{ij}^{\mu} = \int_0^1 \mu\varphi_j^{''}\varphi_i du$$

$E_{ijkl} = \int_0^1 [\frac{1}{2} \varphi_j'''' \varphi_k' \varphi_l' + 3\varphi_j' \varphi_k'' \varphi_l''' + \varphi_j'' \varphi_k'' \varphi_l''] \varphi_i du$

$F_{ijkl} = \int_0^1 [\frac{1}{2} \varphi_j' \int_0^u \varphi_k' \varphi_l' d\sigma + \varphi_j' \varphi_k'' \int_u^1 \varphi_l \, d\sigma - \frac{1}{2} \varphi_j'' \int_u^1 \int_0^\sigma \varphi_k' \varphi_l' \, d\eta d\sigma + -\frac{1}{2} \varphi_j \varphi_k' \varphi_l'] \varphi_i du, ,$

$F_{ijkl}^{\mu} = \mu \int_0^1 [\varphi_j' \varphi_k'' - \frac{1}{2} \varphi_j'' \int_0^1 \varphi_k' \varphi_l' d\sigma] \varphi_i du$

To get first mode set i=1(g_1=q)

$\ddot{q} + 2\zeta\lambda_i \dot{q} + [\lambda_1^4 - (A_{11}\alpha + B_{11} + 1)\beta^2]q + (E_{1111} - F_{1111}\beta^2)q^3 = K\varepsilon \sin\beta\tau +$

$K\varepsilon n(\tau) \sin\beta\tau$ (A.11)

Appendix B

Signal to noise ratio of electromagnetic energy harvester

The procedure proposed in ref. [97] is used for calculating signal-to-noise of the proposed harvester in thesis.

The autocorrelation of Eq. (B.1) can be calculated via the two-state method proposed by McNamara and Wiesenfeld [98] as follows.

$$<q(t)q(t+\tau)> = \frac{k_1}{k_3} e^{-\alpha_0|\tau|}[1-\frac{\alpha_1 f_0 \cos(\beta t-\varphi)}{(\alpha_0^2+\beta^2)^{\frac{1}{2}}}]+ \frac{\frac{k_1}{k_3}\alpha_1^2 f_0^2\{\cos\beta\tau+\cos(\beta(2t+\tau)+2\varphi]\}}{2(\alpha_0^2+\beta^2)} \quad (B.1)$$

where φ denotes an arbitrary phase and

$$f_0=\frac{K\varepsilon\sqrt{\frac{k_1}{k_3}}}{D},\ \alpha_0=\frac{k_1^2\sqrt{2}}{\pi\beta} e^{-\frac{k_1^2}{3D\beta k_3}},\ \alpha_1=\frac{k_1^2 2\sqrt{2}}{\pi\beta} e^{-\frac{k_1^2}{3D\beta k_3}} \quad (B.2)$$

where D, K, k_1, k_3, β, and ε are defined in Eqns. (B.2-4). The power spectrum can be obtained by taking Fourier transform of the autocorrelation, i.e.,

$$<S(\omega)>_t = s_n + s_s\delta(\omega-\beta) \quad (B.3)$$

where $s_s=\frac{\pi\frac{k_1}{k_3}\alpha_1^2 f_0^2}{\alpha_0^2+\beta^2}$, $s_n=\frac{4\frac{k_1}{k_3}\alpha_0}{\alpha_0^2+\omega^2}(1-\frac{\alpha_1^2 f_0^2}{2(\alpha_0^2+\beta^2)})$ and ω denotes frequency of Fourier transform.

Finally, the signal-to-noise ratio (SNR) is derived as

$$\text{SNR} = \frac{s_s(\beta)}{s_n(\omega=\beta,\beta)}= \frac{2\sqrt{2}k_1^3(K\varepsilon)^2}{\beta D^2 k_3} e^{-\frac{k_1^2}{3D\beta k_3}}[1-\frac{\frac{3k_1^3(K\varepsilon)^2}{10\pi^2 D^2 k_3}e^{-\frac{5k_1^2}{6Dk_3}}}{\frac{2k_1^2}{\pi^2}e^{-\frac{5k_1^2}{6Dk_3}}+\beta^2}]^{-1} \approx \frac{2\sqrt{2}k_1^3(K\varepsilon)^2}{\beta D^2 k_3} e^{-\frac{k_1^2}{3D\beta k_3}} \quad (B.4)$$

Appendix C

Calculation of average power from probability density function

Let X be a continuous random variable with the range [a,b]. Every continuous random variable X has probability density function, written in P(x), that satisfies the following conditions. [99]

1) $P(x) \geq 0$ for all x
2) $\int_{-\infty}^{\infty} P(x)dx = 1$

The probability that a random variable X takes on values in the interval $a \leq X \leq b$ is defined as

$$P(a \leq X \leq b) = \int_{a}^{b} P(x)dx \qquad (C.1)$$

Which is the area under the curve f(x) from x=a and x=b

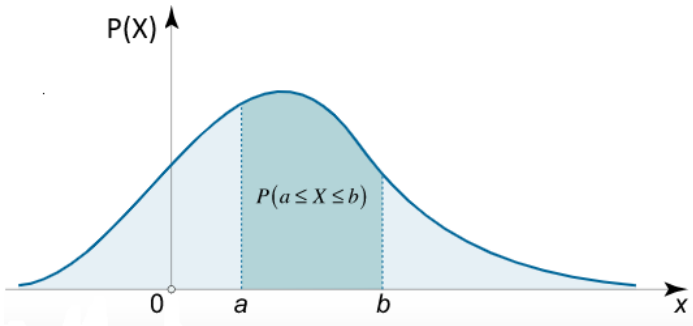

Figure C.1 The curve of probability density function and its probability.

For multiple continuous random variable X_1,.., X_n, it is also possible to define a probability density function associated to the set as a whole, often called joint probability density function. This density function is defined as a function of the *n* variables, such that, for any domain *D* in the *n*-dimensional space of the values of the variables X_1, ..., X_n, the probability that a realization of the set variables falls inside the domain *D* is

$$P(X_1,\ldots, X_n \in D) = \int_D P_{X_1,\ldots,X_n}(x_1,\ldots, x_n)dx_1 \cdots dx_n \qquad (C.2)$$

Expected value of X is defined by [100]

$$E(X) = \int_{-\infty}^{\infty} xP(x)dx \tag{C.3}$$

For multi variable cases, (C.3) can be written as

$$E(\prod_{i=1}^{n} X_i) = \int_{-\infty}^{\infty} \cdots \int_{-\infty}^{\infty} \prod_{i=1}^{n} X_i P_{X_1,..,X_n}(x_1,..,x_n)\ dx_1 \cdots dx_n \tag{C.4}$$

The probability density function introduced in this dissertation has two random variables: Displacement x_1 and velocity x_2.

Harvester power for deterministic system is [97]

$$w = c_e x_2^2 \tag{C.5}$$

where w is power and c_e is electrical damping

For the stochastic energy harvester, it is impossible to calculate exact power. Rather, expected value is used to investigate power output of energy harvester.

Using equation (C.3), expected value of harvested power can be calculated according to the following equation

$$\overline{w} = c_e E(x_2^2) = c_e \int_{-x_2 l}^{x_2 h} \int_{-x_1 l}^{x_1 h} {x_2}^2 P(x_1, x_2) dx_1 dx_2 \approx c_e \sum_i \sum_j {x_2}_i^2 P_{ij} dx_1 dx_2 \tag{C.6}$$

where $\overline{w}$ is expected value of harvester power, $x_1 h$ and $x_2 h$ is upper boundary of displacement and velocity respectively, $x_1 l$ and $x_2 l$ is lower boundary of displacement. In practical calculation, we assume that probability density function P is zero when random variable X is located outside of boundaries. Since probability density P is discretized in the proposed problem, the integrals in the equation (C.6) canbe approximated to the summation of discrete numbers.